

VICERRECTORÍA DE INVESTIGACIÓN Y POSTGRADO <u>DIRECCIÓN DE POSTGRADOS Y POSTÍTULOS</u>

FACULTAD DE CIENCIAS DEPARTAMENTO DE ASTRONOMÍA

Estudio espectroscópico del sistema múltiple en interacción HCG 31

Tesis presentada para optar al Grado Académico de Magíster en Astronomía.

AUTOR: DIEGO ALEJANDRO GÓMEZ ESPINOZA

LA SERENA, CHILE, MARZO 2022

CONSTANCIA

Don																																																									
Don	•	•	• •	•	 •	•	•	•	•	• •	•	•	•	•	•	•	•	•	•	•	•	•	•	•	•	•	 •	•	•	•	•	• •	•	•	•	•	•	•	•	• •	•	•	 •	•	 •	•	•	•	•	•	•	• •	•	•	•	•	•

HACE CONSTAR:

Que el trabajo correspondiente a la presente Tesis de Magíster, titulada "Estudio espectroscópico del sistema múltiple en interacción HCG 31", ha sido realizada por Don Diego Alejandro Gómez Espinoza, bajo mi dirección.

Para que conste y en cumplimiento de las normativas vigentes de la Universidad de la Serena, Chile, firmo el presente documento en La Serena, Chile, 29 de Marzo de 2022

TESIS PARA OPTAR AL GRADO DE MAGÍSTER EN ASTRONOMÍA

TÍTULO : ESTUDIO ESPECTROSCÓPICO DEL SISTEMA

MÚLTIPLE EN INTERACCIÓN HCG 31

PRESENTADA POR : LIC. DIEGO ALEJANDRO GÓMEZ ESPINOZA

DIRECTOR DE TESIS : DR. SERGIO PATRICIO TORRES FLORES¹

CO-DIRECTOR DE TESIS: DRA. VERÓNICA FIRPO²

TRIBUNAL CALIFICADOR

El tribunal de tesis, conformado por:

PRESIDENTE :

MIEMBROS DEL TRIBUNAL: * Dra. Duilia de Mello³

* Dra. Claudia Mendes de Oliveira⁴

* Dr. Marcelo Mora⁵

* Dr. Ricardo Amorín⁶

* Dr. Philippe Amram⁷

ACUERDAN OTORGARLE LA CALIFICACIÓN DE:

¹Universidad de La Serena.

²Gemini Observatory/NSFs NOIRLab, Casilla 603, La Serena, Chile

³Universidad Católica de América GSFC/NASA

⁴Universidad de Sao Paulo

⁵ANID/Universidad Católica de Chile

⁶Universidad de La Serena.

⁷Laboratorio Astrofísico de Marsella

La Serena, Chile, $\mathbf{29}$ de Marzo de $\mathbf{2022}$



AGRADECIMIENTOS

Escribir esta tesis fue muuucho más complicado de lo que pensaba y la verdad es que costó pero un montón, entre la pandemia, el estrés, el inglés, los códigos que no compilaban, y los gráficos que no decían nada, la verdad es que ha sido de los desafíos más grandes que he tenido, pero bueno este espacio es para agradecer y no un diario personal (pero es bacán poder escribir libremente por fin).

Muchas gracias Papá, la verdad es que sin ti nada de esto estaría pasando, tu apoyo ha sido fundamental para mí desde que tengo memoria y a pesar de que estemos lejos siempre te he sentido al lado mio. Nada mas que decir, estoy orgulloso de tener un papá como tú. Obviamente tengo que agradecer a mi mamá y a mi lela, gracias por todo el cariño, por toda la comprensión y por formarme, la verdad es que no hay palabras para agradecer todo lo que han hecho por mí, realmente las amo y gracias por todo nuevamente.

A mí polola, Alina, como no agradecerte, estuviste siempre conmigo en todo momento, el magíster en general fue bastante intenso y pucha, estar contigo siento que de verdad me ayudo a sobrellevar muchas cosas, te amo mucho, y bueno, ahora se viene el tuyo así que con todo y sabes que cuentas conmigo para lo que sea.

No puedo olvidar a mi hermana Sofía, que hayas estado en la casa durante la pandemia, en el momento donde comencé a acumular estrés de manera exponencial fue muy, muy importante para poder lidiar con el, riéndonos, viendo series, paseando a la Chimi, lo que sea, te amo, siempre puedes contar conmigo para cualquier cosa yo feliz estoy para ti, igualmente a la Pía, mi hermanita, muchas gracias por los buenos ratos, los bailes que me hacían reír, los juegos, por todo < 3.

A mi familia en general siempre le voy a estar agradecido, mis tíos, tías, primos, primas, primitos y primitas, todo buen rato que pasamos siempre me ayudo mucho más de lo que creen. Bueno, obviamente a todos mis compañeros del magíster, con los que convivimos el primer año en oficina, la pase genial, una lata que no se pudo repetir el segundo por el virus, pero hubiera sido mucho más llevadero todo el proceso. Finalmente, pero no menos importante quiero agradecer a mis directores, Sergio y Vero, fueron un 7, siempre me sentí apoyado y animado por ustedes, aprendí un sinfín de cosas, estoy trabajando con ustedes desde el 2018 y no me arrepiento para nada, un verdadero gusto tener mi primer acercamiento real a la ciencia con ustedes.

Este espacio final es para todas las personas que no mencioné pero sin duda me ayudaron en todo el proceso, mis amigos, familiares, muchas gracias por todo!

Bueno de aquí en adelante todo se pone muy técnico (y en inglés), pero la persona detrás de todo esto exprimió cada neurona de su cerebro para que todo el texto tenga algo de sentido.

Resumen

En este proyecto de tesis se presenta un profundo análisis del sistema múltiple en interacción HCG 31 utilizando datos de unidad integral de campo (IFU) del instrumento MUSE ubicado en el observatorio Very Large Telescope. Para obtener una comprensión completa del sistema derivamos: mapas de velocidad radial y de velocidad de dispersión, mapas del mecanismo de ionización del sistema, abundancias químicas y su distribución en toda la extensión del sistema, tasas de formación estelar y edades de las distintas regiones de formación estelar, distribución espacial de la población de estrellas Wolf-Rayet y también una reconstrucción de la historia de formación estelar de los miembros A, C, B y F. Medimos los flujos de las lineas de emisión y también realizamos una síntesis de la población estelar de los espectros obtenidos. Nuestros principales hallazgos son i) una cinemática claramente perturbada debido al evento de fusión que está experimentando el sistema, ii) una ionización casi exclusivamente debida a estrellas masivas jóvenes exceptuando el núcleo de la galaxia HCG 31 A, donde hay una pequeña contribución de choques, iii) abundancia de oxígeno baja y distribuida de manera prácticamente homogénea en todo el sistema, iv) una clara población de estrellas Wolf-Rayet de carbono distribuidas en la zona central del grupo y v) confirmamos el origen de marea de los objetos E, F y H basándonos en su ubicación en la relación masa-metalicidad, pues estos objetos muestran una metalicidad mayor a la que corresponde según su masa estelar según dicha relación. Todos estos hallazgos son clara evidencia de que HCG 31 es un grupo compacto con una fusión de galaxias en su centro en fase temprana.

Summary

On this thesis we present an in-depth analysis of the multiple interacting system HCG 31. We use integral field unit (IFU) data taken from the MUSE instrument located at the Paranal observatory. In order to obtain a complete understanding of the system we derive: radial velocity and dispersion velocity maps; maps of the ionization mechanism of the system, chemical abundances and their distribution over the whole system, star formation rates and ages of the different star-forming regions, spatial distribution of the Wolf-Rayet stellar population and we perform a reconstruction of the formation history of galaxies HCG 31 A, C, B and F. We measure the emission-line fluxes and also made a stellar population synthesis. Our main findings are i) a clearly disturbed kinematics due to the merger event that the system is experiencing, ii) the ionization is produced exclusively via star-formation except for the nucleus of the galaxy HCG 31 A, where there is a small contribution of shocks, iii) a low oxygen abundance which is distributed in a homogeneous way through the system, iv) a prominent population of carbon Wolf-Rayet stars in the central zone of the group and v) we confirm the tidal origin of objects E, F and H based on their location in the mass-metallicity relation because these objects show a fairly high metallicity for their stellar mass. All these findings are clear evidence that HCG 31 is a compact group in an early merger phase.

Contents

1	Intr	oduction	1
	1.1	Galaxy interactions	1
	1.2	Galaxy interactions in the local Universe	2
	1.3	The Hickson compact group 31	4
2	Mot	civation, goal and objectives	11
3	Dat	a	12
	3.1	Type of data used: integral field spectroscopic observations	12
	3.2	Observations and data reduction	14
4	Ana	llysis	18
	4.1	Description of the code FADO	18
	4.2	Description of the code IFSCUBE	20
	4.3	Emission-line measurement	20
	4.4	Stellar population synthesis	25
	4.5	Kinematics	26
		4.5.1 Radial velocity	26
		4.5.2 Velocity dispersion	26
	4.6	Interstellar extinction correction	27
		4.6.1 Fitzpatrick law	28
		4.6.2 Calzetti law	29
	4.7	Star Formation Rate determination	31
	1.8	Physical proporties	39

CONTENTS

		4.8.1	Electron temperatures	33
		4.8.2	Electron density	34
	4.9	Chemic	cal abundances	36
		4.9.1	Oxygen abundances	36
		4.9.2	Sulfur abundances	37
		4.9.3	Nitrogen abundance	38
		4.9.4	Helium abundance	38
		4.9.5	Argon abundance	39
		4.9.6	Empirical calibrations: N2 and O3N2	40
	4.10	$H\alpha$ equ	nivalent width and age determination	42
	4.11	Ionizat	ion mechanism: BPT diagnostic diagrams	43
5	Resi	ulta		45
J				
	5.1	Kinema	atics	45
		5.1.1	Radial Velocity: The complex velocity field of HCG 31	45
		5.1.2	Velocity dispersion	49
	5.2	Extinct	sion: A 2D view of the dust distribution in HCG 31	51
	5.3	Physica	al parameters	54
		5.3.1	Electron Temperatures	54
		5.3.2	Electron Density	55
	5.4	Chemic	eal Abundances in HCG 31	57
		5.4.1	Empirical relations and Direct Method	57
		5.4.2	Empirical calibrators results and HII-CHI-Mistry	62
		5.4.3	Metallicity gradients on HCG 31	65
	5.5	$H\alpha$ lun	ninosities and star formation rates: Witnessing the stellar birth in a	
		mergin	g system	71
	5.6	Estima	ting the ages of the different star forming burst	77
		5.6.1	$H\alpha$ Equivalent width and ages	77
		562	Ages estimates through stellar populations: FADO	82

	5.7	Wolf-Rayet bump	1
	5.8	Ionization Mechanism	7
	5.9	The Mass-Metallicity relation of HCG 31)
6	Disc	cussion 94	1
	6.1	Are we discovering more super star clusters in HCG 31?	4
	6.2	A peculiar knot in HCG 31 A	7
	6.3	About the TDG nature of member F	9
	6.4	Abundance gradients)
	6.5	The star-formation history of HCG 31	2
	6.6	Disentangling the Hickson Compact Group HCG 31	4
		6.6.1 The northern tidal tail: Objects A1, A2 and A3	4
		6.6.2 The central merger: The A+C complex	3
		6.6.3 A close companion: Galaxy B	3
		6.6.4 The southern tidal tail: Objects E, H and F	9
7	Sun	nmary and Conclusions 111	L
8	Fut	ure Work 113	3

List of Figures

1.1	The antennae galaxies. An example of a major merger between two spiral	
	galaxies. Credits ESA/Hubble	2
1.2	A plot showing the flattening of the metallicity gradients in interacting galaxies.	
	The black dots represent the metallicity gradient of interacting galaxies and	
	the white dots represent the gradients of isolated galaxies. M_k Represents the	
	absolute magnitude in the K band. L_{IR} represent the total luminosity in the	
	infrared. Image taken from Rupke et al. (2010a)	3
1.3	Color composite image of HCG 31. The colors are: purple (NUV with GALEX), $$	
	blue (B435 with HST), yellow-green (V606 with HST), orange (8 μm with	
	Spitzer), and red (I814 with HST). Group galaxies and tidal debris are labeled	
	in white. The scale presented in the image represent 30 arcseconds. Which is	
	equivalent to ~ 8 kpc. North is up and East is left. Image taken by Gallagher	
	et al. (2010)	5
1.4	Radial velocity map of the central part of the system obtained by Richer et al.	
	(2003). The scale colors represent the radial velocity for every spaxel. Members	
	A, C, E and F are labeled. Using this map, the authors conclude that the A+C	
	complex consists in only one galaxy interacting, because they did not find any	
	remarkable discontinuity in the velocity between the central galaxies. The scale	
	presented in the image of 20" epresents ~ 5 kpc. North is up and East is left .	7
1.5	Wolf-Rayet bump detected by López-Sánchez et al. (2004) in the spectra of the	
	central region of HCG 31. This bump is produced by the emission of the line	
	$\mathrm{He}_{II}\lambda 4686$	7

1.6	The Hickson compact group 31 observed in the ${\bf r}'$ band using the Gemini GMOS	
	instrument. Every member of the group are labeled. The scale is represented	
	with the bar indicating 1 arcmin which correspond to \sim 16 kpc. Image taken	
	from Mendes de Oliveira et al. (2006) North is up and East is left $\ \ .$	8
1.7	Luminosity-Metallicity relation obtained by Mendes de Oliveira et al. (2006)	
	using the luminosity in the K_s band (M_{K_s}) . The black line represents the best	
	fit to the LZR obtained by Lee et al. (2003) and the black triangles represent	
	their sample. The galaxies C, G and B follows the relation but the galaxies A1,	
	H, and R shows a high metallicity for their luminosity. This could be evidence	
	of their tidal origin. Plot taken from Mendes de Oliveira et al. (2006)	8
1.8	Radial velocity map obtained by Amram et al. (2007). The velocity scale shows	
	a range from 3950 km s^{-1} to 4180 km s^{-1} . The white contours represent	
	the isovelocities taken from the velocity map in HI (Verdes-Montenegro et al.	
	(2005)). The scale of 20 arcseconds represents \sim 5kpc. Figure taken from	
	Amram et al. (2007)	10
3.1	Schematic representation of a datacube showing the three principal axis (X,Y,λ) .	
	Figure taken from Roth et al. (2002)	13
3.2	A representation of the three different types of instruments that creates dat-	
	acubes. Lenslets, Lenslets + fibers and Slicer. Image taken from Allington-	
	Smith et al. (1998)	14
3.3	GMOS-N r' band image of the entire system, the black squares show the lo-	
	cation of the four IFUs taken by MUSE, the r^\prime band image was taken from	
	Mendes de Oliveira et al. (2006)	15
3.4	RGB image of HCG 31 made collapsing images of different lines. Red represents	
	${\rm H}\alpha$ (6647 \mathring{A} - 6654 \mathring{A}), Green represents [NII] λ 6584 \mathring{A} (6667 \mathring{A} - 6674 \mathring{A}) and	
	Blue represents [OIII] λ 5007Å (5070 Å - 5078 Å). The wavelength ranges are	
	not corrected by redshift	16

3.5	${\rm H}\alpha$ colapsed image over the entire cube. The wavelength range considered for	
	the image is 6647 \mathring{A} - 6654 \mathring{A} - 6654 \mathring{A}	17
4.1	Schematic view of FADO Showing the function of their three main stages.	
	Figure extracted from Gomes & Papaderos (2017)	20
4.2	Continuum-substracted emission lines of a spaxel in the central zone of HCG 31, $$	
	the red dotted line represent the fit performed by FADO. The blue line repre-	
	sents the emission lines of the spectra. The X axis represents wavelength and	
	the Y axis the relative flux	22
4.3	Emission-line flux maps of HCG31 obtained with FADO, the lines are ${\rm H}\beta,$	
	[OIII] λ 5007 Å, [OI] λ 6300 Å, H α , [NII] λ 6584 Å, and [SII] λ 6717 Å. The maps	
	are in pixel coordinates and the scale color represents the flux. All colorbars	
	are normalized to the maximum flux in $H\alpha$	23
4.4	Emission-line ratio maps of [NII] λ 6584 Å/H α , [OIII] λ 5007 Å/H β , [SII] $\lambda\lambda$ 6717,6	$731\mathrm{\AA/H}lpha$
	and [OI] $\lambda6300\text{Å}/\text{H}\alpha,$ the contours in all the maps are of H α emission. The	
	maps are in pixel coordinates	24
4.5	Extinction curve for the Milky Way derived by Fitzpatrick (1999) (solid line),	
	also there is the curve derived by Cardelli et al. (1989) (dotted line) and Seaton	
	(1979) (segmented line). The three curves assume $R_V=3.1$. Figure taken	
	from Fitzpatrick (1999)	29
4.6	Schematic view of the five models describing the dust distribution. Figure	
	taken from Calzetti et al. (1994)	30
4.7	Variation of the intensity ratios in function of the density of free electrons for	
	two different doublets: [OII] $\lambda\lambda$ 3729, 3726 Å and [SII] $\lambda\lambda$ 6717, 6731 Å. For	
	this plot it is assumed an electron temperature of $T_e=10.000$ K. Figure taken	
	from Osterbrock (1989)	35

4.8	Metallicity versus N2 parameter for a sample of HII regions, solid line repre-	
	sents the relation derived by Pettini & Pagel (2004), grey segmented line the	
	fit by Pérez-Montero & Contini (2009), grey dotted line the fit by Nagao et al.	
	(2006) and green solid line represent the fit by Marino et al. (2013), figure	
	taken from Marino et al. (2013) $$	41
4.9	$I([O_{III}]5007\mathring{A})/I(H\beta)$ vs $I([N_{II}]6584\mathring{A})/I(H\alpha)$ BPT diagram, the black dots	
	are galaxies taken from the SDSS at $0.02 < z < 0.3$, the dotted line represent	
	the limit derived by Kewley et al. (2001) and the segmented line represent the	
	limit derived by Kauffmann et al. (2003), figure taken from Kauffmann et al.	
	$(2003) \dots \dots$	44
5.1	${ m H}lpha$ Radial velocity derived by IFSCUBE. The black contours represent ${ m H}lpha$	
	emission. The gray ellipses show the three main kinematic entities visually	
	identified (see text). The black lines represent the different simulated slits	
	used to analyse the internal kinematic of each object. The radial velocity span	
	range of $3950 km/s < v < 4200 km/s$ North is up and East on left	46
5.2	Velocity gradients derived for the different pseudo slits represented in Fig-	
	ure 5.1. The errorbars represents the uncertainty obtained from the fitting	
	parameters of IFSCUBE as explained in section 4.5.1. The gradients run	
	from East to West	48
5.3	${\rm H}\alpha$ velocity dispersion map. The zones with higher σ are in the center of the	
	merger between A and C. Members B, E and F present low velocity dispersion	
	(< 30 $km\ s^{-1}).$ The group span a range of velocity dispersion of $10km/s <$	
	$\sigma < 95 km~s^{-1}.$ However, our values probably are overestimated (see text).	51
5.4	E(B-V) map of HCG 31. White contours represents H α in emission. The group	
	shows low values of $E(B-V)$ excepting in the central zone. Where the $E(B-V)$	
	shows a neak in a knot of galaxy HCG 31 A	54

5.5	Map of $T_e([SIII])$ of HCG 31, the contours represent $H\alpha$ emission, the red	
	boxes marks the positions of the 2 main ${\rm H}\alpha$ knots in the central zone of this	
	system. The central zone of the system shows the lower values of temperature	
	with $T_e([SIII]) \sim 0.7[10^4 K]$. While the knots located at members F and B	
	shows higher values of temperature	56
5.6	Map of electron density derived with the $[S_{II}]$ 6717,6731 \mathring{A} lines. The contours	
	are $H\alpha$ in emission. Almost the whole group shows low densities with $n_e <$	
	$100[cm^{-3}]$. In central knots of the A+C it is seen a peak in the density with a	
	knot showing $n_e \sim 250[cm^{-3}]$	57
5.7	Oxygen abundance map obtained using empirical calibrators for $T_e([OIII])$.	
	The overplotted contours correspond to $H\alpha$ emission. A knot located in the	
	southern part of the central zone shows the peak of oxygen abundance in the	
	whole system with $12 + log(O/H) \sim 8.6$ dex	58
5.8	Map of the argon abundance obtained with the equations described in 4.9 .	59
5.9	Helium abundance obtained with the method described in section 4.9	59
5.10	Nitrogen abundance obtained with the method described in section 4.9	60
5.11	Sulfur abundance obtained with the method described in section 4.9 $$	61
5.12	Oxygen abundance maps calculated with different strong lines calibrations and	
	HII-CHI-Mistry; (a) N2 (Marino et al. 2013), (b) O3N2 (Marino et al. 2013)	
	and (c) HII-CHI-Mistry (Pérez-Montero et al 2014) in all the maps the contours	
	represent $H\alpha$ emission	66
5.13	Oxygen abundance maps calculated using strong lines empirical calibrators;	
	(a) S3O3, (b) S23 and (c) AR3O3	67
5.14	Comparison of the metalicities obtained with the different strong-line empirical	
	calibrators, ERM, HII-CHI-Mistry and the values obtained by López-Sánchez	
	et al. (2004) (L04). Every panel represent a different knot in HCG 31. The hor-	
	izontal segmented lines represents the oxygen abundance obtained with ERM.	
		68

5.15	Metallicity gradients and their fit parameters derived for different structures	
	in HCG 31; (a) Galaxy B. (B) southern tidal tail and (c) the central zone.	
	For comparation we include the gradients of other similar objects in panels	
	(a) and (b). The linear regression were perfored using the package CURVEFIT	
	from SCIPY which allow us to consider the uncertainties to perform the linear	
	regression.	69
5.16	Map of star formation rate for HCG 31 derived using the calibration of Kenni-	
	cutt & Evans (2012)	72
5.17	Extinction corrected H α map of HCG 31, the contours represent the edges of	
	the segmentations obtained by SExtractor, each knot are labeled with their	
	respective ID	74
5.18	Map of $H\alpha$ equivalent width derived by FADO, black contours represent $H\alpha$	
	in emission	79
5.19	Map of ages obtained interpolating with the models of Starburst99 assuming	
	an instantaneous star formation event, a Salpeter IMF was assumed with mass	
	limits 1-100 M_{\odot} and with different metallicites; (a) with Z = 0.004 and (b)	
	with $Z = 0.008$	80
5.20	Ages derived through the population synthesis performed by FADO, black	
	contours represent $\mathrm{H}\alpha$ in emission and white contours represent continuum	
	emission (a) Luminosity-weighted Age and (b) Mass-weighted age	83
5.21	(a) An example of the spectra of a spaxel with the red bump visible, it is also	
	shown the continuum fit performed for all the spaxels in order to map the red	
	bump, (b) Intensity map of the red bump obtained for the central region of	
	HCG 31, black contours represent H α in emission and (c) Integrated spectra of	
	all the spaxels in (b) with the gaussian fit performed to estimate the number	
	of WC stars in the central region of HCG 31	86

5.22	BPT diagrams for the whole system. The contours represent $H\alpha$ in emis-	
	sion. Mostly of the points lies in the SF sequence. Almost all points in the	
	AGN/LINER zones lies in the outskirts of the galaxy. Probably due to the low	
	${\rm S/N}$ on these regions, or to an eventual contribution of shocks/DIG. $$	88
5.23	BPT diagram of the inner zone of the A+C complex. We see a composite	
	ionization in the HCG31 A knot, this is probably a contribution of shocks on	
	this region, also this region presents a peak in the electron density ($\sim 200~cm^{-3}$)	89
5.24	Segmentations used over a smoothed R-band synthetic image. for galaxy B	
	we integrate the spectra of segmentations B1, B2 and B3. For Galaxy E we	
	integrate segmentations E1 and E2. The color scale is to show the differences	
	between each segmentation. The black contours represent the smoothed ${\rm H}\alpha$	
	emission	92
5.25	MZR relation derived for HCG 31 (green points in three panels). To compare,	
	we present the MZR of nearby dwarf galaxies derived by Lee et al. (2006) as	
	black points in the three panels. The masses considered were calculated by	
	FADO. In (a) is shown the MZR obtained using the ERM Method. In (b) and	
	average between N2 and O3N2 and (c) with HII-CHI-Mistry	93
6.1	Continuum emission map of HCG 31. The black contours represent the ${\rm H}\alpha$	
	emission, the red circles show the locations of the principal offsets between	
	continuum and emission peaks	97
6.2	Zoom into the integrated spectra of a 1"x1" box centered at the knot A, it is	
	seen that the spectrum shows WR features, a weak red bump and an intense	
	blue bump.	98
	▲	_

6.3 Luminosity fraction at the normalization wavelength (5100 Å) as a function of the age for the galaxies HCG 31 A+C, HCG31 A, HCG 31 B and HCG 31 F1. The colors light-blue, blue, light-green and orange stand for metallicities of 0.02 Z_{\odot} , 0.2 $_{\odot}$, 0.4 $_{\odot}$ and 1 Z_{\odot} respectively. The shaded area shows an Akima-smoothed (Akima 1970) version of the SSP contributions, giving as a result an illustration of the star formation history of the different galaxies. . 103

List of Tables

3.1	Observation log for the four IFU fields observed with MUSE	15
5.1	Average E(B-V) values obtained for each member of HCG 31 $ \dots \dots \dots$	53
5.2	Physical parameters of the different knots in HCG 31. Col (1) Shows their IDs.	
	Col (2) show the [SIII]temperature which is the only measured using the direct	
	method. Cols (3), (4) and (5) shows the temperatures of [SII], [SII], [OIII] and	
	[OII] respectively. Col (5) shows the electron density obtained with the Sulfur	
	doublet [SII] $\lambda\lambda$ 6717 6731	55
5.3	Chemical abundances of the different knots in HCG 31. All the Chemical abu-	
	dances have been measured using the equations explained in section $4.9.$	63
5.4	Results of the linear regression for the different gradients of HCG 31 $$	71
5.5	Star formation rates and ${\rm H}\alpha$ luminosities for the knots identified using SEx-	
	tractor. Col (1) shows the ID, Col (2) the H α luminosity. Col (3) shows the	
	SFRs obtained with the calibration of Kennicutt & Evans (2012) and Col (4)	
	the SFR obtained with the calibration of Kennicutt (1998a)	76

5.6	Ages and EW obtained with different methods of the knots of $HCG31;$ Col	
	(1) shows the ID of every knot. Col(2) shows the EW derived by FADO. Col	
	(3) shows the age obtained interpolating with the models of S99, assuming	
	a metallicity of $z=0.008$. Col (4) Shows the age obtained with S99 but	
	assuming a metallicity of $z=0.004$. Col (5) Shows the mass-weighted age of	
	the population vector fitted by FADO and Col (6) shows the light-weighted	
	age obtained by FADO. We note that uncertainties for columns (5) and (6)	
	are lower than 10 Myrs, as discussed in the text. Cols (3) and (4) represents	
	the age of the last episode of star formation. On the other hand, cols (5) and	
	(6) shows the weighted age of the stellar popularion fitted by FADO	78
5.7	Different masses and metallicities determinations for the members of HCG 31; Col	
	(1) ID of the object. Col (2) Mass determination performed by FADO. Col-	
	umn (3) mass determined by López-Sánchez & Esteban (2010). (4) Adopted	
	mass obtained from the K-band luminosities taken from Mendes de Oliveira	
	et al. (2006). Column (5) Oxygen abundance obtained through an average be-	
	tween methods N2 and O3N2. Column (6) Oxygen abundance obtained using	
	HII-CHI-Mistry and Column (7) Oxygen abundance obtained using the ERM	
	method	91

Chapter 1

Introduction

1.1 Galaxy interactions

The processes of formation and transformation of galaxies are crucial to understand their evolution. The hierarchical model is the process in which the largest structures in the universe are formed through the fusion of smaller structures. According to the hierarchical model of galaxy formation, the interactions between dwarf galaxies at high redshift were the foundations for the formation of current galaxies (Toomre & Toomre 1972). A good way to investigate the physical processes that take place in galaxy interactions is by studying them in the local universe. This strategy could give clues about the formation and evolution of galaxies. A great advantage of study galaxy mergers and interactions in the local universe is the better spatial resolution that we have due to the proximity of these objects. Although different studies have been done to compare properties of galaxies in the local and distant universe (e.g Epinat et al. 2010), it should be noted that there is clear differences between studying galaxy mergers at the local universe and studying at high redshift, e.g the mass of the gas has evolved with redshift and also the star formation rates (SFR). Thus, the comparison of physical processes and phenomena is more relevant than the comparison of the absolute values. Indeed, galaxy mergers are unique laboratories to understand the transformation of galaxies due to gravitational effects. However, to fully understand these phenomena is mandatory combine the observational results with simulations and models.

There are many types of mergers between galaxies. Depending on the type of collision the galaxies will be affected in different ways. If one galaxy is much



Figure 1.1: The antennae galaxies. An example of a major merger between two spiral galaxies. Credits ESA/Hubble

less massive than the other (< 1:4 of the mass according to Kaviraj (2014)) the merger is called *minor merger*. This type of merger does not affect observationally the most massive galaxy. If the two galaxies have similar mass (or at least one have > 1:3 of the mass of the other according to Kaviraj et al. 2013) occurs a *major merger* on which both galaxies are severally affected in their morphology. There are some features that indicates that a major merger is ocurring. e.g. tidal tails, destruction of the disks, formation of tidal dwarf galaxies (TDG), among others. In Figure 1.1 there is an optical image, taken with the Hubble Space Telescope, of a major merger between two spiral galaxies, in this case the Antennae Galaxies.

1.2 Galaxy interactions in the local Universe

During the last years, several authors have studied the properties of interacting galaxies. From the point of view of its physical properties (e.g. Zaragoza-Cardiel et al. 2018), as well as from the point of view of its kinematic properties (e.g. Plana et al. 2003, Amram et al. 2007, Torres-Flores et al. 2010). These efforts allowed us to understand the role of galaxy interactions in their evolution. However, several questions still remain open, with no clear answers. For example, as a result of the interaction between galaxies it is expected an increase in their SFR. Various authors propose different scenarios to explain this increase. Xu et al. (2010) studied a sample of pairs of spiral-elliptical galaxies. They find that most spiral galaxies do not present an increase in their SFRs. On the other hand Patton et al. (2011) study a sample of galaxy pairs. They find increased SFRs, which is

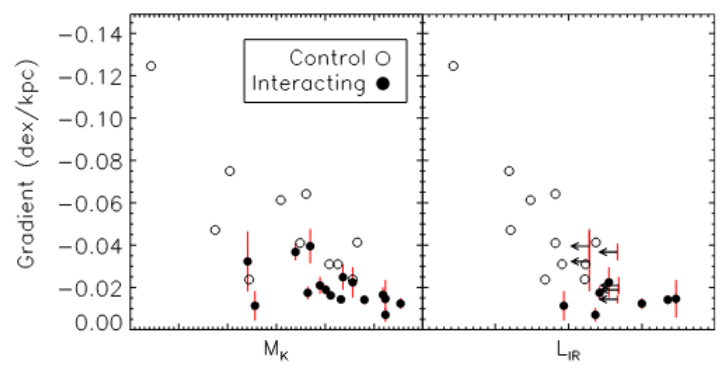


Figure 1.2: A plot showing the flattening of the metallicity gradients in interacting galaxies. The black dots represent the metallicity gradient of interacting galaxies and the white dots represent the gradients of isolated galaxies. M_k Represents the absolute magnitude in the K band. L_{IR} represent the total luminosity in the infrared. Image taken from Rupke et al. (2010a)

expected due to the interaction processes between galaxies. Additionally, Ellison et al. (2011) found that galaxies associated in pairs have a higher fraction of active galactic nuclei (AGN) compared with isolated galaxies. Rupke et al. (2010a) find that interacting galaxies exhibit metallicity gradients more flattened than those observed in isolated galaxies, phenomena that could be produced by the process of interaction between galaxies. In Figure 1.2 can be seen the flattening in the metallicity gradient of interacting galaxies with respect to isolated galaxies.

There are other processes in galaxy interactions that end up with the formation of new galaxies. Duc & Mirabel (1998) studied the interacting system NGC 5291, where they found star-forming objects in the intergalactic medium. The authors suggest the existence of newly formed dwarf galaxies in NGC 5291, tidal dwarf galaxies. These objects should be free of dark matter and should have high metallicities for their masses. There are more interesting works on TDGs in the literature (e.g. Weilbacher et al. (2003),de Mello et al. (2012)) Its fate is still an open question until nowadays.

As shown before, interacting and merging systems are ideal laboratories to understand different physical and kinematical process that take place in our universe. On this thesis we will develop a deep spectroscopic study of the Hickson Compact Group 31.

1.3 The Hickson compact group 31

On this section we will review the most important investigations about our object of study. The Hickson compact group 31.

Our object of study on this thesis project consists on a very particular group of galaxies, the Hickson compact group 31 (HCG 31). This group lies at a distance of 59.38 ± 4.16 Mpc. That distance was measured assuming a redshit of $z = 0.01347 \pm 0.00002$ (Wong et al. 2006) and a value of the Hubble constant of $H_0 = 67.8 km \ sec^{-1} \ Mpc^{-1}$ (Riess et al. 2016).

This group consists on many low-mass galaxies with low-metallicites and all of them interacting (Rubin et al. 1990). This particular configuration makes HCG 31 an ideal laboratory to study galaxy interactions and evolution.

Due to its configuration, HCG 31 is a very studied object and many authors have contributed to the knowledge of this system, (e.g Rubin et al. 1990, Iglesias-Paramo & Vilchez 1997, López-Sánchez et al. 2004, Amram et al. 2007, Alfaro-Cuello et al. 2015, Torres-Flores et al. 2015, among others). Hickson (1982) was the first study on which the system has been classified as a compact group of galaxies. On this study the author detected 4 members on this group, HCG 31 A, B, C and D. Rubin et al. (1990) detected four new members, HCG 31 E, F, G and Q. Also conclude that member D was not part of the group due to its higher redshift. More recently Mendes de Oliveira et al. (2006) detected another member of the system, HCG 31 R. Currently, our vision of HCG 31 consists on 9 galaxies: A, B, C, E, F, G, H, Q and R. In Figure 1.3 We show a color composite image of HCG 31, taken from Gallagher et al. (2010), on which we can see 7 galaxies labeled, members Q and R lies at the north of the field of view.

The entire group is embedded in a common envelope of HI (Williams et al. 1991). The HI mass of the system was estimated by Williams et al. (1991), which find a total HI mass of $2.1 \times 10^{10} M_{\odot}$. These authors also found that the HI peaks at the overlap between HCG A and HCG C.

Rubin et al. (1990) detected high $H\alpha$ emission in the central part of the system and in the member F. This starburst in the central region is most likely triggered by the merger between the galaxies A and C.

Using H α Fabry-Perot data, Richer et al. (2003) derived radial velocity maps and velocity dispersion maps for the central region of the system. They found that there are no discontinuities on the velocity map between the galaxies A



Figure 1.3: Color composite image of HCG 31. The colors are: purple (NUV with GALEX), blue (B435 with HST), yellow-green (V606 with HST), orange (8 μm with Spitzer), and red (I814 with HST). Group galaxies and tidal debris are labeled in white. The scale presented in the image represent 30 arcseconds. Which is equivalent to ~ 8 kpc. North is up and East is left. Image taken by Gallagher et al. (2010)

and C. Thus, they conclude that it consists in only one interacting galaxy. In Figure 1.4 is presented their radial velocity map for the central part of the system. These authors proposed that the starburst in the A+C complex is triggered by an interaction with the member HCG 31 G.

Richer et al. (2003) Also present the luminosity-metallicity relation for the objects A, C, B and F. They find that the galaxies A and C do not follow the main trend, with high luminosities and low metallicities. The explanation given by the authors involves gas inflows triggered by the interaction with galaxy G. Those inflows are currently diluting the central metallicities of the galaxies. Also the high luminosities could be been triggered by the interaction.

A very complete study of the system was developed by López-Sánchez et al. (2004). They perform a deep analysis of the physical properties and SFR using optical and Near-Infrared (NIR) imaging, also the authors used optical long-slit

middle-resolution spectroscopy. Using their data, the authors calculate electron temperatures and densities, chemical abundances, ages, luminosity and SFR.

An interesting result obtained by López-Sánchez et al. (2004) is that they detected a Wolf-Rayet bump in the spectra of the galaxy HCG 31 C (see Figure 1.5), which indicate the presence of massive stars. This bump can be identified with the blend of the spectral lines $\text{He}_{II}\lambda$ 4686, $\text{C}_{III}/\text{C}_{IV}\lambda$ 4650 and $\text{N}_{III}\lambda\lambda/4634,4640$. Moreover, the most important emission in the bump arises from the Helium lines. The presence of such type of stars is a strong evidence of the starburst on this system.

Using the spectroscopic data, López-Sánchez et al. (2004) determine position-velocity diagrams. They find a sinusoidal pattern on the slit that passes through members A and C. This pattern is a evidence of a merging process, which contradicts the result obtained by Richer et al. (2003).

The authors also derive the ages for the different starbursts in the system. They find that all the bursts have a very similar age on the order of ~ 5 Myr, which is consistent with the presence of Wolf-Rayet stars Schaerer & Vacca (1998). The values of the oxygen abundances were derived using the direct method. They find that all the members of the group present low oxygen abundances, spanning a range of $12 + log(O/H) \sim 8.03-8.37$.

Mendes de Oliveira et al. (2006) detected the new member, namely HCG 31R, and suggests that it correspond to a TDG candidate. Figure 1.6 presents an image of the group obtained with the Gemini GMOS instrument using the r' band filter. In the image it is possible to observe all the members of the group. Mendes de Oliveira et al. (2006) derive the luminosity-metallicity relation (LZR) for HCG 31 using K_s-band magnitudes, which mainly trace stellar emission (at this redshift). The LZR obtained by the authors is presented in Figure 1.7. As a control sample they use the LZR for dwarf galaxies obtained by Lee et al. (2003). In the Figure can be seen that the galaxies C, G and B follow the relation but show higher magnitudes. Members A1, H, R, E2, F1 and F2 shows higher metallicities for their luminosities. Members A1, H and R do not follow the relation. Then, these authors suggest that the members H, A1, R, F1, F2 and E2 could be tidal debris or TDG candidates.

Amram et al. (2007) present a kinematic study of the group using high-resolution Fabry-Perot data, with a resolution of R=45900 (centered in H α). They present maps of radial velocity and velocity dispersion for almost the whole group.

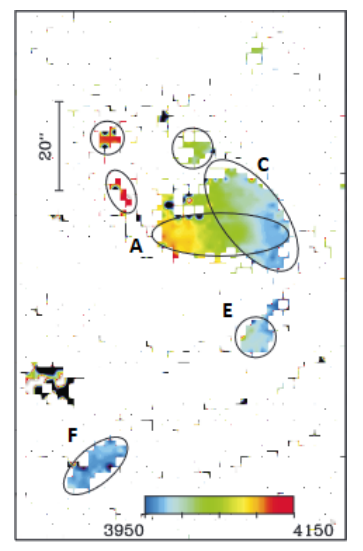


Figure 1.4: Radial velocity map of the central part of the system obtained by Richer et al. (2003). The scale colors represent the radial velocity for every spaxel. Members A, C, E and F are labeled. Using this map, the authors conclude that the A+C complex consists in only one galaxy interacting, because they did not find any remarkable discontinuity in the velocity between the central galaxies. The scale presented in the image of 20"epresents $\sim 5~\rm kpc$. North is up and East is left

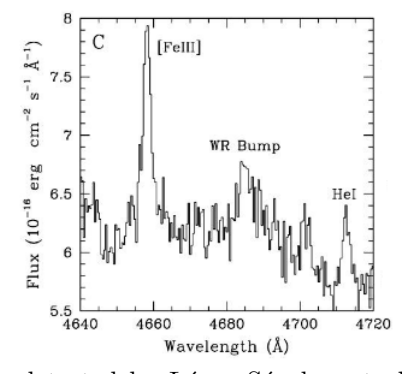


Figure 1.5: Wolf-Rayet bump detected by López-Sánchez et al. (2004) in the spectra of the central region of HCG 31. This bump is produced by the emission of the line $\text{He}_{II}\lambda 4686$

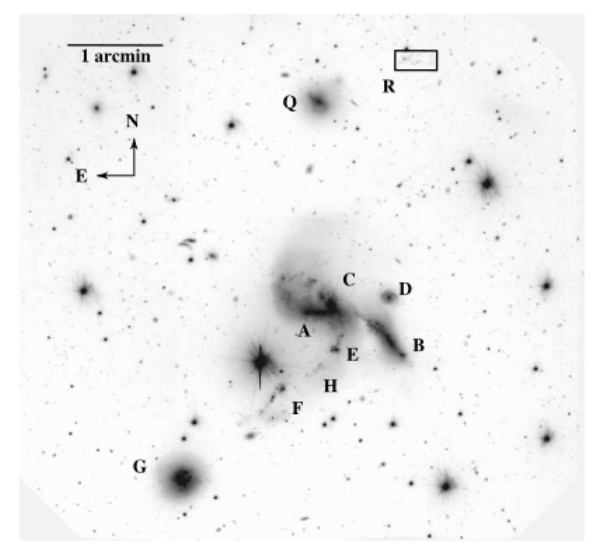


Figure 1.6: The Hickson compact group 31 observed in the r' band using the Gemini GMOS instrument. Every member of the group are labeled. The scale is represented with the bar indicating 1 arcmin which correspond to ~ 16 kpc. Image taken from Mendes de Oliveira et al. (2006) North is up and East is left

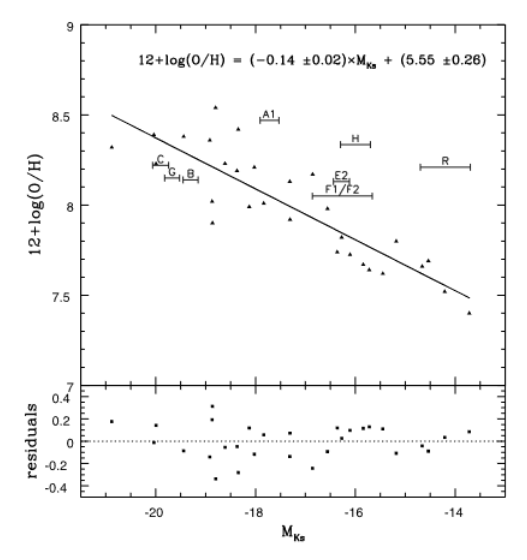


Figure 1.7: Luminosity-Metallicity relation obtained by Mendes de Oliveira et al. (2006) using the luminosity in the K_s band (M_{K_s}) . The black line represents the best fit to the LZR obtained by Lee et al. (2003) and the black triangles represent their sample. The galaxies C, G and B follows the relation but the galaxies A1, H, and R shows a high metallicity for their luminosity. This could be evidence of their tidal origin. Plot taken from Mendes de Oliveira et al. (2006)

Figure 1.8 presents their radial velocity map. In that map is possible to see a rotating pattern in the central zone of the group with no large variations between galaxies A and C. A striking result obtained by Amram et al. (2007) is the double component detected in the $H\alpha$ profile near to the galaxy A and also in the galaxy C. This is an evidence of disks overlapping which is a clear insight of an ongoing merger. According to the classification given by Surace (1998) HCG 31 belongs to the pre-merger class (Amram et al. 2007) because it shows "two nuclei with well-developed tidal tails and bridges". The features suggesting an ongoing merger in HCG 31 are:

- Overlapping components through the system.
- Wider velocity profiles in the interface between galaxies HCG 31 A and HCG 31 C.
- The kinematic peculiarities.
- Presence of tidal tails, suggesting a bound orbit between the galaxies.
- Very small separation between the central galaxies.

These pieces of evidence contradict the scenario suggested by Richer et al. (2003).

A very interesting study of this system was developed by Gallagher et al. (2010) using HST imaging to study star clusters (SCs) population in HCG 31. They determined the age of the population of SCs to be < 10 Myr SCs. They find ~ 400 SCs candidates and ~ 40 globular cluster candidates through the entire system. The authors also calculate the SFR of the entire system and obtained $\sim 10 \ M_{\odot}yr^{-1}$. They did not find any evidence of an underlying old stellar population in galaxy F suggesting that this is a completely new structure.

A deep study of the central region of HCG 31 was done by Alfaro-Cuello et al. (2015). The authors use IFU observations taken with Gemini/GMOS, centered in the overlap region between galaxies A and C. They find more evidence supporting the merger scenario proposed by Amram et al. (2007): i) high SFR density in the central region which is difficult to maintain with only a single dwarf galaxy and ii) using the same data Torres-Flores et al. (2015) detected a smooth gradient in the oxygen abundance map linking the galaxies A and C. This gradient suggests gas mixing in the interface between galaxies A and C (Torres-Flores et al.

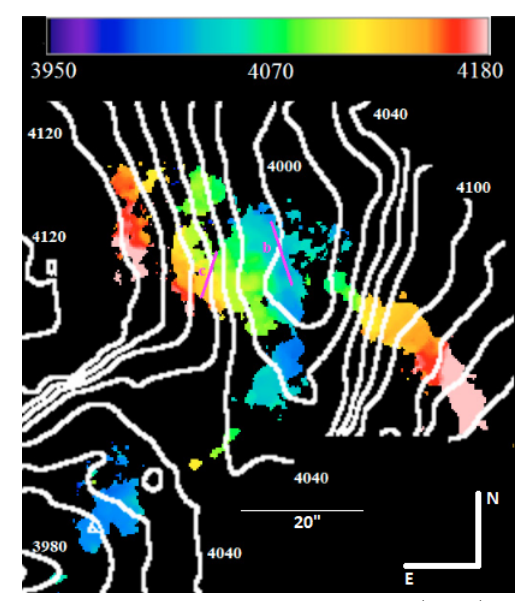


Figure 1.8: Radial velocity map obtained by Amram et al. (2007). The velocity scale shows a range from 3950 km s^{-1} to 4180 km s^{-1} . The white contours represent the isovelocities taken from the velocity map in HI (Verdes-Montenegro et al. (2005)). The scale of 20 arcseconds represents \sim 5kpc. Figure taken from Amram et al. (2007).

2015). Alfaro-Cuello et al. (2015) also detected a super star cluster (SSC) near to the nucleus of the galaxy HCG 31C. This SSC is currently triggering more star formation at their surroundings with its stellar winds (Alfaro-Cuello et al. 2015).

As shown above, HCG 31 offers a natural place to seek for answers to different open questions in the field of interacting/merging galaxies.

Chapter 2

Motivation, goal and objectives

In the previous chapter we reviewed the previous results found in the literature about our object of study HCG 31. However, there are several open questions about this system: How do the chemical abundances behave in HCG 31? Is this behaviour correlated with the kinematics of the system? Are shocks an important ionization mechanism in HCG 31? What are the physical properties of the TDG candidates? Is the Wolf-Rayet population distributed through the whole system or only in the central zone? All the questions listed above are important to understand the system HCG 31 as a whole. Indeed, no previous work has been able to study the system on this way given the instrumental limitations. In this context, our principal goal is to understand the physical and kinematical state of HCG 31. In this thesis we perform a deep study of the Hickson Compact Group 31. In order to achieve our goal, we raise the following general and specific objectives.

General objectives:

• Characterize the physical properties of the merging system HCG 31, to fully understand its state of interaction.

Specific Objectives:

- Determine physical parameters
- Determine chemical abundances
- Determine the ionization mechanism
- Determine star formation rates

Chapter 3

Data

3.1 Type of data used: integral field spectroscopic observations

The integral field spectroscopy (IFS, also commonly named integral field unit -IFU-) is a spectroscopic technique frequently used to study extended objects. This is because we obtain a spectrum for every spaxel in a 2D image, turning the classical (X,Y) plane of a 2D image into a 3D datacube with (X,Y, λ), where λ represents the third axis as the wavelength. The 3D output is also called a datacube. It could be defined as the combination of photometry and spectroscopy. In Figure 3.1 there is a representation of the structure of a datacube.

One of the main advantage of using IFS is that we obtain a large spatial coverage of an object with spectroscopic information for all spatial positions. IFS is a great technique to study extended object such as Galaxies, Nebulae, among others. There are many surveys that observe a large number of objects using IFS. e.g The Calar Alto Legacy Integral Field Area Survey (CALIFA) (Sánchez et al. 2012), Mapping Nearby Galaxies at APO (MaNGA, Bundy et al. 2015), among others.

A notable feature of the IFS is the complex instrument structure required. There are three types of instrument designs for IFS:

- 1) Lenslets: It consists of a pure lenslet array that takes the spectra directly into the CCD. Its principal disadvantage is the inefficient CCD usage, e.g SAURON (Bacon et al. 2001).
 - 2) Lenslets + Fibers: It is the same principle as the lenslet array but it has

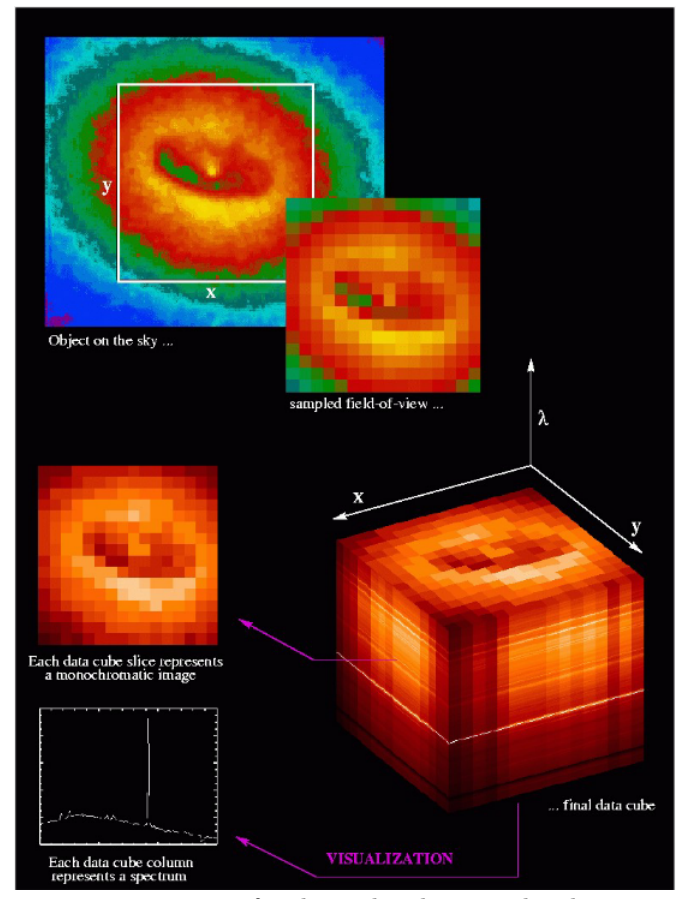


Figure 3.1: Schematic representation of a datacube showing the three principal axis (X,Y,λ) . Figure taken from Roth et al. (2002)

optical fibers connected to each lenslet in order to obtain a better usage of the CCD. But disadvantage is their small Field of View. E.g GMOS at Gemini South (Allington-Smith et al. (2002)).

3) Slicer: For this technique, the light coming from the extended source is segmented into several slices. Every slice is reflected into different directions. Then the light from the goes to the diffraction grating to finally get to the CCD. MUSE at the Very Large Telescope (VLT) uses this technique (Bacon et al. 2004).

Figure 3.2 shows representation of the three different types of IFS techniques.

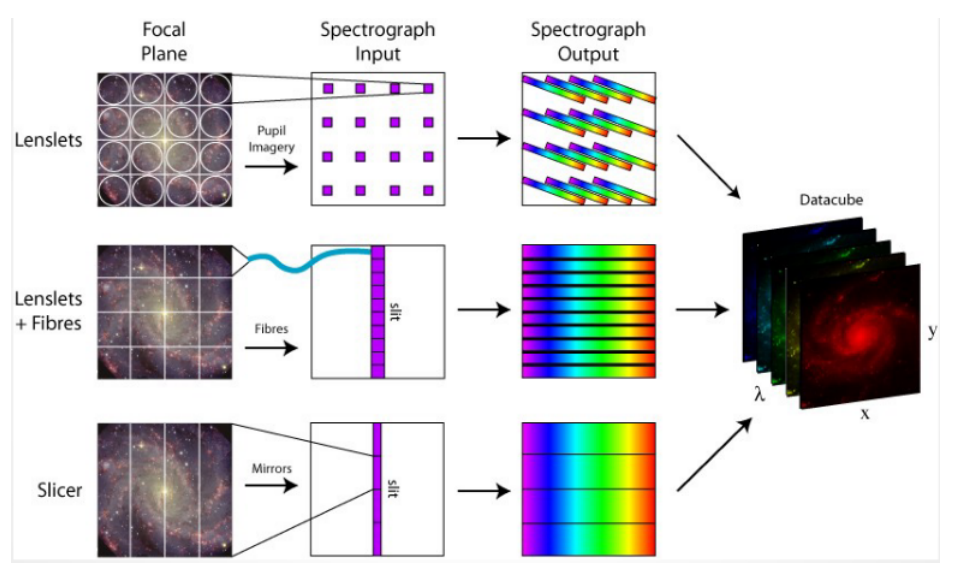


Figure 3.2: A representation of the three different types of instruments that creates datacubes. Lenslets, Lenslets + fibers and Slicer. Image taken from Allington-Smith et al. (1998)

3.2 Observations and data reduction

The Hickson Compact Group 31 was observed during the nights of February 18-20 of 2014. In order to obtain a larger spatial coverage, four different Field-of-View (FoV) were observed. In Figure 3.3 we represent all the FoVs observed over the r' band image taken by Mendes de Oliveira et al. (2006). The data was acquired in the Wide Field Mode (WFM), where each field covers a field-of-view of 1x1 arcmin², with a spatial sampling of 0.2" and a spectral range of $4750-9350\,\text{Å}$ at $1.25\,\text{Å}$ sampling. The mean seeing during the observations was of $\sim 0.9\,\text{arcsec}$, with a mean airmass of 1.15. During the nights the seeing ranged from $\sim 0.81\,\text{arcsec}$ to $\sim 1.01\,\text{arcsec}$ Taking into account the distance to the system (59.38 Mpc) our mean seeing implies a spatial resolution of $\sim 252\,\text{pc}$, and each spaxel cover $\sim 56\,\text{pc}$, and each FoV cover an area of $\sim 16.8\,\text{x}\,16.8\,\text{kpc}$.

The archival data of HCG 31 was taken during the year 2014 as part of the science verification strategy. The data was reduced by Thierry Contini. The reduced data was provided us by Philippe Amram (Laboratoire d'e Astrophysics de Marseille, France). The data was fully tested by the Marseille team. The team used the standard ESO pipelines for the data reduction.

In figure 3.4 we present a RGB image of the datacube using different strong emission-lines of gas with red representing H α in the range 6647 \mathring{A} - 6654 \mathring{A} , green

	Field 1	Field 2	Field 3	Field 4
Date	2014-02-18	2014-02-19	2014-02-19	2014-02-20
Time	00:13:24	00:13:20	01:03:25	01:43:22
Date	2014-02-18	2014-02-19	2014-02-19	2014-02-20
Time	00:36:07	00:35:35	01:25:52	02:05:31
Date	_	_	2014-02-20	2014-02-20
Time	_	_	00:21:53	02:27:13
Date	_	_	2014-02-20	_
Time	_	_	00:52:14	_
Date	-	-	2014-02-20	-
Time	_	_	01:14:02	_
t_{exp} [s]	1200	1200	1200	1200
n_{exp}	2	2	5	3
Mean air mass	1.078	1.081	1.127	1.304
Mean seeing ["]	0.87	0.98	1.01	0.81

Table 3.1: Observation log for the four IFU fields observed with MUSE $\,$

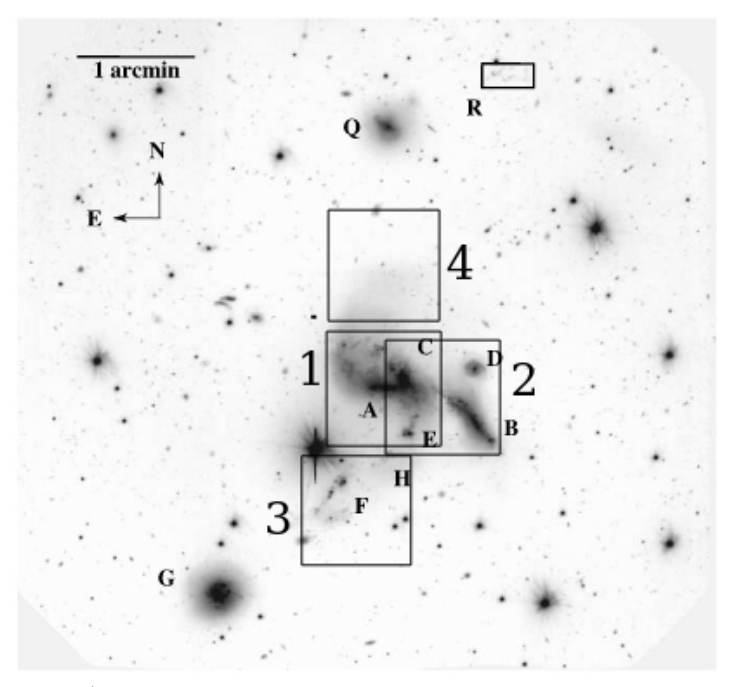


Figure 3.3: GMOS-N r' band image of the entire system, the black squares show the location of the four IFUs taken by MUSE, the r' band image was taken from Mendes de Oliveira et al. (2006)

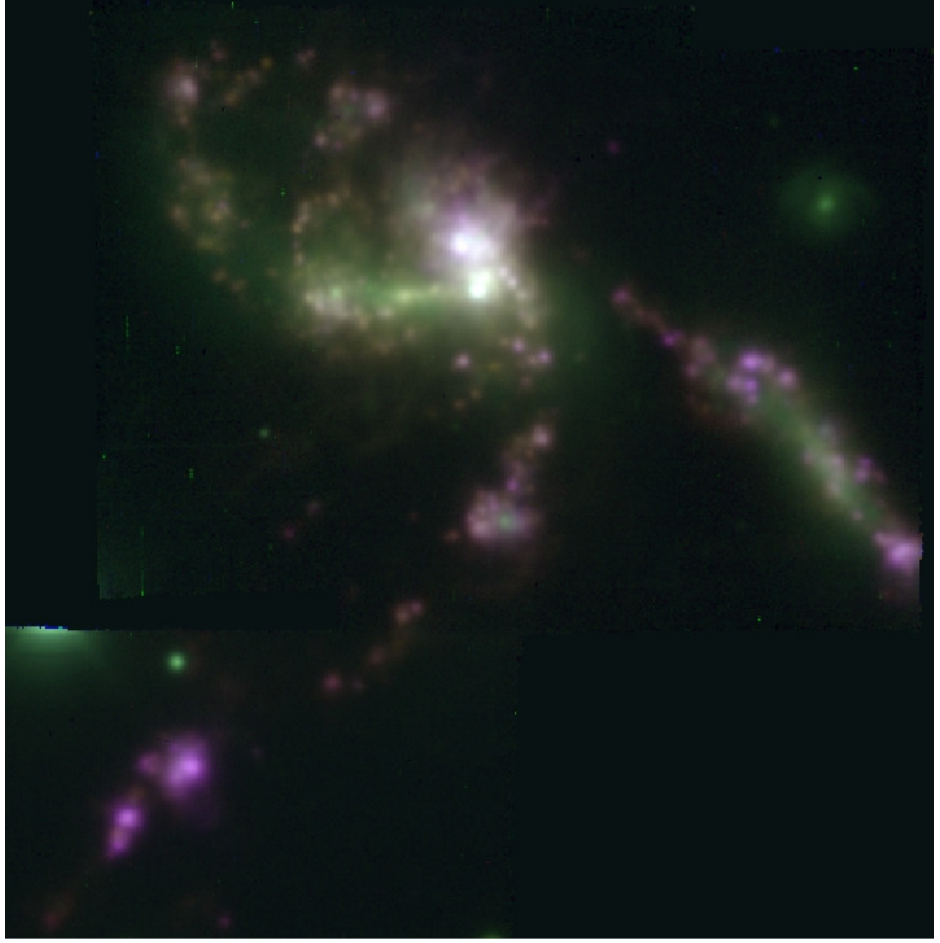


Figure 3.4: RGB image of HCG 31 made collapsing images of different lines. Red represents $\text{H}\alpha$ (6647 Å - 6654 Å), Green represents $[\text{NII}]\lambda$ 6584Å (6667 Å - 6674 Å) and Blue represents $[\text{OIII}]\lambda$ 5007Å (5070 Å - 5078 Å). The wavelength ranges are not corrected by redshift.

representing [NII] λ 6584 $^{\mathring{A}}$ in the range 6667 $^{\mathring{A}}$ - 6674 $^{\mathring{A}}$ and [OIII] λ 5007 $^{\mathring{A}}$ in the range 5070 $^{\mathring{A}}$ - 5078 $^{\mathring{A}}$. The wavelength ranges were not corrected by redshift. In figure 3.5 is shown a colapsed image in the spectral range of H α (6647 $^{\mathring{A}}$ - 6654 $^{\mathring{A}}$) for the four fields. The signal-to-noise ratio (SNR) was measured for every emission line of interest. We collapsed an image for every emission line over the science and variance layer of the datacube. We divide the science image over the square root of the variance, obtaining an SNR map. We found that for field "4" the SNR was < 3 for H α We discarded that field and also the bottom part of field 3.

3 Data 17

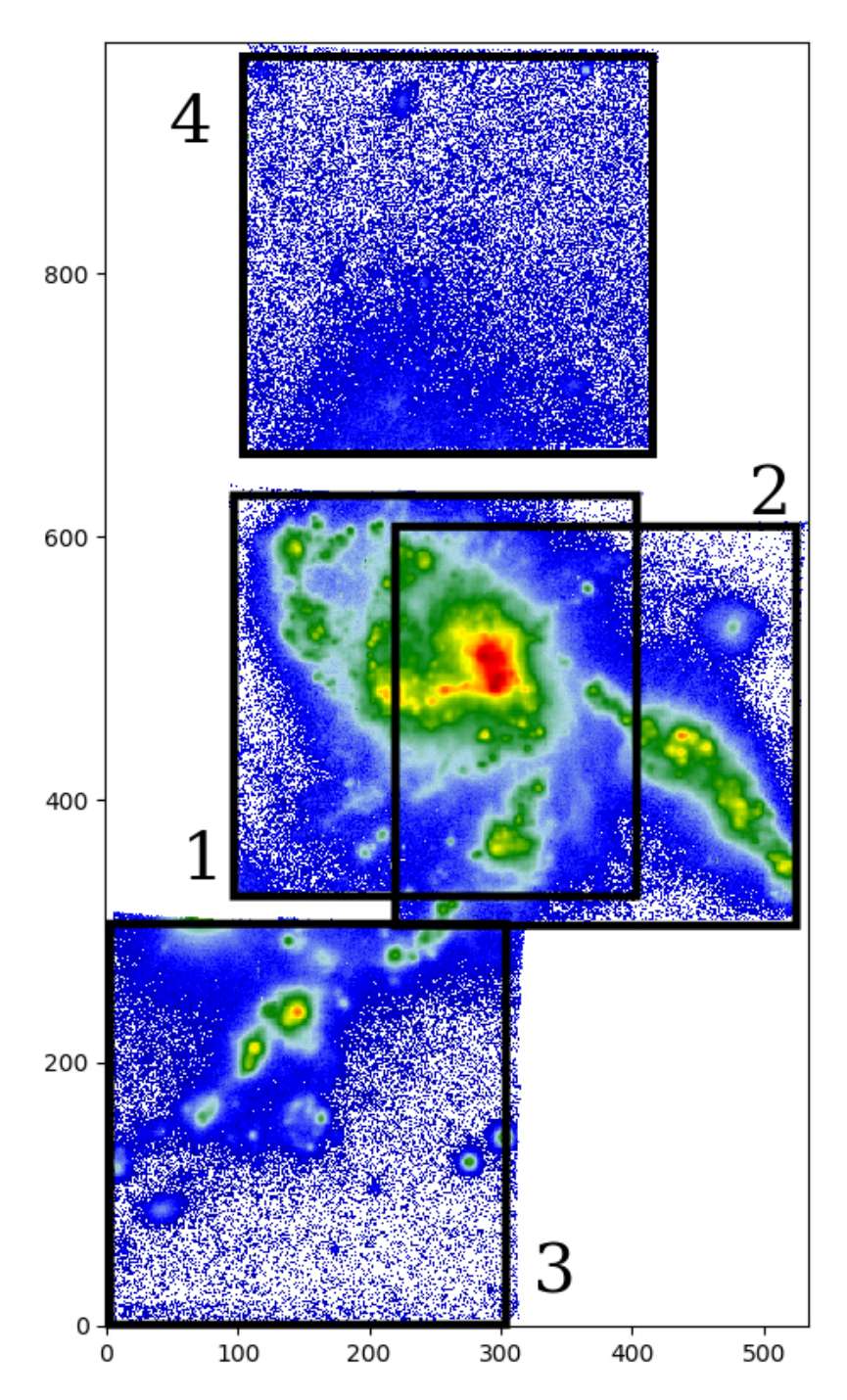


Figure 3.5: H α colapsed image over the entire cube. The wavelength range considered for the image is 6647 Å - 6654 Å.6647 Å - 6654 Å

Chapter 4

Analysis

In this section we present the analysis carried out to determine the different physical parameters and properties of the members of HCG 31. We focus on the methods used to obtain extinction, SFR, physical parameters, ionization mechanism, measure of the line-emission fluxes, the stellar population synthesis (SPS) and kinematics.

4.1 Description of the code FADO

FADO¹ (Fitting Analysis using Differential Evolution Optimization) is a code developed by J.M Gomes & P. Papaderos (2017) which is capable to do a spectral population synthesis and is specially optimized for star-forming galaxies. The main advantage of FADO over others SPS codes is that it is the first one that considers the contribution of a nebular continuum alongside with the stellar continuum. This is useful in galaxies with high SFR (such as HCG 31) because in such system the contamination of nebular continuum could be considerable (e.g. in compact narrow-emission line galaxies).

FADO also allows the fit of the most important emission-line (Balmer recombination lines, forbidden lines such as [OIII] $\lambda\lambda$ 4959, 5007 Å [NII] $\lambda\lambda$ 6548,6584 Å [SII] $\lambda\lambda$ 6717,6731 Å among others), and it measure the emission-lines fluxes and the equivalent widths (EW), and it determine of the physical parameters such as electron density and temperature.

Figure 4.1 shows a schematic view of FADO (extracted from the main paper, Gomes & Papaderos 2017), and it is possible to see how the code works in three

¹http://spectralsynthesis.org/index.html

main stages:

1 - α Pre-process stage, where the code import, rebin the spectra and performs first principal determinations (redshift, 1σ error spectrum, and spectroscopic classification). In addition, the code pick the best fitting strategy (full consistency, nebular continuum or stellar continuum) then, the codes passes to the second stage

- 2 ψ , Differential evolution optimization, where the code performs the onthe-fly measurement of the emission-line fluxes and classification based on the ionization (star-forming, composite or active galactic nuclei), and also the determination of physical conditions of the gas (electron temperature, electron density, and extinction). In this stage the code performs the determination of the stellar population, computation of the hydrogen and helium ionizing photons and other parameters such as predicted Balmer-line luminosities and uncertainties for the individual single stellar populations (SSP) used in the fit. Finally, the code passes to the third stage
- 3 ω , Output, where the final measurements of emission-line fluxes & EW are performed (with its uncertainties), and the computation of evolutionary quantities such as stellar mass, age and metallicity (both weighted by light and mass) is done, the results are stored in fits format and also there is a graphical output showing the main results.

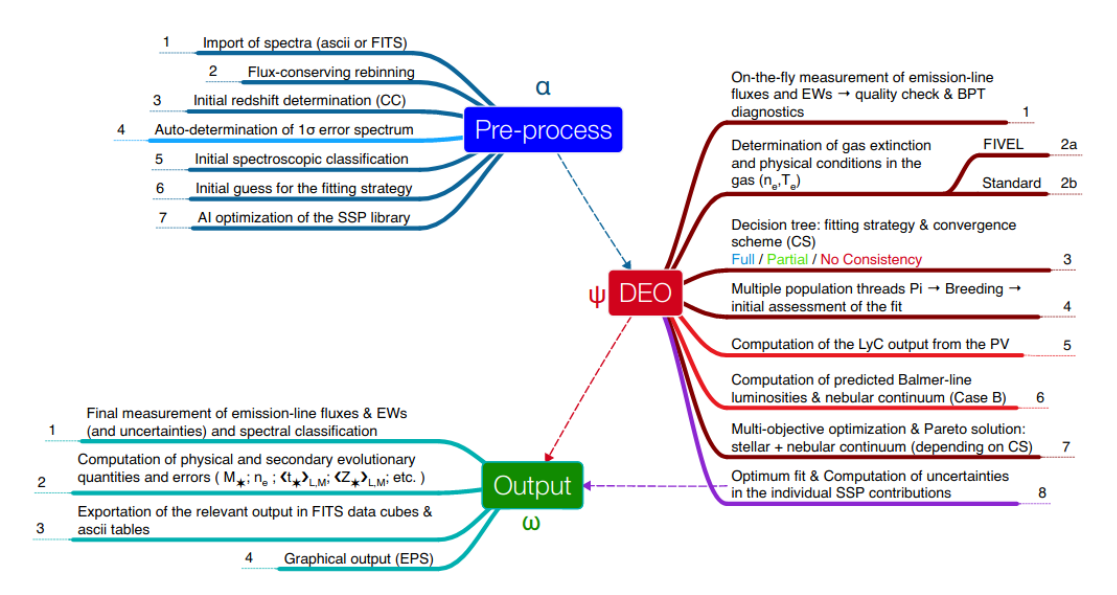


Figure 4.1: Schematic view of FADO Showing the function of their three main stages. Figure extracted from Gomes & Papaderos (2017)

4.2 Description of the code IFSCUBE

IFSCUBE² is a Python routine specifically designed to analyze datacubes of integral field spectroscopy. This code performs a linear fitting to the continuum for every spaxel and then substract it. Over the continuum-free spectra the code performs a single gaussian fitting on each emission line. On each emission line, we define a continuum window of ~ 5 Å on each side in order to perform a good estimate of continuum. It should be noted that we use IFSCUBE as a complementary tool to obtain a full coverage of all the emission lines that we are interested to measure. This is because FADO does not have the line [SIII] λ 9063 on their default set of lines.

We also use IFSCUBE to obtain the kinematic maps of $H\alpha$ because FADO is not optimized to do a kinematic analysis of the spectra

4.3 Emission-line measurement

Measurements of emission lines has been performed with two codes, FADO and IFSCUBE. The first is designed to perform spectral population synthesis and to

²https://ifscube.readthedocs.io/en/latest/

derive different physical parameters from a galaxy spectrum, including emission-line fluxes. The second code is based in a PYTHON³ package of spectral analysis routines that fit Gaussian profiles to the emission lines. We use IFSCUBE to fit the line of sulfur [SIII] λ 9063 and the line [SIII] λ 6312. We use IFSCUBE because FADO includes a default set of emissions lines to be fitted, and [SIII] λ 9063 is out of its range. Due to the low resolution of MUSE spectra (average R ~ 2500) we fit single Gaussian profiles to the observed lines instead of perform a multiple component analysis. In Figure 4.2 we show several line profiles observed with MUSE, as examples. On this Figure we included the profiles of H $\beta\lambda$ 4861, [OIII] λ 5007, [OI] λ 6300, [SIII] λ 6312, H $\alpha\lambda$ 6562, [NII] λ 6584, [SII] $\lambda\lambda$ 6717,6730, [ArIII] λ 7135 and [OII] $\lambda\lambda$ 7319,7330. The x-axis represents the wavelength and the y-axis represent the relative flux. The fit performed by FADO over the observed lines is represented by the red segmented line.

In Figure 4.3 we present the line-maps obtained for some emission lines (H $\beta\lambda$ 4861, [OIII] λ 5007, [OI] λ 6300, H $\alpha\lambda$ 6562, [NII] λ 6584 and [SII] λ 6717). To made these maps we run FADO over the entire datacube and then we reconstruct the image in a (X,Y) plane. We clean the images from noise including only the spaxels were the signal-to-noise ratio (SNR) is > 3. To measure the SNR we divide the map of the emission line with the map of the same line but in the variance layer of the datacube.

In Figure 4.4 we display the maps of the most important line ratios (I([NII] λ 6584) / I(H α), I([OIII] λ 5007) / I(H β), I([SII] $\lambda\lambda$ 6717,6730) / I(H α), I([OI] λ 6300) / I(H α)). The four maps presented show contours of H α in emission. The contours show the levels of 1.33 × 10⁻¹² $ergs \times s^{-1}$ and 5.62 × 10⁻¹² $ergs \times s^{-1}$ of H α in emission.

³Python Software Foundation. Python Language Reference, version 2.7. Available at http://www.python.org

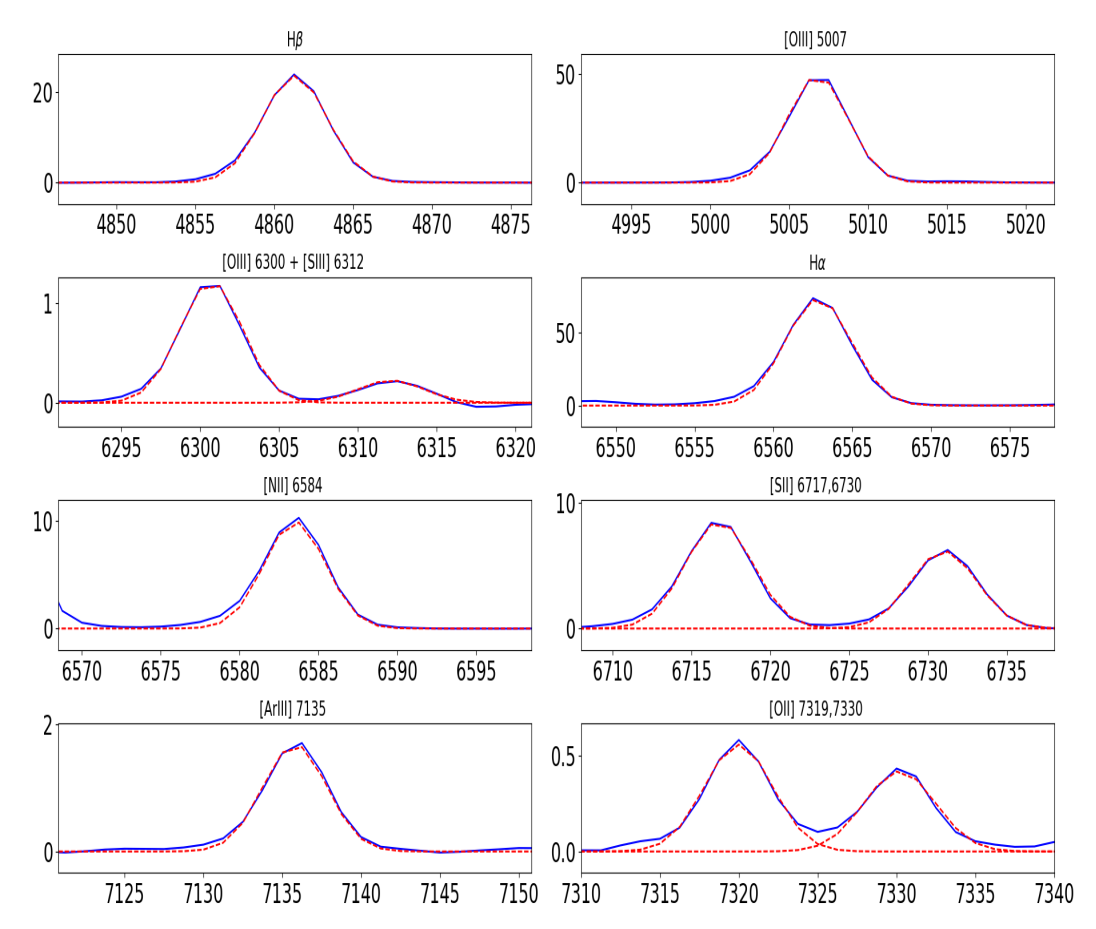


Figure 4.2: Continuum-substracted emission lines of a spaxel in the central zone of HCG 31, the red dotted line represent the fit performed by FADO. The blue line represents the emission lines of the spectra. The X axis represents wavelength and the Y axis the relative flux

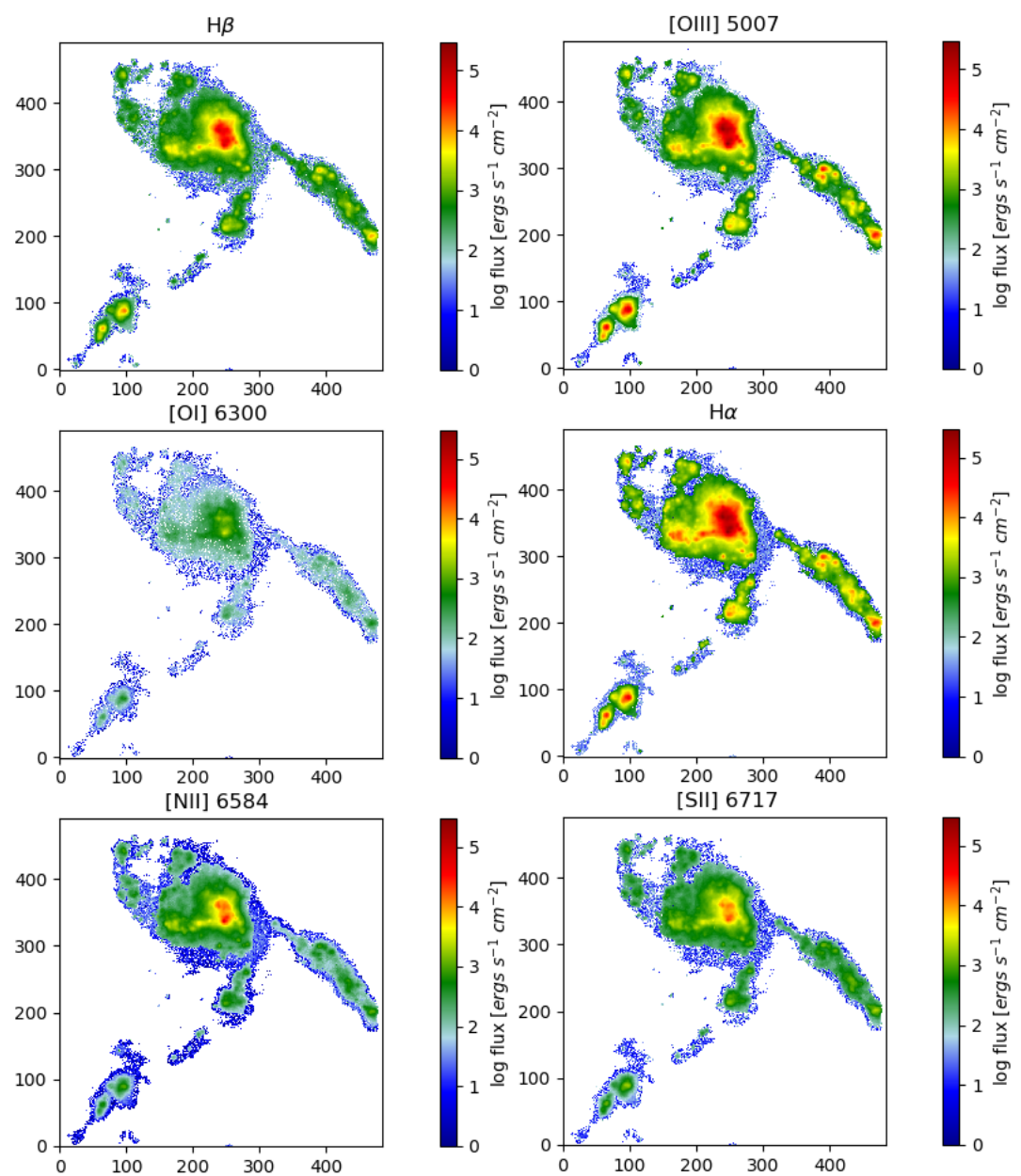


Figure 4.3: Emission-line flux maps of HCG31 obtained with FADO, the lines are H β , [OIII] λ 5007 Å, [OI] λ 6300 Å, H α , [NII] λ 6584 Å, and [SII] λ 6717 Å. The maps are in pixel coordinates and the scale color represents the flux. All colorbars are normalized to the maximum flux in H α

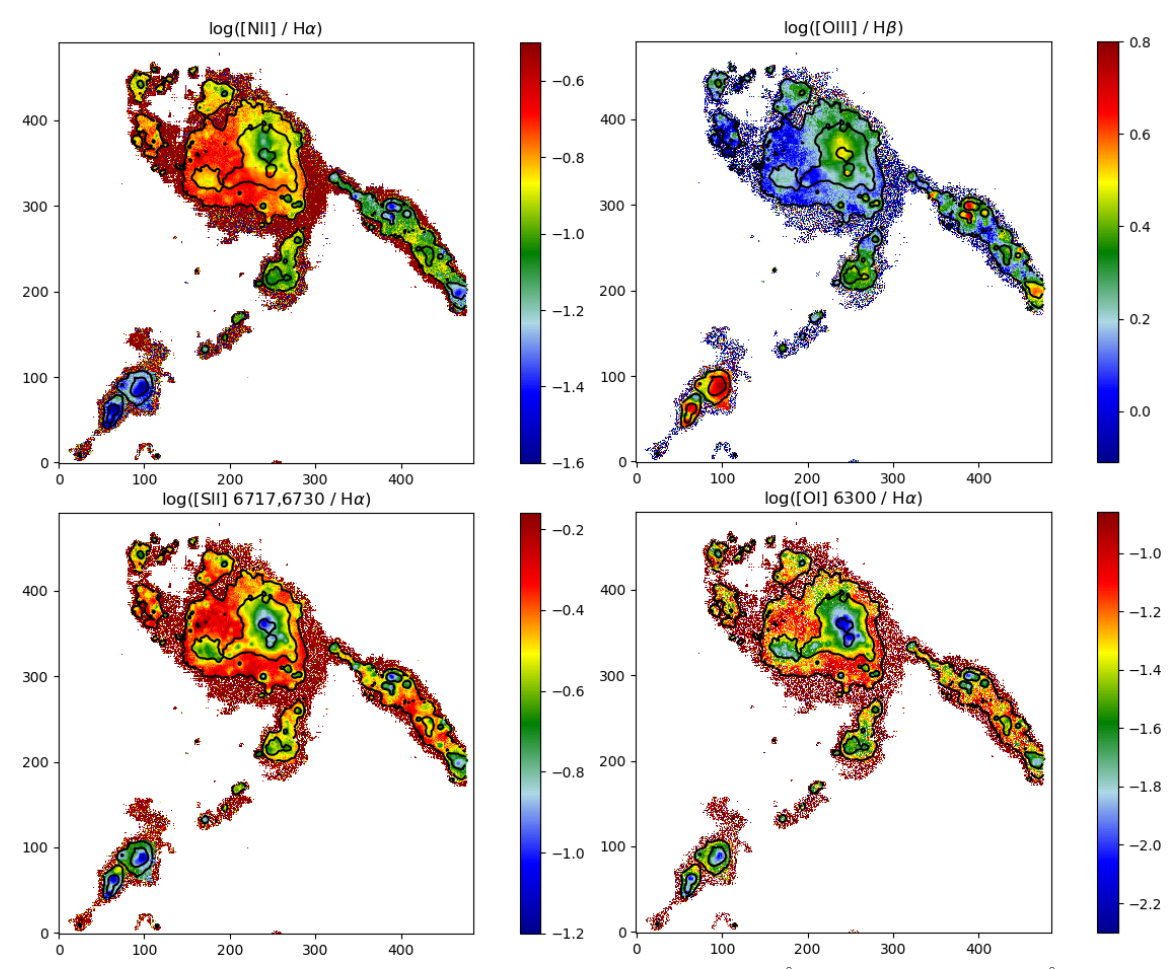


Figure 4.4: Emission-line ratio maps of [NII] $\lambda\,6584\,\text{Å/H}\alpha$, [OIII] $\lambda\,5007\,\text{Å/H}\beta$, [SII] $\lambda\lambda\,6717,6731\,\text{Å/H}\alpha$ and [OI] $\lambda\,6300\,\text{Å/H}\alpha$, the contours in all the maps are of H α emission. The maps are in pixel coordinates.

4.4 Stellar population synthesis

One of the best way to study stellar populations, once is not possible to resolve individually the stars in some astrophysical object, is through synthetic population models. By using this method, it is possible to infer the stellar content of a spectrum by fitting a synthetic stellar population to the observed data. To do that one needs four main components: i) an initial mass function, ii) SFR, iii) isochrones, and iv) stellar spectra. The latter is usually taken from different libraries (e.g. Bruzual & Charlot 2003).

In the literature it is possible to find a wide range of spectral populations synthesis codes, such as pPXF (Cappellari & Emsellem 2004, Cappellari 2017), or STARLIGHT (Cid Fernandes et al. 2005). Almost all of such codes fits different synthetics stellar populations to the stellar spectral features, intending to find the most representative stellar population of a spectrum to derive metallicities, mass and kinematics of that population.

For galaxies displaying a weak continuum level and thus, very weak stellar features in the spectrum, usually a population synthesis is not applied, because it will carry a lot of uncertainties due to the almost unobservable stellar absorption lines. Therefore, studies focused on theses systems just measure the intensities of the lines directly from the observed spectrum.

The main issue with almost all of SPS codes is that they neglect the contribution of nebular continuum, which is produced mainly by the free-free radiation on the HII regions (Gomes & Papaderos 2017). This could lead to systematic biases on the determination of the mass of the stellar population.

In this work we made use of the code FADO which allow us to fit the most important emission lines with a subtraction of the stellar and nebular continuum. In order to complement the analysis, we made use of the code IFSCUBE which also performs Gaussian fit to the emission-lines. It should be noted that, despite we use SPS models. Our analysis in this thesis cannot be focused on the stellar populations because the weak continuum. But we are going to use some of the results e.g the stellar mass and the ages.

4.5 Kinematics

4.5.1 Radial velocity

Using the Doppler shifts of the spectral lines it is possible to calculate the velocity on the line-of-sight of the gas. This velocity is called radial velocity and is denoted with v or V_r . This velocity is given by:

$$V_r = \frac{\lambda_{obs} - \lambda_0}{\lambda_0} \times c \tag{4.1}$$

where λ_{obs} is the wavelength of the observed emission line, λ_0 is the wavelength of the emission line in the rest frame, and c represents the speed of light in a vacuum ($\sim 299792458~ms^{-1}$). Positive radial velocities implies that the object is moving away from the observer.

The uncertainties of radial velocity were calculated using the recipes given by Lenz & Ayres (1992) and using the fitting parameters derived by using IFSCUBE.

4.5.2 Velocity dispersion

The width of a Gaussian profile is usually determined by the full width at half maximum (FWHM) which, in this case, is measured in angstroms. The standard deviation (σ) is related to the FWHM through FWHM = $2\sqrt{2ln2}\times\sigma\approx~2.35\times\sigma$.

The emission lines are produced by the bound-bound transitions of an electron between the different energy levels in an atom. This transition has a characteristic energy that could be detected in absorption or emission in a spectrum. However, due to the uncertainty principle this energy is not infinitely sharp. This fact, besides that the atoms are moving relative to us produce a broadening in the spectral lines. In this sense, emission lines can be fitted with a gaussian, where the standard deviation of the gaussian represents the velocity dispersion of the atoms, providing information about its broadening mechanism.

The observed velocity dispersion (σ_{obs}) is affected by several broadening mechanisms (Melnick et al. 1999). The principals broadening mechanisms in GHIIRegions are:

1. Thermal broadening: with a characteristic width of $\sigma_{th} = \sqrt{kT_c/m_H} \approx 9.1 km \ s^{-1}$ (assuming $T_c = 10^4 K$)

2. Virial broadening: this is an effect of the gravitational field of the region. Its width is given by $\sigma_{vir} = \sqrt{GM_T/R_G}$. With M_G represents the total mass and R_G the radius of the mass distribution (generally, M_G and R_G are difficult to determine observationally)

3. Expanding shells and filaments: This contributes usually to the wings of the gaussian profiles, due to the contribution of stellar winds.

There is also another broadening mechanism that affects the observed width of the gaussian. The instrumental broadening σ_i which is produced by several instrumental effects e.g the width of the slit.

We do not consider the virial broadening because it is difficult to calculate it. Thus, we consider as the intrinsic velocity dispersion (σ_{int}) the result of the following equation.

$$\sigma_{int}^2 = \sigma_{obs}^2 - \sigma_i^2 - \sigma_{th}^2 \tag{4.2}$$

For the instrumental width we use a standard σ_{inst} for MUSE, which has been taken from the literature (Bellocchi et al. 2019, $\sigma_{inst} = 50 \, km s^{-1}$).

The uncertainties of σ_{obs} where calculated using the formulation given by Lenz & Ayres (1992) with the fitting parameters of IFSCUBE.

4.6 Interstellar extinction correction

Once an observed spectrum of an astrophysical source is reduced and calibrated, it is necessary to correct them for interstellar reddening. This effect is caused by the interstellar dust which scatters light of stars and nebulae, making them redder. The reddening effect depends inversely on wavelength and conventionally it is quantified through the color excess for the (B-V) index, as follows:

$$E(B-V) = (B-V) - (B-V)_0 \tag{4.3}$$

where (B-V) corresponds to the observed color and $(B-V)_0$ to the intrinsic color of the source. The extinction is the absorption and scattering of the light by dust and gas between an astronomical object and the observer. The extinction at a wavelength λ is given by:

$$A_{\lambda} = 2.5 \times log(F_{\lambda}^{0}/F_{\lambda}) \tag{4.4}$$

where F_{λ} corresponds to the observed flux at λ and F_{λ}^{0} is the flux without the absorption effect.

The relation between E(B-V) and A_V is given by the extinction factor R_V , which is defined as

$$R_V = \frac{A_V}{E(B-V)} \tag{4.5}$$

It should be noted that $E(B-V)=A_B-A_V$ where A_B and A_V corresponds to the value of extinction at the central wavelength of the filters ($\sim 4400 \text{Å}$ for B and $\sim 5500 \text{Å}$ for V).

The value of R_V depends on the nature of the dust grains in the Interstellar Medium (ISM), i.e. the shape, composition, and size (Osterbrock 1989).

A different extinction law needs to be applied to each object depending on its nature (e.g. starburst galaxy, quiescent galaxy, etc), which should be applied in addition to the extinction produced by the Milky Way. In case of HCG1 we choose to use Fitzpatrick (1999) law for galactic correction and Calzetti et al. (2000) law for intrinsic extinction.

4.6.1 Fitzpatrick law

The Galactic extinction curve has been studied by several authors (e.g. Cardelli et al. 1989; Fitzpatrick 1999 among others). In this thesis we use the curve derived by Fitzpatrick (1999), which covers from UV to IR. In Figure 4.5 I show the extinction curve derived by Fitzpatrick alongside with the curves of Cardelli et al. (1989) and Seaton (1979).

It can be seen from Figure 4.5 that the behavior of the three curves is similar, except in the fuv rise region. Also, the inversely proportional relationship between extinction and wavelength is clearly shown. In the IR region we see a slowly increase that the author called power law. In the optical region, where our data is, we see a slight rise called knee. In the NUV region we see a considerable increase, but in a relatively narrow range, called bump. Finally, in the fuv rise when a systematic increase of extinction is seen. In the Milky Way, the value of R_V range between 2.1 to 5.8 depending on the line-of-sight, with an average of $R_V \sim 3.1$ according to Fitzpatrick (1999).

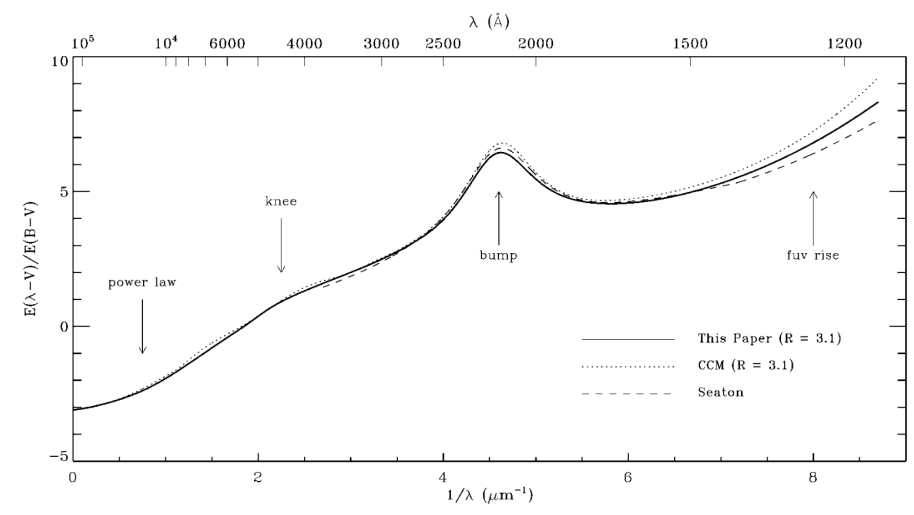


Figure 4.5: Extinction curve for the Milky Way derived by Fitzpatrick (1999) (solid line), also there is the curve derived by Cardelli et al. (1989) (dotted line) and Seaton (1979) (segmented line). The three curves assume $R_V = 3.1$. Figure taken from Fitzpatrick (1999)

4.6.2 Calzetti law

Calzetti et al. (1994) studied the extinction properties in a sample of 39 Starburst and Blue Compact Galaxies observed in UV and optical. They compared their observations with five different grain dust distribution models, using the extinction curves of the Milky Way and Magellanic Clouds. The different models are schematized in Figure 4.6:

- 1. Uniform dust screen. The model used to correct the extinction for single stars, consists of a screen of dust located between the observer and the source.
- 2. Clumpy dust screen. As model 1, but the dust has a clumpy distribution, this model is more realistic than 1.
- 3. Uniform scattering slab. On this model the dust is located closer to the source than model 1, causing scattered radiation may now return to the line of sight.
- 4. Clumpy scattering slab. As in model 3, but dust with a clumpy distribution.
- 5. Internal dust. On this model dust and ionized gas are mixed.

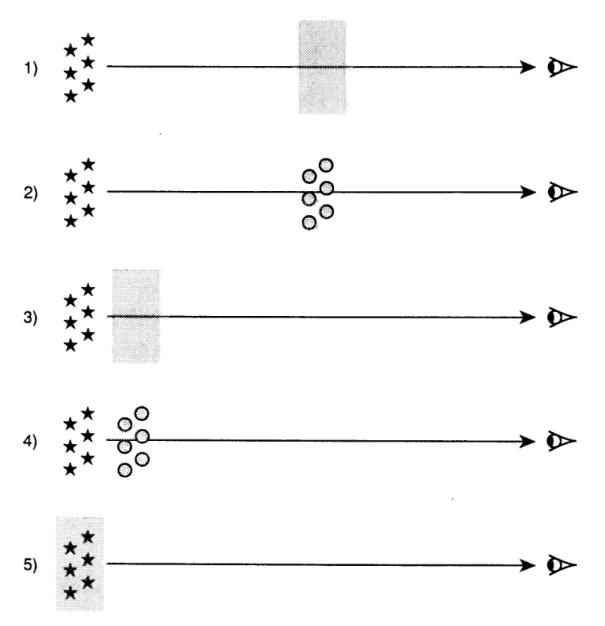


Figure 4.6: Schematic view of the five models describing the dust distribution. Figure taken from Calzetti et al. (1994)

The authors find that none of the models explain the dust configuration in their sample of galaxies, which display high star SFRs, probably due to the complex dust distribution in such galaxies. The authors propose a new extinction curve for this type of galaxies, which is a cubic polynomial.

To complete the study Calzetti et al. (2000) modeled the dust emission in eight Starburst galaxies at low-redshift through FIR photometry ($\lambda > 40 \,\mu m$) from the *Infrared Astronomical Satellite* (IRAS) and Infrared space observatory (ISO). They find that the Spectral Energy Distribution (SED) in the FIR is well represented by two Planck functions, one representing warm dust ($\sim 40 \,\%$ of the emission) and other representing cold dust ($\sim 60 \,\%$ of the emission).

In order to obtain E(B-V), the Balmer decrement $(I(H\alpha)/I(H\beta))$ should be determined. Following Osterbrock (1989), the theoretical value of this ratio at $T = 10^4 K$ and $n_e = 10^2 \, cm^{-3}$ is 2.86. Then, E(B-V) is estimated by using the following equation (Domínguez et al. 2013):

$$E(B - V)_{gas} = 1.97 \times log\left(\frac{(H\alpha/H\beta)_{observed}}{2.86}\right)$$
 (4.6)

It should be noted that in the extinction curve of Calzetti et al. (2000) a value of $E(B-V)_{stellar}$ is needed, i.e. the extinction of the stellar continuum rather

than the extinction of gas, fortunately, Calzetti et al. (2000) give an expression to calculate this value from $E(B-V)_{gas}$.

$$E(B-V)_{stellar} = (0.44)(\pm 0.03) \times E(B-V)_{gas}$$
 (4.7)

4.7 Star Formation Rate determination

The SFR is a key process in galaxy evolution and represents the amount of gas that is converted into stars per unit of time. Usually is measured as solar masses per year, and is a very important and interesting research topic by itself (see Kennicutt & Evans 2012 for a complete review of star formation in nearby galaxies).

The physical processes behind the star formation involves the physics of atomic and molecular gas on the ISM of galaxies. The actual view of this process consists on the gravitational collapse of a molecular cloud into clumps that form single or binary stars, or even star clusters, depending on the mass of the clump Kennicutt & Evans (2012).

One of the most convenient ways to estimate SFR is taking advantage of its relationship with the density of the gas, using the Kennicutt-Schmidt relation (Schmidt 1959, Kennicutt 1998b)

$$\Sigma_{SFR} = \Sigma_{gas}^{N} \tag{4.8}$$

where N = 1.4 - 1.5 (Kennicutt 1998b)

The mass distribution of the new young stars depends on the initial mass function (IMF). The massive OB stars ($M > 15M_{\odot}$) have an intense UV emission and ionize their surrounding gas, converting the HI envelope into an HII region, and due to the detailed balance, every ionization is followed by recombination. These recombinations produce strong emission-lines (ELs) observed in the spectra of a galaxy (i.e. Balmer series in optical, Lyman Series in UV, Paschen series in IR). Indeed, the spectra of a star-forming galaxy has very strong ELs, both from recombination (e.g. $H\alpha$, $H\beta$, among others) and forbidden lines (e.g. [OIII] $\lambda 5007$ Å, [NII] $\lambda 6584$ Å, [SII] $\lambda \lambda 6717,6731$ Å among others).

Using this relation with recombination EL intensity and the SFR, Kennicutt (1998a) derived one of the most widely used relations to estimate SFR, assuming

a Salpeter IMF with $M=1-100M_{\odot}$ as mass limits:

$$SFR(M_{\odot}yr^{-1}) = 7.9 \times 10^{-42} \times L(H\alpha)(ergs^{-1})$$
 (4.9)

Kennicutt & Evans (2012) reviewed the most used SFR calibrators to date, and they refined the equations, including for $H\alpha$. They propose, for $L(H\alpha)$, the following expression, assuming a Chabrier IMF, and a continuous SF process:

$$logSFR(M_{\odot}yr^{-1}) = logL(H\alpha)(ergs^{-1}) - 41.27$$
 (4.10)

There are also, more SFRs calibrators that are widely used in literature:

- UV continuum luminosity. As explained above, most of the light of the massive stars comes in the UV range, at $\lambda 1500\text{-}2800\,\text{Å}$, making it a good calibrator of SFR.
- [OII] λ 3727 Å forbidden line. This line is well related with $H\alpha$ flux, thus it is a good SFR calibrator. Usually, this method is more used on high redshift galaxies, but has more dispersion than using $H\alpha$.
- Total infrared (TIR) continuum luminosity. Dust absorbs approximately half of the light coming from stars, making the dust emission at λ 10-300 μ m a good tracer of SFR.

On this thesis, we use $H\alpha$ as tracer of SFRs, given that we did not have the whole spectral coverage to use UV or IR calibrators. The uncertainties are calculated propagating the flux errors given by FADO and using an uncertainty on the distance of 4.16 Mpc (taken from *Nasa Extragalactic Database* (NED)).

4.8 Physical properties

On this section we explain the equations and literature used on this thesis in order to determine the different physical properties in our data. This type of analysis is important because it give us information about the interstellar medium and it helps us to derive the ionic chemical abundances on the gas. The determination of the electron temperature and density is associated with the chemical abundances. The better way to do that is using the so-called auroral lines. Unfortunately, on this thesis we do not have the fluxes of the auroral lines related

with Oxygen and we just have Sulfur information. Thus, we have to use empirical calibrators in order to estimate the oxygen temperature.

4.8.1 Electron temperatures

The electronic temperature of a physical region could be determined using the relationship between the emission lines of some ion with a p^2 configuration. And different excitation energies in the same wavelength regime, since the relative excitation rates for the upper and lower levels depend widely on temperature.

For example, some important emission-line ratios are I([OIII] λ 4959 \mathring{A} + [OIII] λ 5007 \mathring{A}) / I([OIII] λ 4363 \mathring{A}) and I([NII] λ 6548 \mathring{A} + [NII] λ 6583 \mathring{A}) / I([NII] λ 5755 \mathring{A}). The lines [OIII] λ 4363 \mathring{A} and [NII] λ 5755 \mathring{A} are the so-called auroral lines and are very sensitives to temperature.

The spectral coverage of the current data set does not allow us to measure the needed lines to estimate directly $T_e([OII])$ or $T_e([OIII])$. In fact, we only have the auroral lines [SIII]6312 Å and [OII]7319,7330 Å, so we need to use the empirical relations between these temperatures. Considering the [SIII]6312 Å line, [SIII]9069 Å line, and using the relation $I(9532\text{Å}) \approx 2.44 \times I(9069\text{Å})$, we are able to measure directly the ionic temperature of S^{2+} , $T_e([SIII])$. However, it is necessary to calculate the R_{S3} coefficient.

Owing to the limitation of the spectral range of our data, we were not able to measure the [OII] $\lambda\lambda$ 3727,3729 Å emission-lines and the auroral line [OIII] λ 4363 Å needed to estimate the respective [OII] and [OIII] electron temperatures using the direct method. However, it is possible to measure the auroral lines [SIII] λ 6312 Å and to estimate the [SIII] temperature using the direct method.

We calculate $T_e([SIII])$ with the formula given by Hudson et al. (2012)

$$T_e([SIII]) = 0.517 + 0.0003187 \times R_{S3} + \frac{23.64041}{R_{S3}}$$
 (4.11)

where the R_{S3} coefficient is given by the formula:

$$R_{S3} = \frac{I(9069) + I(9532)}{I(6312)} \tag{4.12}$$

which has a precision of $\sim 1\%$ in the temperature range $0.6 < T_e([SIII]) < 1.5$.

The electron temperature $T_e([OIII])$ was calculated from $T_e([SIII])$ using empirical relation fitted by Hägele et al. (2006),

$$T_e([SIII]) = (1.19 \pm 0.08) \times T_e([OIII]) - (0.32 \pm 0.10)$$
 (4.13)

Using the empirical temperature relations, we can estimate the [OII] and [SII] electron temperatures. The $T_e([OII])$ was derived using the empirical temperature relation with $T_e([OIII])$ given by Pagel et al. (1992) and based on the models of Stasińska (1990),

$$T_e([OII]) = \frac{2}{T_e([OIII])^{-1} + 0.8}$$
 (4.14)

The electron temperature $T_e([SII])$ was calculated from $T_e([OII])$ using the relationship based on photoionization model derived by Pérez-Montero & Díaz (2003),

$$T_e([SII]) = 0.71 \times T_e([OII]) + 0.12$$
 (4.15)

The $T_e([NII])$ can be calculated using the 5755 \mathring{A} auroral line, but usually this line is very weak or contaminated with stellar features such as the red WR bump at 5808 \mathring{A} . In cases where this line is not detected, it is possible to use the classical approximation $T_e([NII]) \approx T_e([OII])$ (PM17).

4.8.2 Electron density

In order to estimate the density of free electrons it is possible to use the relationships between two emission line intensities. These emission lines should be from the same ion. Corresponding to transitions from the same level to different levels but with similar excitation energies. If these two levels have different radiative transition probabilities, the relative population will depend essentially on the electron density. That is the case for ions with a p³-type configuration. Some examples of ions with that structure are O^+ , S^+ , Cl^{++} and Ar^{++} . In figure 4.7 it represented the variation of the line ratios in function of density for two different doublets: $[OII]\lambda\lambda$ 3729, 3726 Å and $[SII]\lambda\lambda$ 6717, 6731 Å.

In order to derive electron densities, one of the mostly used approaches is to use line ratios of some doublets sensitive to changes in electron density. In the low-excitation regime, the coefficient from [OII] $\lambda\lambda$ 3727,3729 Å and [SII] $\lambda\lambda$ 6717,6730 Å

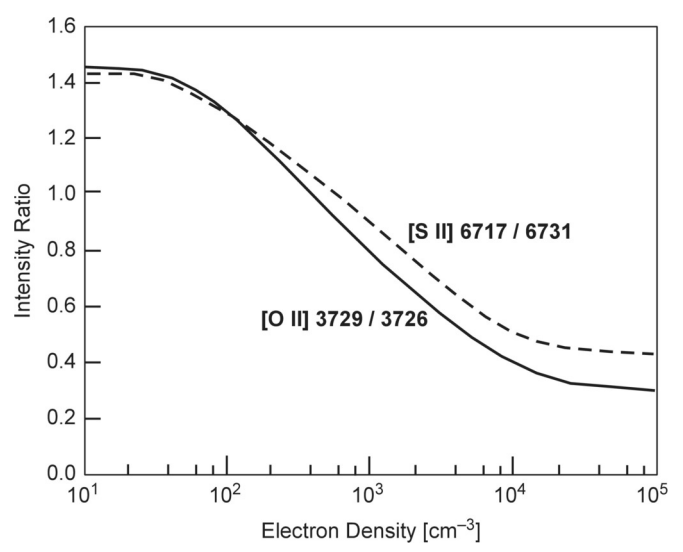


Figure 4.7: Variation of the intensity ratios in function of the density of free electrons for two different doublets: [OII] $\lambda\lambda$ 3729, 3726 Å and [SII] $\lambda\lambda$ 6717, 6731 Å. For this plot it is assumed an electron temperature of $T_e = 10.000$ K. Figure taken from Osterbrock (1989)

are used. In this thesis, we use the [SII] doublet because the [OII] lines are not in our spectral range.

The [SII] coefficient used is R_{S2} , which is defined as

$$R_{S2} = \frac{I(6716)}{I(6731)} \tag{4.16}$$

and then the electron density is obtained using the following equation presented in Pérez-Montero (2017),

$$n_e([S_{II}]) = 10^3 \times \frac{R_{S2} \times a_0(t) + a_1(t)}{R_{S2} \times b_0(t) + b_1(t)}$$
(4.17)

where the polynomials fittings are presented in Tayal & Zatsarinny (2010),

$$a_0(t) = 16.054 - 7.79/t - 11.32 \times t$$

$$a_1(t) = -22.66 + 11.08/t + 16.02 \times t$$

$$b_0(t) = -21.61 + 11.89/t + 14.59 \times t$$

$$b_1(t) = 9.17 - 5.09/t - 6.18 \times t$$

$$(4.18)$$

where $n_e([S_{II}]) = 10^4 N_e$ and t is usually $T_e([OIII])$, with $t = 10^4 T_e$.

4.9 Chemical abundances

In this section we explain the equations used to derive the chemical abundances on HCG 31 from the physical parameters of the system. Due to the spectral coverage, we do not measure the oxygen auroral line [OIII] λ 4363 Å. However, we can measure the sulfur auroral line [SIII] λ 6312 Å which, in combination with some empirical relations, allow us to derive the chemical abundances of several species as oxygen, sulfur, argon, helium and nitrogen.

4.9.1 Oxygen abundances

We derive the oxygen abundance using an empirical calibrator, which allow us to obtain its temperature. Usually, to derive the ionic abundances of O^+ and O^{2+} , first it is necessary to measure the doublet [OII] $\lambda\lambda$ 3727,3729 Å and [OIII] $\lambda\lambda$ 4959,5007 Å respectively. Using empirical relations, as the following given by PM17, it is possible obtain the ionic abundance of O^+ :

$$12 + log\left(\frac{O^{+}}{H^{+}}\right) = log\left(\frac{I(3726) + I(3729)}{I(H\beta)}\right) + 5.887 + \frac{1.641}{T_{e}([OII])} - 0.543 \times log(T_{e}([OII])) + 0.000114 \times n_{e} \quad (4.19)$$

where $T_e([OII])$ is obtained as was described in section 4.8.1.

Unfortunately, as mentioned above, we do not have the necessary spectral coverage to obtain the [OII] $\lambda\lambda$ 3727,3729 Å lines. However, an alternative equation to derive the ionic abundance O^+ is given by Kniazev et al. (2003). This expression uses the [OII] $\lambda\lambda$ 7319,7330 Å auroral lines:

$$12 + log\left(\frac{O^{+}}{H^{+}}\right) = log\left(\frac{I(7320) + I(7330)}{I(H\beta)}\right) + 7.21 + \frac{2.511}{T_{e}([OII])} - 0.422 \times log(T_{e}([OII])) + 10^{-3.4} \times n_{e}(1 - 10^{-3.44} \times n_{e})$$
(4.20)

On the other hand, to determine the O^{2+} abundance, we use the expression given by PM17:

$$12 + log\left(\frac{O^{2+}}{H^{+}}\right) = log\left(\frac{I(4959) + I(5007)}{I(H\beta)}\right) + 6.1868 + \frac{1.2491}{T_e([OIII])} - 0.586 \times log([T_e([OIII]) \quad (4.21))$$

with a precision of 0.01 dex in the range $0.7 \times 10^4 K < T_e([OIII]) < 2.5 \times 10^4 K$.

Finally, we calculate the total oxygen abundance assuming the following equation:

$$\frac{O}{H} = \frac{O^+ + O^{2+}}{H^+} \tag{4.22}$$

where it is assumed that most of the oxygen is in the form of O^+ and O^{2+} .

4.9.2 Sulfur abundances

In order to derive the sulphur ionic abundances S^+ and S^{2+} we use $T_e([SII])$ and the intensities of the [SII] $\lambda\lambda$ 6717,6731 Å lines for S^+ . And the $T_e([SIII])$ and [SIII] $\lambda\lambda$ 9069,9532 Å lines for S^{2+} .

We have followed the equations given in PM17 to calculate the Sulfur ionic abundances:

$$12 + log\left(\frac{S^{+}}{H^{+}}\right) = log\left(\frac{I(6717) + I(6731)}{I(H\beta)}\right) + 5.463 + \frac{0.941}{T_{e}([SII])} - 0.37 \times log(T_{e}([SII])) \quad (4.23)$$

$$12 + log\left(\frac{S^{2+}}{H^{+}}\right) = log\left(\frac{I(9069) + I(9532)}{I(H\beta)}\right) + 5.983 + \frac{0.661}{T_e([SIII])} - 0.527 \times log([T_e([SIII])))$$
(4.24)

where we assume $I(9532) \approx 2.44 \times I(9069)$.

In order to estimate the total sulfur abundance we should take into account the contribution of S^+ , S^{2+} and S^{3+} ionic abundances. Because the latter ionization state is not observable, we used the so-called ionization correction factor (ICF), which is defined by:

$$\frac{N(X)}{N(H)} = ICF(X_{obs}) \frac{N(X_{obs})}{N(H)}$$
(4.25)

In the case of the sulfur, an approximation of its ICF is given by Stasińska (1978):

$$ICF(S^{+} + S^{2+}) = \left(1 - \left(\frac{O^{2+}}{O^{+} + O^{2+}}\right)^{\alpha}\right)^{-1/\alpha}$$
 (4.26)

According to Dors et al. (2016) we use $\alpha \approx 3.27$.

4.9.3 Nitrogen abundance

The equation to derive the N^+ abundance is given by (PM17)

$$12 + log\left(\frac{N^{+}}{H^{+}}\right) = log\left(\frac{I(6548) + I(6583)}{I(H\beta)}\right) + 6.291 + \frac{0.90221}{T_{e}([NII])} - 0.5511 \times log([T_{e}([NII]))$$
(4.27)

We derived the N/O ratio assuming the following equation:

$$\frac{N^{+}}{N} = \frac{O^{+}}{O} \tag{4.28}$$

To obtain the total N abundance, we calculated an ICF using the approximation:

$$ICF(N^+) = \frac{O}{O^+} \tag{4.29}$$

4.9.4 Helium abundance

The helium abundance (once ionized, He^+) is estimated using the recombination lines (RL) 4471 Å 5876 Å 6678 Å and 7065 Å and the RL 4686 Å is used to derive the abundance of the helium twice ionized (He^{2+}).

Once the spectra are corrected by stellar and nebular absorption, the abundance of He^+ can be derived independently for each RL with the following equation:

$$y^{+}(\lambda) = \frac{I(\lambda)}{I(H\beta)} \frac{F_{\lambda}(n_e, t_e)}{f_{\lambda}(n_e, t_e, \tau)}$$
(4.30)

where F_{λ} is the theoretical emissivity and f_{λ} is the optical depth function. The theoretical emissivities adopted are given in PM17:

$$F_{5876} = (0.745 - 5.1 \times 10^{-5} \times n_e) \times t_e^{0.226 - 0.0011 \times n_e}$$

$$F_{6678} = (2.612 - 0.000146 \times n_e) \times t_e^{0.2355 - 0.0016 \times n_e}$$

$$F_{7065} = (4.329 - 0.0024 \times n_e) \times t_e^{-0.368 - 0.0017 \times n_e}$$

$$(4.31)$$

where t_e and n_e are the electronic temperature (in units of $10^4 K$) and density (in units of cm^{-3}) respectively. Usually, the electron temperature of [OIII] is used as a estimate of the zone where the He emission arises, and the optical depth function is given by Olive & Skillman (2004). However, for our data we assume $\tau = 1$ because it is not necessary a very precise Helium abundance for two reasons: i) we are not seeking for helium primordial abundance (or another similar study which will require a more precise determination of this abundance), and ii) we do not have the HeII λ 4686 Å line which is necessary to derive the total He abundance. In the context of this thesis, it is not important to have a very precise He^+ abundance determination.

In summary, to obtain the adopted He^+ abundance we averaged the He^+_{5876} , He^+_{6678} and He^+_{7065} ionic abundances.

4.9.5 Argon abundance

The total argon abundance is obtained using the [ArIII] λ 7135 Å [ArIV] λ 4740 Å for the Ar^{2+} and Ar^{3+} ionic abundances, respectively. However, the SNR of the emission-line [ArIV] λ 4740 Å detected in our spectra is very low. Therefore, we have determined the ionic abundance Ar^{2+} using the following expression:

$$12 + log\left(\frac{Ar^{2+}}{H^{+}}\right) = log\left(\frac{I(7135)}{I(H\beta)}\right) + 6.100 + \frac{0.86}{T_{e}([ArIII])} - 0.404 \times log(T_{e}([ArIII]))$$

$$(4.32)$$

where we assume $T_e([ArIII]) \approx T_e([SIII])$.

The total Ar abundance was derived using the ICF given by Pérez-Montero et al. (2007):

$$ICF(Ar^{2+}) = 0.596 + 0.967(1-x) + \frac{0.077}{1-x}$$
 (4.33)

where $x = O^{2+}/(O^+ + O^{2+})$

4.9.6 Empirical calibrations: N2 and O3N2

The methods described in the previous paragraph are quite robust, however, they require the use of different emission lines that could be faint, in low surface brightness regions (such as [SIII] λ 9063, or [OII] $\lambda\lambda$ 7320, 7330). In these cases, we use the strong-line methods as abundance indicators, given that these methods mainly uses strong emission lines.

The most used strong-line method is the R23, which was defined by Pagel et al. (1979):

$$R23 = \frac{I([O_{II}]3726, 3729\mathring{A}) + I([O_{III}]4959, 5007\mathring{A})}{I(H\beta)}$$
(4.34)

Others strong-line methods use very intense recombination and forbidden lines. Some good examples are the N2 and O3N2 empirical calibrator which requires only four intense emission-lines: ${\rm H}\alpha$, ${\rm H}\beta$, ${\rm [OIII]}\,\lambda\,5007\,{\rm \AA}$ and ${\rm [NII]}\,\lambda\,6584\,{\rm \AA}$

The N2 calibrator was defined by Storchi-Bergmann et al. (1994) and is given by the following expression:

$$N2 = log\left(\frac{I([N_{II}]6584\text{Å})}{I(H\alpha)}\right) \tag{4.35}$$

In literature there are different calibrations for this relation (Denicoló et al. 2002, Pettini & Pagel 2004, Pérez-Montero & Contini 2009, Marino et al. 2013). All of these were obtained by calibrating the relations with estimates obtained through the direct method. One disadvantage of this method is its dependence

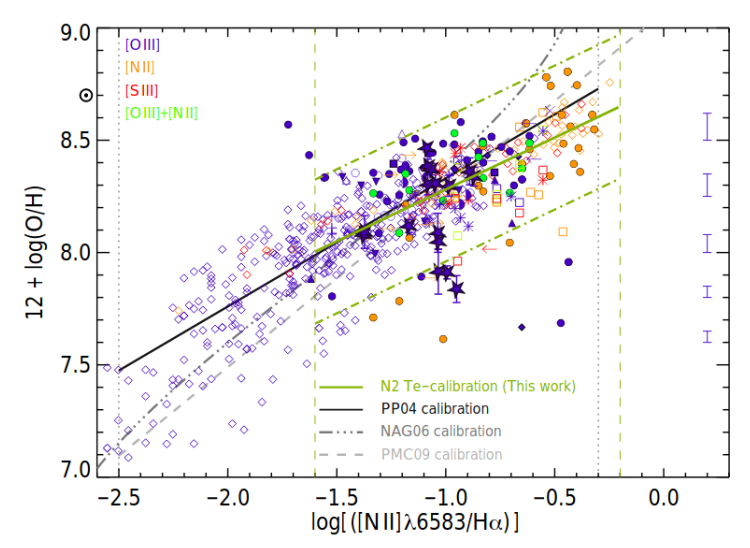


Figure 4.8: Metallicity versus N2 parameter for a sample of HII regions, solid line represents the relation derived by Pettini & Pagel (2004), grey segmented line the fit by Pérez-Montero & Contini (2009), grey dotted line the fit by Nagao et al. (2006) and green solid line represent the fit by Marino et al. (2013), figure taken from Marino et al. (2013)

with the ionization parameter and also with the N/O vs O/H relation (Maiolino & Mannucci (2019)), producing a high dispersion in the relation ($\sim 0.3-0.35$ dex). On the other hand, advantages using thesse methods are: i) it requires a small spectral coverage, and ii) it is completely free of dust absorption.

In Figure 4.8 is presented the calibration of the parameter N2 with respect of the direct method. On the Figure we see a comparison with the calibrations performed by Pettini & Pagel (2004), Pérez-Montero & Contini (2009) and Nagao et al. (2006).

In this thesis, we use the calibration obtained by Marino et al. (2013), which uses data from the survey CALIFA and from literature:

$$12 + log(O/H) = 8.743(\pm 0.027) + 0.462(\pm 0.024) \times N2$$
 (4.36)

which has a valid range of -1.6 < N2 < -0.2, with a dispersion of 0.16 dex.

The O3N2 calibrator was defined by Alloin et al. (1979), and is given by the following expression:

$$O3N2 = \left(\frac{I([O_{III}]5007\mathring{A})}{I(H\beta)} \times \frac{I(H\alpha)}{I([N_{II}]6584\mathring{A})}\right)$$
(4.37)

This parameter has several calibrations with the oxygen abundance (Pettini

& Pagel 2004, Pérez-Montero & Contini 2009, Marino et al. 2013), and it has a dependence with ionization parameter and the N/O ratio (Maiolino & Mannucci 2019). The calibration given by Marino et al. (2013), and used in this work is:

$$12 + log(O/H) = 8.533(\pm 0.012) - 0.214(\pm 0.012) \times O3N2$$
(4.38)

with a valid range of -1.1 < O3N2 < 1.7 and a dispersion of 0.18 dex.

4.10 $H\alpha$ equivalent width and age determination

The H α equivalent width (EW) give us a good estimation of the ratio between ionizing photons of massive stars and continuum photons of the underlying stellar population. The mathematical definition of the EW is given by:

$$EW_{\lambda} = \int \frac{F_l(\lambda) - F_c(\lambda)}{F_c(\lambda)} d\lambda \tag{4.39}$$

where $F_l(\lambda)$ corresponds to the measured flux of certain line at λ and $F_c(\lambda)$ corresponds to the continuum level near to the emission or absorption line. This quantity estimate how large should be the continuum range to integrate near to the line to obtain the same flux of the line.

The EW is commonly used to date star formation events. EW values decrease over time for the evolution of a single stellar population (SSP, a simple population of stars that are all formed at the same time). Then, comparing observations with modelled SSP (e.g. Leitherer & Heckman 1995), it is possible to estimate the ages of past star formation events. One of the models used to estimate ages is given by STARBURST99 (S99) (Leitherer (1990)), which is used in this work.

STARBURST99 generates predictions for the evolution of $EW(H\alpha)$ for two different star-formation laws; i) assuming a SSP, and ii) assuming a continuous star formation process. The predictions are available for five different stellar metalicities: $(2Z_{\odot}, Z_{\odot}, 0.4Z_{\odot}, 0.2Z_{\odot}, \text{ and } 0.005Z_{\odot})$, and for three different initial mass functions, covering ages from 10^6 to 10^9 years.

We choose to use SB99 because it was used in previous analysis on HCG 31, both photometrically (López-Sánchez et al. 2004) and spectroscopically (Alfaro-Cuello et al. 2015). Therefore, we will be able to compare our findings with those results.

4.11 Ionization mechanism: BPT diagnostic diagrams

Distinguish the different ionization mechanism in a galaxy is a very important and challenging topic in extragalactic astronomy. Baldwin et al. (1981), used a database of extragalactic objects to classify them according to their ionization mechanism. The predominant ionization mechanism in an extragalactic object could be: i) photo-ionization by O and B stars, ii) a power-law continuum source, and iii) shock wave heating (Baldwin et al. 1981).

Baldwin et al. (1981) classified the objects of their sample through different diagnostic diagrams based on emission line ratios (hereafter BPT diagrams), which search for differentiate the main sources of ionization. One of these diagrams uses $I([O_{III}]5007\text{Å})/I(H\beta)$ vs $I([N_{II}]6584\text{Å})/I(H\alpha)$. These ratios are very useful due to the small separation between the lines, thus avoiding the reddening correction.

The limits which divide the different ionization mechanisms is not fully clear. Kewley et al. (2001) studied the properties of starburst galaxies using the codes *PEGASE* and *STARBURST99*, which allowed them to derive an upper limit for the starburst region in the BPT diagrams. The limit between star-Forming objects and active galactic nuclei (AGN) in the BPT diagram is given by the following equation:

$$log\left(\frac{I([O_{III}5007\mathring{A}])}{I(H\beta)}\right) = \frac{0.61}{log(I([N_{II}]6584\mathring{A})/I(H\alpha)) - 0.47} + 1.19$$
 (4.40)

Kauffmann et al. (2003) studied a sample of 22623 AGNs at 0.02 < z < 0.30 taken from the *Sloan Digital Sky Survey* (SDSS) with the objective to separate star-forming galaxies and AGNs. Kauffmann et al. (2003) used the BPT diagrams and derived an empirical limit to the star-forming sequence. This limit lies below the line suggested by Kewley et al. (2001) (see figure 4.9), and the zone between both limits corresponds to the so-called composite galaxies, which probably host a mixture between the different ionization mechanisms (i.e. a normal star-forming galaxy with a nucleus that is activating, or with a significative contribution by shock heating). In Figure 4.9 is presented the BPT diagram made by Kauffmann et al. (2003). The gray line represent the upper limit between AGN and star-

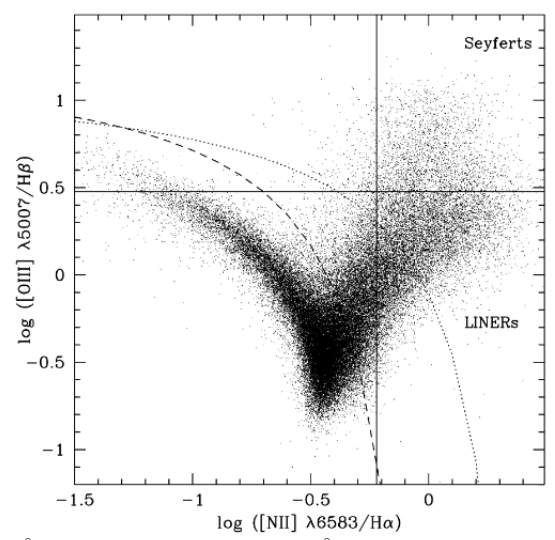


Figure 4.9: $I([O_{III}]5007\text{Å})/I(H\beta)$ vs $I([N_{II}]6584\text{Å})/I(H\alpha)$ BPT diagram, the black dots are galaxies taken from the SDSS at 0.02 < z < 0.3, the dotted line represent the limit derived by Kewley et al. (2001) and the segmented line represent the limit derived by Kauffmann et al. (2003), figure taken from Kauffmann et al. (2003)

forming regions (Kewley et al. 2001) and the black dashed line represents the lower limit (Kauffmann et al. 2003). Any object between these two limits lies in the composite zone which was explained above. Black dots represent galaxies taken from the SDSS.

Chapter 5

Results

5.1 Kinematics

5.1.1 Radial Velocity: The complex velocity field of HCG 31

In Figure 5.1 we display the radial velocity field of HCG 31, derived from the H α emission line. The contours represent H α emission in the flux levels of 6.3 $10^{-14}~ergs~s^{-1}$, $4.10^{-13}~ergs~s^{-1}$ and $1.0~10^{-11}~ergs~s^{-1}$. The velocity scale span a range from 3950 km s^{-1} to 4200 km s^{-1} . On this Figure, the main kinematical structures are labeled and the black lines represent the mock slits that we use to derive the position-velocity diagrams.

HCG 31 shows a complex kinematics, where we do not identify a single rotating pattern for the whole system (Amram et al. 2007 hereafter A07). We roughly identify three different kinematic entities: i) the Central Region (A+C), ii) a Western member called Galaxy B, and iii) the Southern tidal tail composed by three sub-regions (E1, E2), (H1, H2, H3) and (F1, F2, F3). These three entities are labeled with gray ellipses in Figure 5.1.

The group covers a very narrow range in velocity space ($\sim 200 \,\mathrm{km/s}$) which was also detected by other authors (Rubin et al. 1990, Richer et al. 2003, López-Sánchez et al. 2004, Amram et al. 2007). This indicate that the system has a very low velocity dispersion, which is expected for compact groups composed by late-type (or gas-rich) galaxies (Hickson et al. 1988b).

The central region shows a rotation pattern from East to West, with a PA \sim 120°. A07 derived different kinematic parameters for this region. They estimated

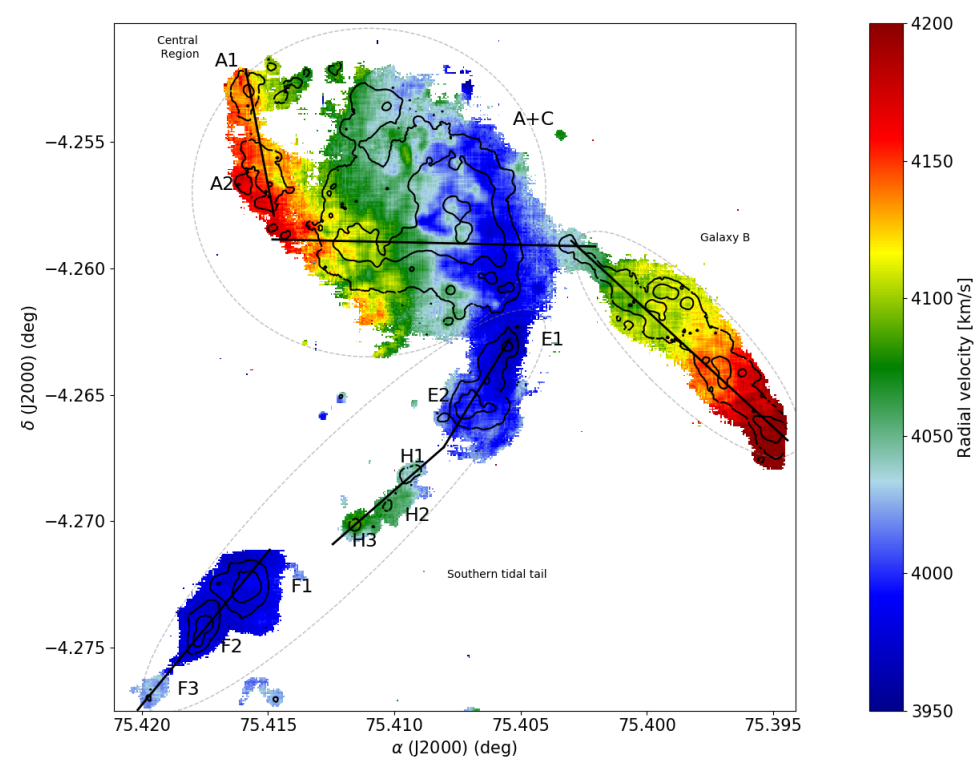


Figure 5.1: H α Radial velocity derived by IFSCUBE. The black contours represent H α emission. The gray ellipses show the three main kinematic entities visually identified (see text). The black lines represent the different simulated slits used to analyse the internal kinematic of each object. The radial velocity span range of 3950km/s < v < 4200km/s North is up and East on left.

a mass of the order of $4.5 \times 10^9 M_{\odot}$, PA = $130 \pm 3^{\circ}$, and an inclination of $52 \pm 5^{\circ}$. The difference between the lowest and highest velocity is in order of $\sim 150 \, \mathrm{km/s}$. To analyse the velocity gradient of galaxy A, we simulate the PA used by Verdes-Montenegro et al. (2005) in the analysis of the HI map of HCG 31 (Figure 5.1, horizontal line in region A+C). The velocity gradient, showed in Figure 5.2c, display similar values than the presented by previous authors.

It should be noted that the simulated slit passes through the zone where the ${\rm H}\alpha$ double components are seen on the high-resolution Fabry-Perot data of this system (A07). Thus, the velocity gradient showed in Figure 5.2c corresponds to the average motion of the multiple components (which cannot be resolved by MUSE). Richer et al. (2003) also showed Fabry-Perot data for HCG 31, with a resolution of ${\rm R}\sim7500$, concluding that A+C corresponds to a single kinematic entity.

There are also two sub-structures, A1 and A2, in the central region (see Fig-

ure 5.1). These sub-structures are part of the northern tidal tail of the group (Verdes-Montenegro et al. 2005). Probably, these sub-structures are made of material stripped from member A due to the interaction and now are falling back into the galaxy (Mendes de Oliveira et al. 2006, Amram et al. 2007). The simulated slit in these objects does not show a considerable velocity variation in A1 and a low amplitude in A2 ($\sim 40 \, \mathrm{km/s}$). The latter is counter-rotating concerning to A+C, which suggests that is currently falling back (A07). On the other hand, A1 does not show a considerable velocity gradient. Probably it is rotating tangentially, and its rounded shape may be evidence that. In any case the projected distance to the central merge ($\sim 9 \, \mathrm{kpc}$) is quite small and it does not have enough mass to gravitationally separate from the central merger ($\log (M/M_{\odot} \approx 6.6)$).

For Galaxy B, A07 derived the following kinematic parameters; PA = 45 \pm 3°, $i = 60 \pm 5$ ° and a rotation velocity of $\sim 120 \,\mathrm{km/s}$. Our velocity gradient (applying a inclination correction assuming $i = 60 \pm 5$ °) is consistent with the determinations of A07 and also with the HI map presented by Verdes-Montenegro et al. (2005).

The southern tidal tail is the more extended structure in our field-of-view, (~ 20 , kpc from E1 to F3). It is composed by three structures, from North to South: E, H, and F. In the HI map of this system (Williams et al. 1991, Verdes-Montenegro et al. 2005) this tail extends upon member G (not seen on our FoV), but its optical counterpart is formed by different small-scale structures, with the three main structures mentioned above. The velocity gradient is presented in Figure 5.2d, showing a somewhat peculiar kinematical behavior. No single velocity gradient is shown.

Galaxy E presents a steep velocity gradient with an amplitude of $\sim 70\,\mathrm{km/s}$. According to A07, this structure is falling back to A+C due its counter-rotation. Inside this member we can identify two main knots of star formation that we denominate E1 and E2, and are labeled in Figure 5.1. The difference in velocity between these two members is about $\sim 40\,\mathrm{km/s}$, but with a smooth velocity transition between them, suggesting that they are part of the same kinematic entity.

Object H consist in a chain of three star-forming knots aligned with the tail. This faint structure presents the higher velocity on the tail, with a peak of $4080 \,\mathrm{km/s}$ in H3 and an amplitude of $\sim 40 \,\mathrm{km/s}$ from H1 to H3. The northern part of the gradient seems to be connected with the southern part of member E

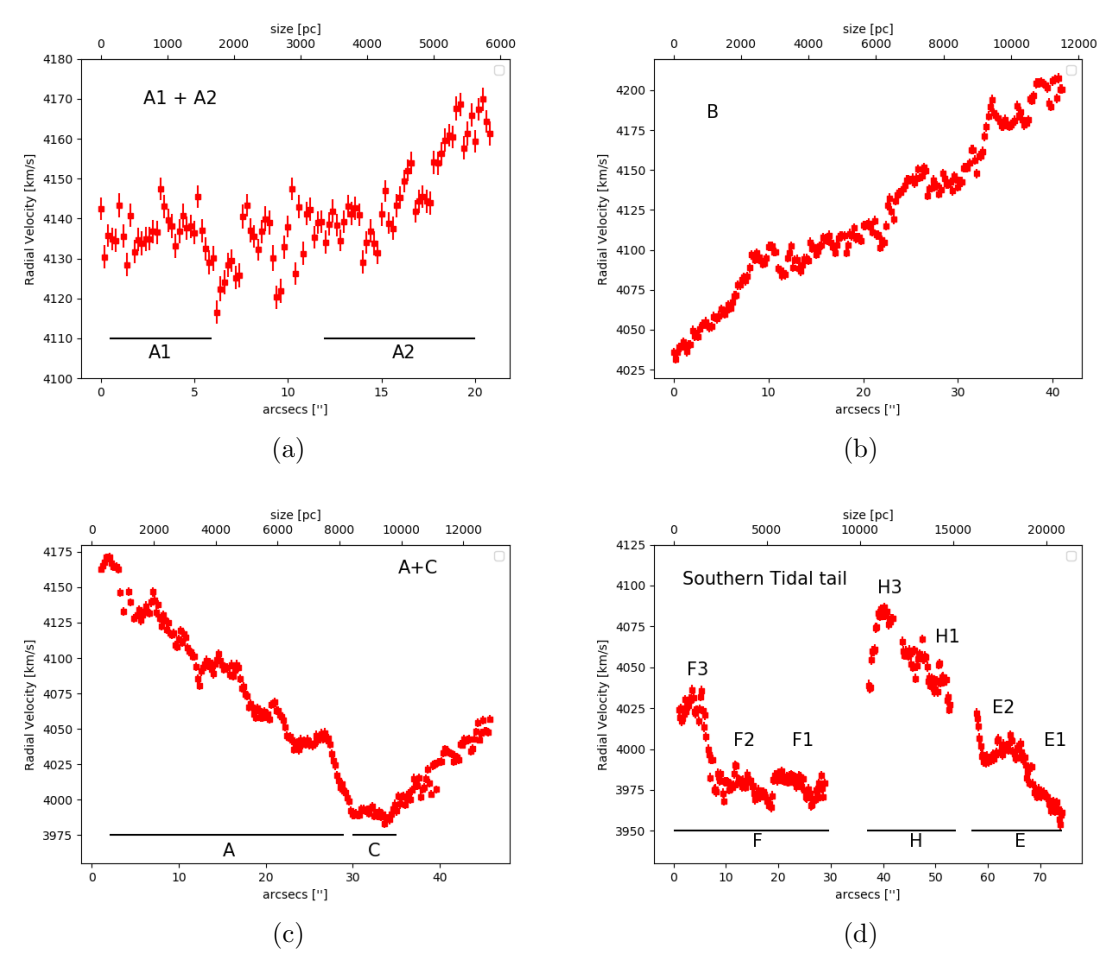


Figure 5.2: Velocity gradients derived for the different pseudo slits represented in Figure 5.1. The errorbars represents the uncertainty obtained from the fitting parameters of IFSCUBE as explained in section 4.5.1. The gradients run from East to West.

gradient. However, our H α map has a very low signal-to-noise in the gap between these objects and this connection cannot be strictly verified with our data. As for the southern part of the gradient, this object suffers a rapid velocity decrement in a very small projected distance, immediately before H3 center. The velocity is about $4080 \,\mathrm{km/s}$ at $40 \,\mathrm{arcsec}$ ($\sim 11.24 \,\mathrm{kpc}$) and $4040 \,\mathrm{km/s}$ at $37 \,\mathrm{arcsec}$ ($\sim 10.39 \,\mathrm{kpc}$), that is a $40 \,\mathrm{km/s}$ variation on $\sim 850 \,\mathrm{pc}$. This pronounced variation could be explained with the HI velocity map of this tidal tail (Verdes-Montenegro et al. 2005, figure 16) where it is seen that the center of H3 (e5 on Verdes-Montenegro et al. (2005)) lies in the edge of a region kinematically detached from the tail.

The object F is composed by three different knots: F1, F2, and F3. This object is the most plausible TDG candidate on HCG 31 (Iglesias-Paramo & Vilchez 1997,

Richer et al. 2003, López-Sánchez et al. 2004, Mendes de Oliveira et al. 2006, Amram et al. 2007, Verdes-Montenegro et al. 2005, Gallagher et al. 2010), along with member R (Mendes de Oliveira et al. 2006) (out of our FoV). Member F does not show a velocity gradient in our position-velocity diagram. Indeed, our velocity gradient seems flat, with no considerable variations on velocity, which is consistent with the previous velocity determinations on this object. It is possible to think that this kinematic behavior is due to rotation on the plane of the sky. However, this hypothesis was already refuted by A07, arguing that this case is very unlikely because the extended morphology of object F. The velocity of F1 and F2 is about $\sim 3980 \,\mathrm{km/s}$, which is consistent with the HI motions. This velocity is more similar to the velocity of E member. Considering the velocity of member H, the values obtained for member F could lead to misinterpretations concerning to the nature of the tail and shows the importance of studying 2D velocity fields, i.e., using long-slit data López-Sánchez et al. (2004) obtained a velocity gradient for the tidal tail, but they interpreted it as two different kinematic structures being on the same object: a short and warped optical tail that ends in H, and the HI tidal tail which connects A+C with G.

F3 shows a higher velocity of $\sim 4030\,\mathrm{km/s}$. A smooth gradient between the south of F2 and F3 is seen on our velocity gradient, suggesting that they are part of the same object. Comparing our velocity field with the HI velocity map of the tail we see that F1, F2, and F3 are part of the region kinematically detached from the tail that we mention above. This explanation favors the scenario on which F is a TDG in formation.

5.1.2 Velocity dispersion

 $H\alpha$ velocity dispersion (σ_v) map are presented in Figure 5.3. This map was derived by using the parameters derived from the single gaussian fitting performed by IFSCUBE and deconvolving instrumental and thermal dispersion from it (see section 4.1.2).

Objects A1, A2, B, E, H, and F shows low values of velocity dispersion ($\sigma_v < 30 \,\mathrm{km/s}$) (see Figure 5.3). These low values are consistent with previous determinations. However, high resolution data is required to understand in detail the internal kinematic of these sources, given the MUSE resolution is not very high ($50 \,\mathrm{km/s}$) (e.g to search for expanding shells using diagnostic diagrams).

Therefore, our determinations on these values are upper limits for these sources. Nonetheless, according to Moiseev et al. (2015), these velocity dispersion values (10 km/s < σ < 30 km/s) are quite typical for HII galaxies and giant HII regions.

The A+C complex is the most interesting zone in the velocity dispersion map. It hosts the highest values of σ in the system HCG 31, with a peak of ~ 95 km/s, and its distribution is not spatially correlated with $H\alpha$ contours. The two main H α knots in the central region present similar velocity dispersion values, of the order of ~ 50 km/s which is consistent with the determinations of Alfaro-Cuello et al. (2015).

It should be noted that the complex A+C shows double-peaked H α profiles (e.g. A07), which cannot be resolved with our resolution. A more detailed kinematics analysis, that consider the resolved physical properties of the system, is needed in order to understand the origin of these "high- σ_v " zones.

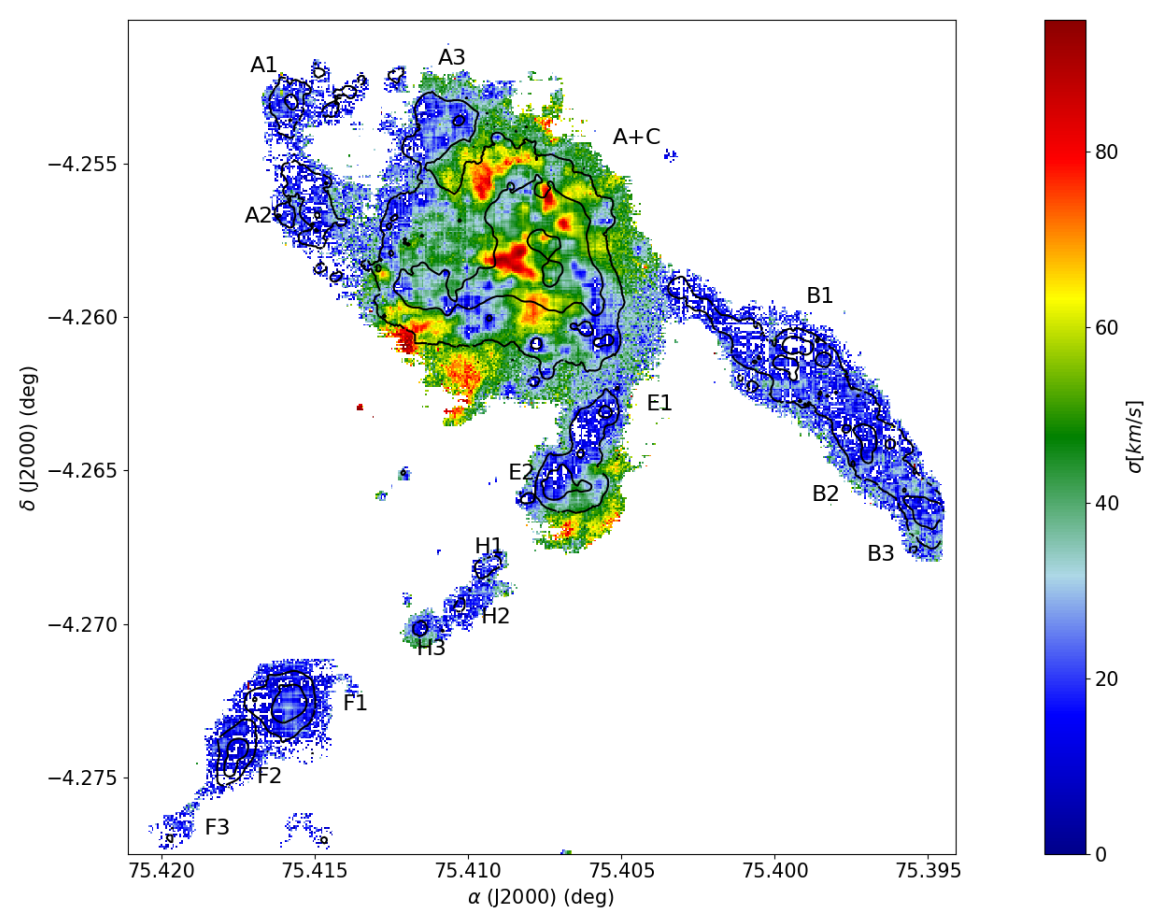


Figure 5.3: H α velocity dispersion map. The zones with higher σ are in the center of the merger between A and C. Members B, E and F present low velocity dispersion ($< 30~km~s^{-1}$). The group span a range of velocity dispersion of $10km/s < \sigma < 95km~s^{-1}$. However, our values probably are overestimated (see text).

5.2 Extinction: A 2D view of the dust distribution in HCG 31

As was explained in section 4.6, the extinction correction was performed using the Fitzpatrick law for galactic absorption, and Calzetti law for internal extinction. The E(B-V) map obtained is presented in Figure 5.4, where the contours represent $H\alpha$ in emission.

The values of E(B-V) ranges from 0 to ~ 0.4 . In some spaxels we detect negative values. These negative values indicates that the coefficient H α / H β is under the theoretical value of 2.86. However, this value implies specific conditions ($n_e = 100 \ cm^{-2}$, $T_e = 10^4 K$) which is not exactly the case for every zone in HCG

31 (e.g López-Sánchez et al. 2004). Thus, with different conditions, different values of the coefficient $H\alpha/H\beta$ are determined. On these cases we assume that the extinction is null. The higher E(B-V) values are in a $H\alpha$ knot that is part of member A. The mean values of E(B-V) for each member of HCG 31 are presented in Table 5.1. Our values are consistent, within the uncertainties, with previous determinations using spectroscopic data (e.g López-Sánchez et al. 2004) or from estimates performed with the HI density column (Williams et al. 1991).

Objects A1, A2, and A3 show very similar values of E(B-V), considering the uncertainties. Their extinction are equal. On those regions our values of the signal-to-noise ratio in H α and H β are relatively low (\sim 5-10), and many spaxels with negative extinction are found, limiting our number of spaxels with confident determinations of E(B-V). Therefore, on these regions we measure the extinction near to the most intense H α knot, maximizing the SNR and minimizing the uncertainties.

Objects A and A+C lies in the region with the highest SNR on our FoV, because of the overlapping of two MUSE fields (fields 1 and 2 on Figure 3.3). Thus, these objects present the lowest uncertainties in our E(B-V) determinations.

Particularly, object A hosts the knot with the highest extinction on HCG 31, with a value of E(B-V) $\sim 0.4 \pm 0.06$. In A+C the absorption is lower and is spatially correlated with the H α emission. In the south of A+C, there are several knots with high extinction (E(B-V) ~ 0.4) that are clearly distinguished in Figure 5.4.

In object B, the extinction of its three main knots seems similar, with B2 being the most extinguished. On this galaxy we use the same procedure as in A1, A2 and A3 to obtain the extinction, i.e. average the E(B-V) values for the points belonging to the peak in H α . It should be noted that this method only gave us an approximation of the extinction. But give us an idea of the average extinction in the galaxy. The bridge at the NE of this object shows a mean extinction value of E(B-V) $\sim 0.12 \pm 0.08$. The two main knots in object E shows similar values of E(B-V), being E2 the one with the highest extinction and also where the H α emission is strongest. For the main body of E, the extinction is E(B-V) $\sim 0-0.1$. In member H the emission of H α and H β is very weak and has low SNR. Thus, the uncertainties determining E(B-V) are very high on its three main knots. In object F the extinction seems to be slightly lower than in the rest of the knots in HCG 31. In F1 and F2 there is a clear spatial correlation between H α emission

Object	$E(B-V^1)$ [dex]
A1	0.19 ± 0.12
A2	0.20 ± 0.16
A3	0.18 ± 0.17
A	0.16 ± 0.08
A+C	0.12 ± 0.02
B1	0.16 ± 0.09
B2	0.17 ± 0.10
В3	0.12 ± 0.04
E1	0.18 ± 0.07
E2	0.20 ± 0.12
H1	0.21 ± 0.25
H2	0.20 ± 0.36
Н3	0.25 ± 0.25
F1	0.10 ± 0.04
F2	0.07 ± 0.06

Table 5.1: Average $\overline{\text{E(B-V)}}$ values obtained for each member of HCG 31

and the extinction. However, F2 knot is less extinguished than F1.

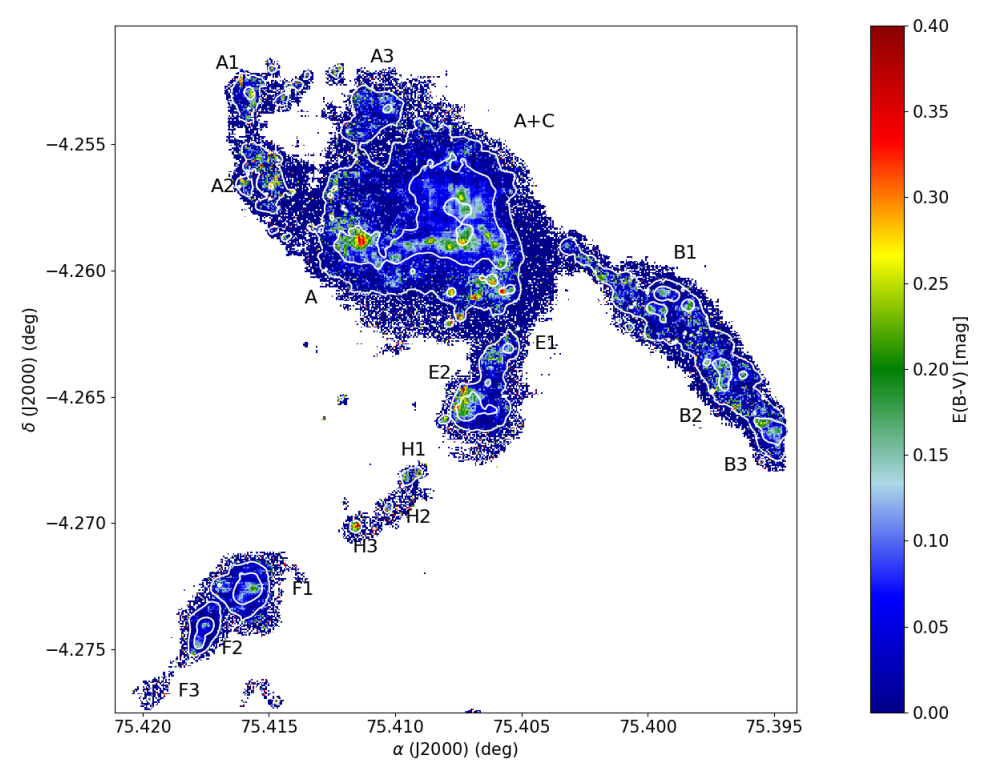


Figure 5.4: E(B-V) map of HCG 31. White contours represents $H\alpha$ in emission. The group shows low values of E(B-V) excepting in the central zone. Where the E(B-V) shows a peak in a knot of galaxy HCG 31 A.

5.3 Physical parameters

5.3.1 Electron Temperatures

The electron temperatures obtained for [SIII], [SII], [OIII], [OIII], and the electron density n_e obtained for the labeled knots are presented in table 5.2.

The temperature shows a different behavior in the central zone in comparison with the outer knots. In A+C, the $T_e([SIII])$ have an average of $\sim 0.77(\pm 0.04) \times 10^4$ K, and span a range of $0.71 \times 10^4 K < T_e([SIII]) < 1.11 \times 10^4 K$, while other knots shows temperatures higher than 10^4 K but lower than 1.3×10^4 K. It should be noted that the uncertainties are smaller in the central zone by approximately one order of magnitude, which is a consequence of the higher signal-to-noise ratio at this zone.

The temperatures of the central knots are similar considering the uncertainties. Their $T_e([OIII])$ are very close to 10^4 K which is the standard value used for HII regions. We find no considerable temperature variations on the central zone. On

Object (1)	$T_e([SIII])[10^4 \text{ K}] (2)$	$T_e([SII])[10^4 \text{ K}] (3)$	$T_e([OIII])[10^4 \text{ K}] (4)$	$T_e([OII])[10^4 \text{ K}] (5)$	$n_e \ [cm^{-3}] \ (6)$
Knot A	0.76 ± 0.03	0.87 ± 0.05	0.91 ± 0.11	1.05 ± 0.07	170 ± 30
Knot C	0.80 ± 0.05	0.88 ± 0.05	0.94 ± 0.11	1.08 ± 0.07	100 ± 70
A+C	0.77 ± 0.04	0.87 ± 0.05	0.91 ± 0.11	1.06 ± 0.07	< 100
B1	1.06 ± 0.12	0.97 ± 0.06	1.16 ± 0.15	1.20 ± 0.08	< 100
B3	1.03 ± 0.10	0.96 ± 0.06	1.14 ± 0.14	1.19 ± 0.08	< 100
F1	1.15 ± 0.13	1.00 ± 0.06	1.24 ± 0.16	1.24 ± 0.08	< 100
F2	1.15 ± 0.15	1.00 ± 0.06	1.24 ± 0.17	1.24 ± 0.09	< 100

Table 5.2: Physical parameters of the different knots in HCG 31. Col (1) Shows their IDs. Col (2) show the [SIII]temperature which is the only measured using the direct method. Cols (3), (4) and (5) shows the temperatures of [SII], [SII], [OIII] and [OII] respectively. Col (5) shows the electron density obtained with the Sulfur doublet $[SII]\lambda\lambda$ 6717 6731.

the north of knot C, a small region with a higher temperature is observed, with an average $T_e([SIII]) \sim 1 \times 10^4 K$. However, the angular size of this region is smaller than the seeing, thus we cannot consider it as an independent region. Furthermore there is no considerable $H\alpha$ emission near to it.

In galaxy B we can measure $T_e([SIII])$ for two regions, B1 and B3. We have information only of the central knot of B1 (assuming that B1 is composed by three different close knots). The $T_e([SIII])$ for regions knots are very similar $(1.06 \times 10^4 K \text{ for B1 and } 1.03 \times 10^4 K \text{ for B3})$.

Member F presents the highest values of $T_e([SIII])$ throughout HCG 31. F1 and F2 show the same temperature which makes sense, because they are part of the same object (the TDG candidate).

López-Sánchez et al. (2004) also presents $T_e([OIII])$ determinations for different knots in HCG 31. Our values are in good agreement with their determinations.

5.3.2 Electron Density

In Figure 5.6 we show the electron density map, derived from the equations presented in section 4.2. The black contours represent H α emission. The sulfur doublet [SII] $\lambda\lambda$ 6717, 6731 was not detected with enough SNR in the whole system, then there is no complete information in all the spaxels showed in the figure. The average values at the different knots are presented in column (6) of table 5.2.

In general, electron densities in HCG 31 are in the low-density regime ($n_e < 100 \ cm^{-3}$), with a peak in the knots located in members A and C. The knot in member A has an average electron density of $n_e \sim 170 \pm 30 cm^{-3}$ with a peak of $\sim 300 cm^{-3}$, and the knot in C has an average electron density of $100 \pm 70 cm^{-3}$ with a peak of $\sim 140 cm^{-3}$. In all the other members, the electron density remains below $100 \ cm^{-3}$. These measures are consistent with the values known for extragalactic

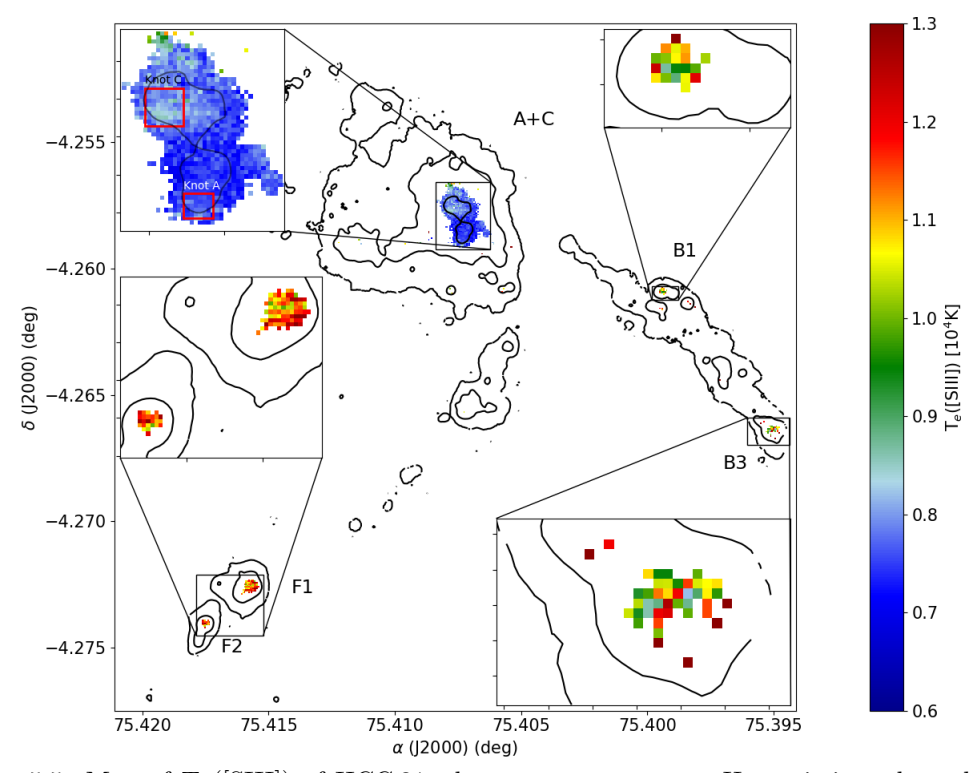


Figure 5.5: Map of $T_e([SIII])$ of HCG 31, the contours represent $H\alpha$ emission, the red boxes marks the positions of the 2 main $H\alpha$ knots in the central zone of this system. The central zone of the system shows the lower values of temperature with $T_e([SIII]) \sim 0.7[10^4 K]$. While the knots located at members F and B shows higher values of temperature

HII regions ($n_e < 500 \ cm^{-3}$ Bresolin et al. 2005).

Krabbe et al. (2014) studied seven pairs of interacting galaxies finding that these systems shows higher electron densities ($n_e = 24\text{-}532~cm^{-3}$) than isolated galaxies ($n_e = 40 - 137~cm^{-3}$). Our values are consistent with those ranges.

Previous determinations of electron density on HCG 31 has been performed by López-Sánchez et al. (2004) and Alfaro-Cuello et al. (2015) (only the central zone for this latter study).

We obtain very similar values than those reported by López-Sánchez et al. (2004), i.e. $n_e < 100 \ cm^{-3}$ for almost the entire system except the central zone. In particular for member C these authors obtained $n_e = 210 \pm 70$, which is higher than our value. This disagreement can be explained considering the aperture effects, because our definition of knot C is not the same than for member C in their work.

Alfaro-Cuello et al. (2015) found $n_e = 230 \pm 120 \ cm^{-3}$ for knot A and n_e

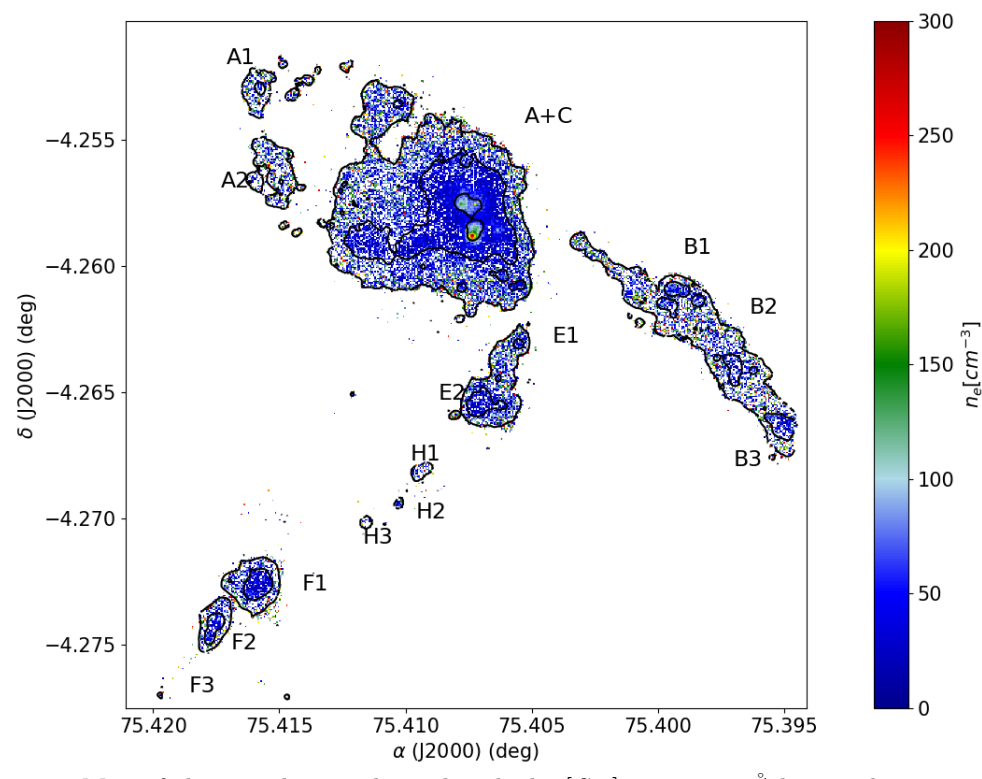


Figure 5.6: Map of electron density derived with the $[S_{II}]$ 6717,6731 Å lines. The contours are $H\alpha$ in emission. Almost the whole group shows low densities with $n_e < 100[cm^{-3}]$. In central knots of the A+C it is seen a peak in the density with a knot showing $n_e \sim 250[cm^{-3}]$.

= $80 \pm 50 cm^{-3}$ for knot C. These values are consistent with our estimates, within the uncertainties. It should be noted that the aperture effects are not important because the authors also used IFU data on the central zone of HCG 31, and our definitions of knots A and C are very similar.

5.4 Chemical Abundances in HCG 31

In these section we present our results obtained for the different chemical abundances in the system HCG 31. In the text we assume the metallicity as a proxy of the oxygen abundance.

5.4.1 Empirical relations and Direct Method

We derive the chemical abundances of oxygen, nitrogen, sulfur, argon and helium. Only the abundance of sulfur and helium were determined using the

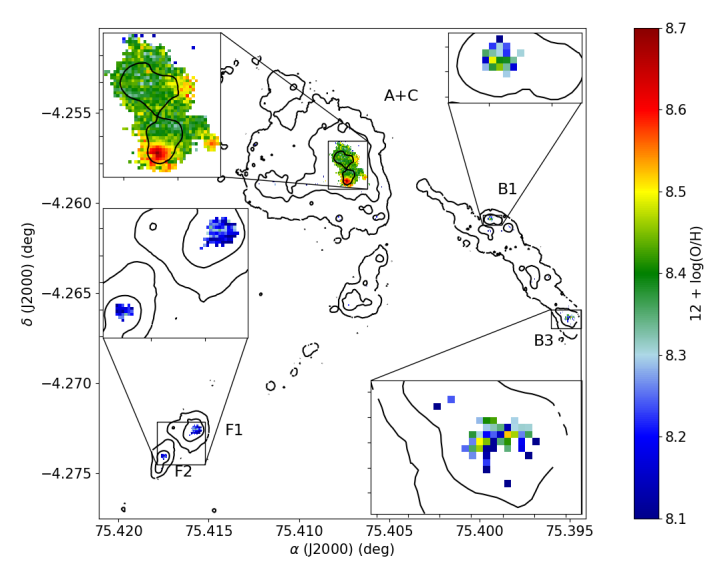


Figure 5.7: Oxygen abundance map obtained using empirical calibrators for $T_e([OIII])$. The overplotted contours correspond to $H\alpha$ emission. A knot located in the southern part of the central zone shows the peak of oxygen abundance in the whole system with $12 + log(O/H) \sim 8.6$ dex

direct method. For the other elements we use the empirical relation between the temperatures (hereafter Empirical relation method ERM).

In the central zone of the group we measure the following average oxygen abundances for the different knots: $12 + log(O/H) = 8.40 \pm 0.18$ for knot C, $12 + log(O/H) = 8.57 \pm 0.18$ for knot A and an average of $12 + log(O/H) = 8.43 \pm 0.19$ for the central zone. On knots B1, B3, F1, and F2 we see similar values of 12 + log(O/H) with 8.00 < 12 + log(O/H) < 8.30. The map of the oxygen abundance is presented on Figure 5.7. The oxygen abundance was derived using ERM. The mean chemical and ionic abundances of the different knots are presented on table 5.3. On the table we present the average values of the abundances of O^+ , O^{2+} , O, N^+ , N, N/O, S^+ , S^{2+} , S, Ar^{2+} , Ar, He^+_{5876} , He^+_{6678} , He^+_{7065} and $He^+_{adopted}$. We also include the values of the ICFs for N^+ , $S^+ + S^{2+}$ and $Ar^{2+} + Ar^{3+}$. All the abundances were obtained using the equations described in section 4.9. A remarkable result is that all the knots in the group shows similar abundance values within the uncertainties.

The abundance maps for Ar, He^+ , N and S are presented on Figure s, 5.8, 5.9, 5.10, and 5.11, respectively. The argon abundance shows a similar behaviour compared to oxygen, with higher values on the central zone of $12 + \log(Ar/H) \sim 6.23$, compared to B and F knots, with averages values of $12 + \log(Ar/H) \sim$

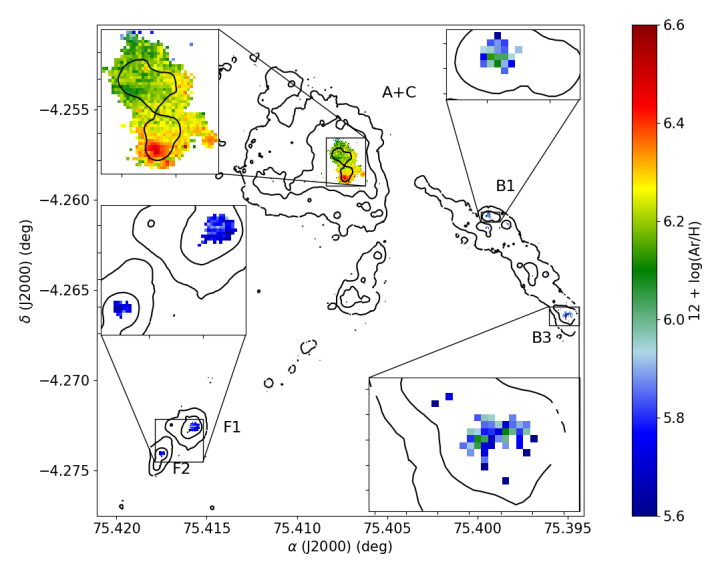


Figure 5.8: Map of the argon abundance obtained with the equations described in 4.9

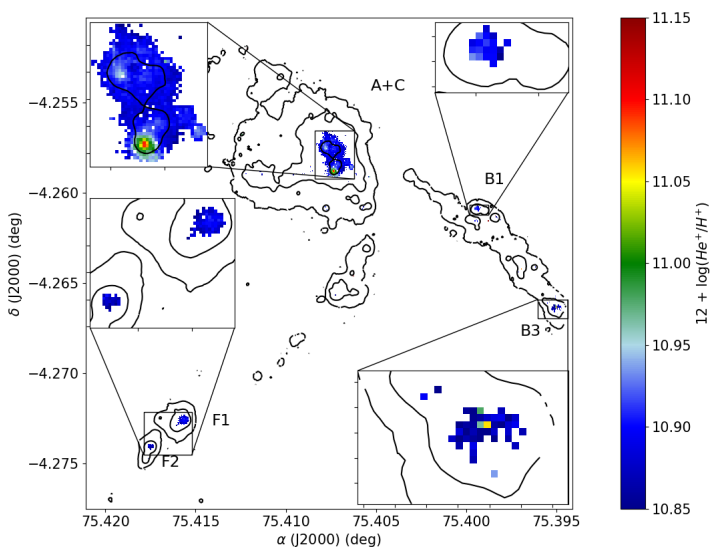


Figure 5.9: Helium abundance obtained with the method described in section 4.9

5.78 and $12 + \log(Ar/H) \sim 5.74$ respectively, and an abundance peak in knot A of $12 + \log(Ar/H) = 6.38 \pm 0.05$. He^+ shows a quite homogeneous abundance map with values of $10.87 < 12 + \log(He^+/H^+) < 10.91$ through the whole system, excepting a peak of $12 + \log(He^+/H^+) = 11.00 \pm 0.02$ in knot A.

The nitrogen abundance map shows a behavior similar to oxygen and argon, with the central zone being more metallic ($12 + \log(N/H) = 7.01 \pm 0.09$) compared to the knots in B and F ($12 + \log(N/H) = 6.48 \pm 0.09$ on average), and

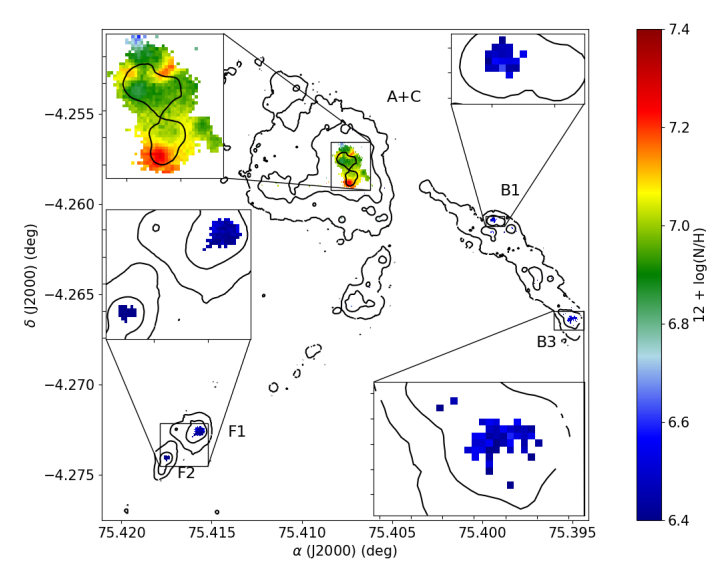


Figure 5.10: Nitrogen abundance obtained with the method described in section 4.9

it shows a peak on knot A with $12 + \log(N/H) = 7.20 \pm 0.08$. In addition, there are two more peaks with an elongated shape at the NE and NW of knot C with values $12 + \log(N/H) \sim 7.1$. These knots only appear on this abundance map, suggesting the presence of massive nitrogen Wolf-Rayet stars that are enriching their nearby environment with nitrogen. The most particular abundance map is that of sulfur, which shows a quite different behavior compared to the other metals.

Despite the main trend of a more metallic center remains, with a value of $12 + \log(S/H) = 6.70 \pm 0.08$, and an average of $12 + \log(S/H) = 6.32 \pm 0.10$ and $12 + \log(S/H) = 6.21 \pm 0.11$ for B and F respectively. The central zone display the peculiarity. A peak in abundance is found outside any specific knot which is a different behaviour compared to the other metals. We cannot attribute this peculiar behavior to a bad line-fitting, because the SNR of the lines used to derive this abundance shows a peak at the central zone.

Comparison with literature

López-Sánchez et al. (2004) derived chemical abundances for different knots in HCG 31 using the direct method, finding $12 + log(O/H) = 8.22 \pm 0.05$ for knot C. Our measurement is consistent with that determination, within the uncertainties. This consistency is fullfilled comparing to other knots. However, if we compare the abundances for each ion we find a disagreement on the O^+ ionic abundance.

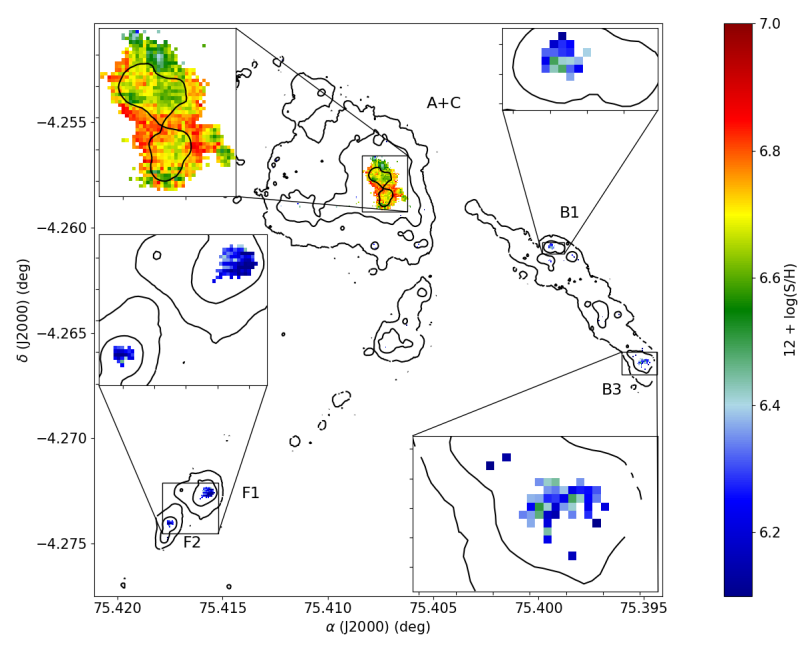


Figure 5.11: Sulfur abundance obtained with the method described in section 4.9

Our estimation is ~ 0.2 dex higher than the estimations given in López-Sánchez et al. (2004). One can think on aperture effects, but this is unlikely because in our spatially resolved map we did not find any spaxel with values of O^+ similar to those found on López-Sánchez et al. (2004). Probably, the origin of this difference arises from the use of different equations and emission-line fluxes to derive this abundance. Nonetheless, according to Kniazev et al. (2004), the oxygen abundance using $[O_{II}]7319,7330\text{Å}$ should be consistent with the direct method using the $[O_{II}]3727\text{Å}$ and [OIII]4363Å lines. Another possibility is that the difference lies on the fact that $T_e([OIII])$ was calculated through an empirical relation, but our determinations of $T_e([OIII])$ were consistent with previous determinations using the direct method.

In order to revise this inconsistency, we take the emission-line fluxes published by López-Sánchez et al. (2004) of the knot C, and use them to derive the O^+ abundance, by using the equations described on Pérez-Montero (2014). We obtained $12 + \log(O^+/H^+) = 8.03 \pm 0.12$ which is greater than the published value in López-Sánchez et al. (2004) ($12 + \log(O^+/H^+) = 7.82 \pm 0.07$). However, our estimate, based on the fluxes published in López-Sánchez et al. (2004), is fully consistent with our determinations at the knot C, by using the MUSE data. Therefore, the difference on the O^+ abundance could be associated to the use of

a different set of equations.

5.4.2 Empirical calibrators results and HII-CHI-Mistry

In order to have a larger view of the the oxygen abundances in HCG 31, we derive this abundance using the following strong-line empirical calibrators: N2, O3N2, S23, and S3O3. The abundance maps obtained with these calibrators are presented on Figures 5.12 and 5.13. In addition, we use also the code HII-CHII-Mistry (Pérez-Montero 2014), whose results are shown in Figure 5.12c.

In the case of the N2 and O3N2 parameters, we used the calibrations proposed by Marino et al. (2013), as explained in section 3.4.6. The maps obtained with these parameters are presented on Figures 5.12a and 5.12b, for N2 and O3N2 respectively. In Figure 5.12a it is also represented the slits used to obtain the metallicity gradients of the system (detailed in next section). In the case of the S3O3 parameter, we use the calibration provided by Stasińska (2006), and the derived map is presented on Figure 5.13a. In the case of S23, we use the calibration of Pérez-Montero & Díaz (2005) and its map is presented on Figure 5.13b.

Inspecting Figures 5.12a and 5.12b, specially in the central region of HCG 31, we observe a very similar trend with respect to the oxygen map shown in Figure 5.7 (previous section). On Figures 5.12a and 5.12b we detect a more metallic knot at the south (knot A).

In the case Figure 5.12a we observe a slight transition from $12 + log(O/H) = 8.23 \pm 0.16$ (N2) in HCG 31C to $12 + log(O/H) = 8.40 \pm 0.16$ (N2) at HCG 31A. On the other hand, the S23 and S3O3 calibrators provide similar values for knots A and C: $12 + log(O/H) = 8.05 \pm 0.20$ (S23) $12 + log(O/H) = 8.03 \pm 0.20$ (S23), respectively. However, considering the uncertainties, the previous measurements are very consistent within each other, suggesting a quite homogeneous metallicity distribution at the center of the A+C complex, with a slightly more metallic peak in HCG 31 A.

Using GMOS-IFU data, Torres-Flores et al. (2015) studied the central zone of HCG 31, finding a metallicity gradient in the line that connects the main burst of star formation in HCG 31 A and C. Our maps suggest the same behaviour of the oxygen abundance, especially those obtained with N2 and O3N2. In the case of the S23 and S3O3, something different is observed. We observe a drop in metallicity in knot A, based on the parameter S3O3. In the case of parameter S23, all the

Abundance	Knot A	Knot C	A+C	B1	B3	F1	F2
$12 + \log(O^+/H^+)$	8.35 ± 0.18	8.06 ± 0.18	8.16 ± 0.18	7.99 ± 0.17	8.03 ± 0.17	7.75 ± 0.17	7.83 ± 0.18
$12 + \log(O^{2+}/H+)$	+	8.14 ± 0.19	8.09 ± 0.19	8.01 ± 0.17	7.96 ± 0.17	8.00 ± 0.17	7.95 ± 0.17
$12 + \log(O/H)$	8.57 ± 0.18	8.40 ± 0.18	8.43 ± 0.19	8.30 ± 0.17	+	8.20 ± 0.16	8.19 ± 0.17
$12 + \log(N^+/H^+)$	6.97 ± 0.07	6.58 ± 0.07	6.74 ± 0.08	4	6.22 ± 0.07	5.98 ± 0.06	5.92 ± 0.07
$ICF(N^+)$	1.69 ± 0.06	2.28 ± 0.18	1.91 ± 0.12	44	1.87 ± 0.14	2.88 ± 0.38	2.34 ± 0.28
$12 + \log(N/H)$	7.20 ± 0.08	6.94 ± 0.09	7.01 ± 0.09	6.49 ± 0.09	6.49 ± 0.08	6.44 ± 0.10	6.28 ± 0.10
$\log(N/O)$	-1.37 ± 0.20	-1.46 ± 0.21	-1.42 ± 0.21	-1.81 ± 0.19	-1.81 ± 0.18	-1.76 ± 0.19	-1.91 ± 0.19
$12 + \log(S^+/H^+)$	5.98 ± 0.07	5.81 ± 0.07	5.97 ± 0.07	5.69 ± 0.06	5.82 ± 0.06	5.57 ± 0.06	5.56 ± 0.07
$12 + \log(S^{2+}/H^{+})$	6.57 ± 0.08	6.59 ± 0.10	6.59 ± 0.09	6.19 ± 0.13	6.14 ± 0.12	6.05 ± 0.13	6.10 ± 0.14
$ICF(S^+ + S^{2+})$	1.02 ± 0.00	1.05 ± 0.00	1.03 ± 0.00	1.04 ± 0.00	1.02 ± 0.00	1.08 ± 0.01	1.05 ± 0.00
$12 + \log(S/H)$	6.68 ± 0.07	6.68 ± 0.09	6.70 ± 0.08	6.32 ± 0.11	6.32 ± 0.10	6.20 ± 0.11	6.23 ± 0.12
$12 + \log(Ar^{2+}/H^{+})$	6.27 ± 0.05	6.08 ± 0.08	6.12 ± 0.07	5.81 ± 0.11	5.76 ± 0.10	5.69 ± 0.12	5.65 ± 0.13
$ICF(Ar^{2+} + Ar^{3+})$	1.29 ± 0.01	1.20 ± 0.01	1.27 ± 0.02	$+\!\!\!+\!\!\!\!+$	1.27 ± 0.03	1.17 ± 0.02	1.20 ± 0.03
$12 + \log(Ar/H)$	6.38 ± 0.05	6.16 ± 0.08	6.23 ± 0.06	5.90 ± 0.11	5.87 ± 0.10	5.75 ± 0.11	5.73 ± 0.13
$12 + \log(He^+/H)_{5876}$	10.97 ± 0.01	10.94 ± 0.01	10.94 ± 0.01	10.93 ± 0.03	10.91 ± 0.03	10.94 ± 0.02	10.91 ± 0.02
$12 + \log(He^+/H)_{6678}$	10.97 ± 0.01	10.93 ± 0.01	10.92 ± 0.02	10.89 ± 0.04	10.90 ± 0.04	10.92 ± 0.03	10.91 ± 0.03
$12 + \log(He^+/H)_{7065}$	11.04 ± 0.06	10.86 ± 0.06	10.84 ± 0.07	10.87 ± 0.09	10.77 ± 0.10	10.78 ± 0.08	10.79 ± 0.09
$12 + \log(He^+/H)_{adopted}$	11.00 ± 0.02	10.91 ± 0.02	10.90 ± 0.02	10.90 ± 0.03	10.87 ± 0.03	10.88 ± 0.02	10.87 ± 0.03

Table 5.3: Chemical abundances of the different knots in HCG 31. All the Chemical abundances have been measured using the equations explained in section 4.9.

central zone display low values of metalicity, with a mean of $12 + log(O/H) = 8.14 \pm 0.20$. Nevertheless, as explained before, all the abundance maps obtained with the empirical calibrators are consistent within each other if we consider the uncertainties.

Objects A1, A2, and A3 presents very similar values of 12 + log(O/H) spanning a range of 8.3 < 12 + log(O/H) < 8.4 (N2 and O3N2). Considering the uncertainties, it can be considered that these 3 objects have the same metallicity, having a similar value than HCG 31A (we note that this trend is observed for all the calibrators). This finding is consistent with the tidal origin of these sources, proposed by several authors (Amram et al. 2007, López-Sánchez et al. 2004)

Galaxy B shows a fairly homogeneous distribution of metallicity at the surroundings of the knot B2 with $12 + log(O/H) \sim 8.3$ (N2 and O3N2) and a drop to lower metallicities at B1 and B3 with $12 + log(O/H) \sim 8.1$ (N2 and O3N2). The bridge that connects B and A+C seems to have the same metallicity as the main body of B. Using the tracer S3O3 we observe low metallicities through the galaxy, with values ranging between $8.0 \pm 0.25 < 12 + log(O/H) < 8.10 \pm 0.25$. Using the tracer S23, we determine that knots B1 and B3 present similar values, with $12 + log(O/H) \sim 8.0 \ 12 + log(O/H) 8.31 \pm 0.20$, respectively.

The mean values of the oxygen abundance for sources E and H are 12 + log(O/H) 8.25 ± 0.16 and 12 + log(O/H) 8.20 ± 0.18 , for the N2 and O3N2 calibrators, respectively. These values are similar to the abundances of the central complex A+C, suggesting a tidal origin for sources E and H, in a similar way than objects A1, A2, and A3. Object H does not provided information to use calibrators S3O3 and S23. In the case of source E, we found $12 + log(O/H) = 8.15 \pm 0.25$ and $12 + log(O/H) = 8.22 \pm 0.20$, for S3O3 and S23, respectively.

The member F is the most metal-poor, where F1 and F2 present the same metallicity for all the calibrators. The mean value of metallicity for object F is $12 + log(O/H) \sim 8.06$, for N2 and O3N2, and $12 + log(O/H) \sim 7.88$, for S3O3 and S23.

We also derive the metallicity using the code HII-CHI-Mistry, whose result is shown in Figure 5.12c. Inspecting Figure 5.12c, it is quite noticeable that the highest metallicities are detected for the main body of galaxy A and for the region between the knots of galaxy B, with values of $12 + log(O/H) \sim 8.55$. This value is considerably higher than the values of these regions obtained with N2 and O3N2 calibrators, where the metallicities span a range of 8.2 < 12 + log(O/H) < 8.4.

This difference could be due to dependences with the ionization parameter or some relative abundances such as the nitrogen-to-oxygen ratio.

On Figure 5.14 we plot all metallicities derived on this section, where we have included the values estimated by López-Sánchez et al. (2004) (L04 in Figure 5.14), by using the direct method. Inspecting the figure we derive three conclusions: i) there is a very good agreement between the empirical calibrators, ii) The Empirical relation method shows higher values than any other method, and iii) HII-CHI-Mistry shows a particular behavior, which is consistent with the values derived from ERM and L04 for knots F and B, but not for knots A and C.

5.4.3 Metallicity gradients on HCG 31

We propose to study the metal distribution in three main structures of HCG 31: i) Galaxy B, ii) southern tidal tail, and iii) the A+C complex. In order to carry out this analysis, we simulate 3 different slits that passes through the structures mentioned above. The positions of the slits are shown on Figure 5.12a. In the southern tidal tail we use the same slit as defined in section 5.1.1. In galaxy B we split the slit in two parts to cover the connection between the knots B1, B2 and B3, and also include the bridge between B and A+C. The slits used have a width of 1" and we binned the gradients in 1" to match the seeing (the seeing at the observation was ~ 1 arcsecond).

The metallicity gradients derived for the different slits are presented on Figure 5.15. The data was fitted using the package curve_fit of scipy which allow us to consider the uncertainties to perform the linear regression. The parameters obtained for the fits are listed in table 5.4. We have not considered the calibrators S23 and S3O3 because the lack of spaxels with good signal. Error bars in Figure 5.15 represents the propagated error coming from the flux uncertainties. On the top right region of Figure 5.15 we show the dispersion associated with each calibrator (0.16 dex for N2 - red bar, and 0.18 dex for O3N2 - blue bar). We also plot the abundance gradient based on the direct method estimates. In this case we combine our estimations with the data published by López-Sánchez et al. (2004), where we take the abundance of knot B (used for the center of galaxy B) and the abundance of object E, which was used on the gradient of the southern tidal tail.

Inspecting the gradient of galaxy B, we find in the main body of the galaxy

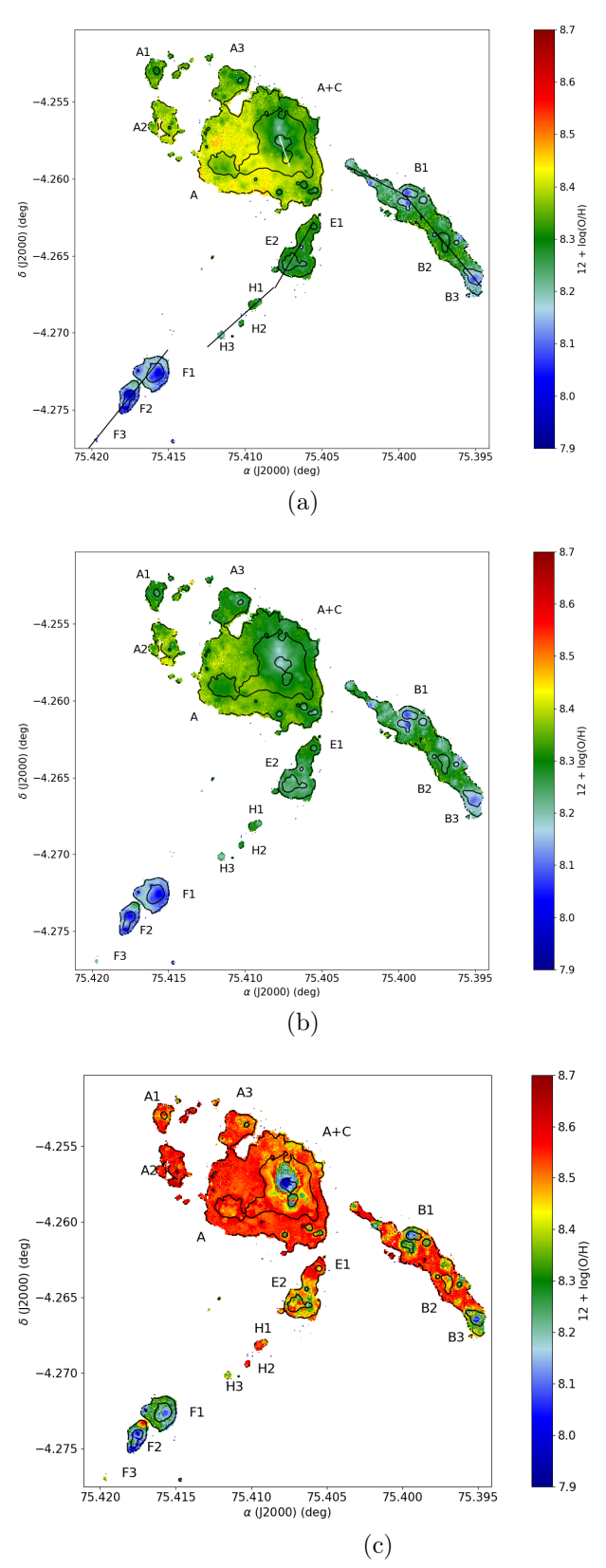


Figure 5.12: Oxygen abundance maps calculated with different strong lines calibrations and HII-CHI-Mistry; (a) N2 (Marino et al. 2013), (b) O3N2 (Marino et al. 2013) and (c) HII-CHI-Mistry (Pérez-Montero et al 2014) in all the maps the contours represent $H\alpha$ emission.

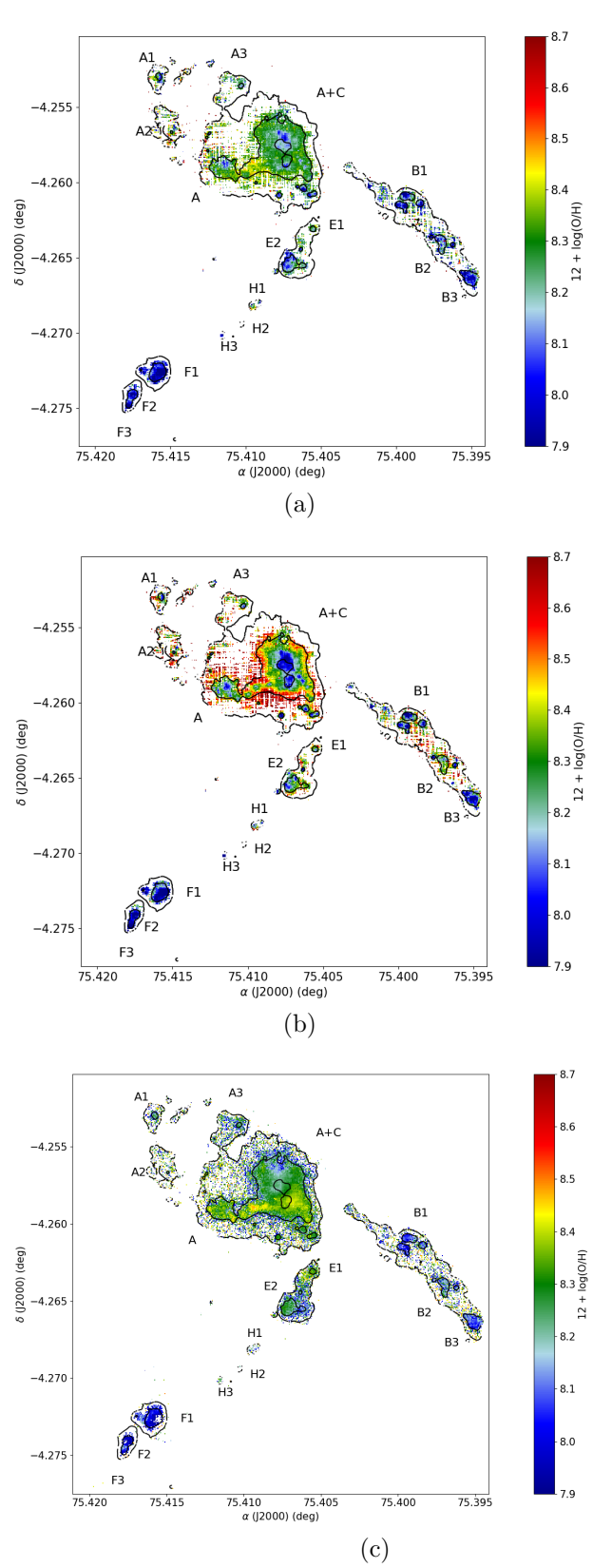


Figure 5.13: Oxygen abundance maps calculated using strong lines empirical calibrators; (a) S3O3, (b) S23 and (c) AR3O3

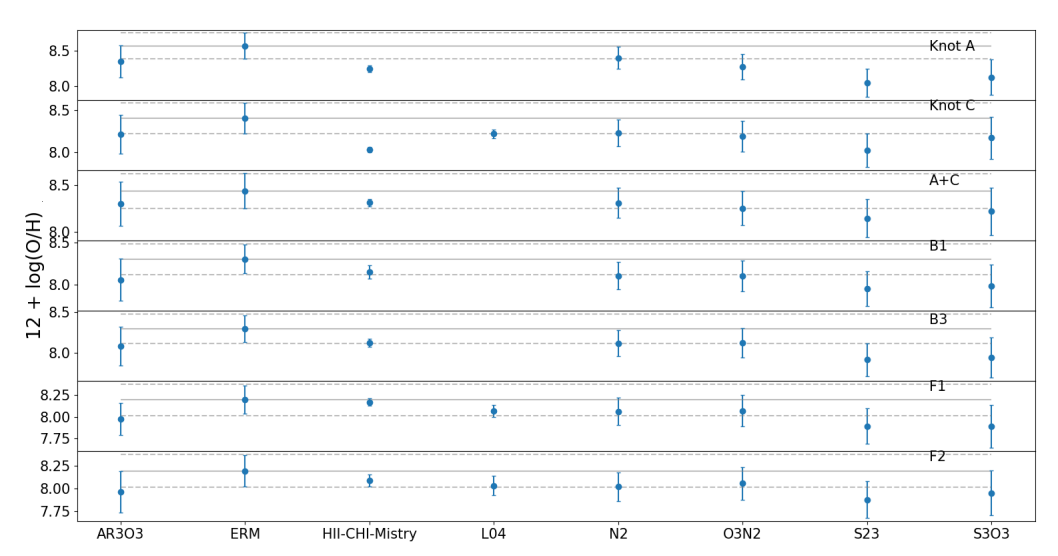


Figure 5.14: Comparison of the metalicities obtained with the different strong-line empirical calibrators, ERM, HII-CHI-Mistry and the values obtained by López-Sánchez et al. (2004) (L04). Every panel represent a different knot in HCG 31. The horizontal segmented lines represents the oxygen abundance obtained with ERM.

a somewhat steep gradient, with a peak non correlated with the center of the galaxy around 5 arcsecs (~ 1.4 kpc) displaced, this behaviour is also observed with HII-CHI-Mistry.

For the bridge of galaxy B, which starts at around 17 arcsecs on Figure 5.15a, a quite flat metallicity gradient is observed (by using HII-CHI-Mistry, N2 and O3N2calibrators). We do not have information of the metallicity on the bridge through the ERM.

We perform a linear fit on the metallicity distribution of member B, considering the measurements on its main body and bridge and whose results are listed on Table 5.4. We find a gradient of $\alpha = -0.012 \pm 0.002 [dex/kpc]$, with the N2 method, suggesting a flat oxygen distribution which is expected for a galaxy with interaction signatures (Kewley et al. 2010, Rich et al. 2012).

We compare this metal distribution with results obtained for galaxies NGC 4656 and NGC 55, which display similar morphological types (SB(s)m, taken from NED) and whose gradients were studied by Muñoz-Elgueta et al. (2018) and Magrini et al. (2017) respectively (see Figure 5.15a). We find similar slopes between these systems, suggesting flat metal distributions. The metallicities in NGC 5656 and NGC 55 are lower than HCG 31 B by 0.1-0.2 dex.

The drop on the central metallicities observed on HCG 31 B is a really interest-

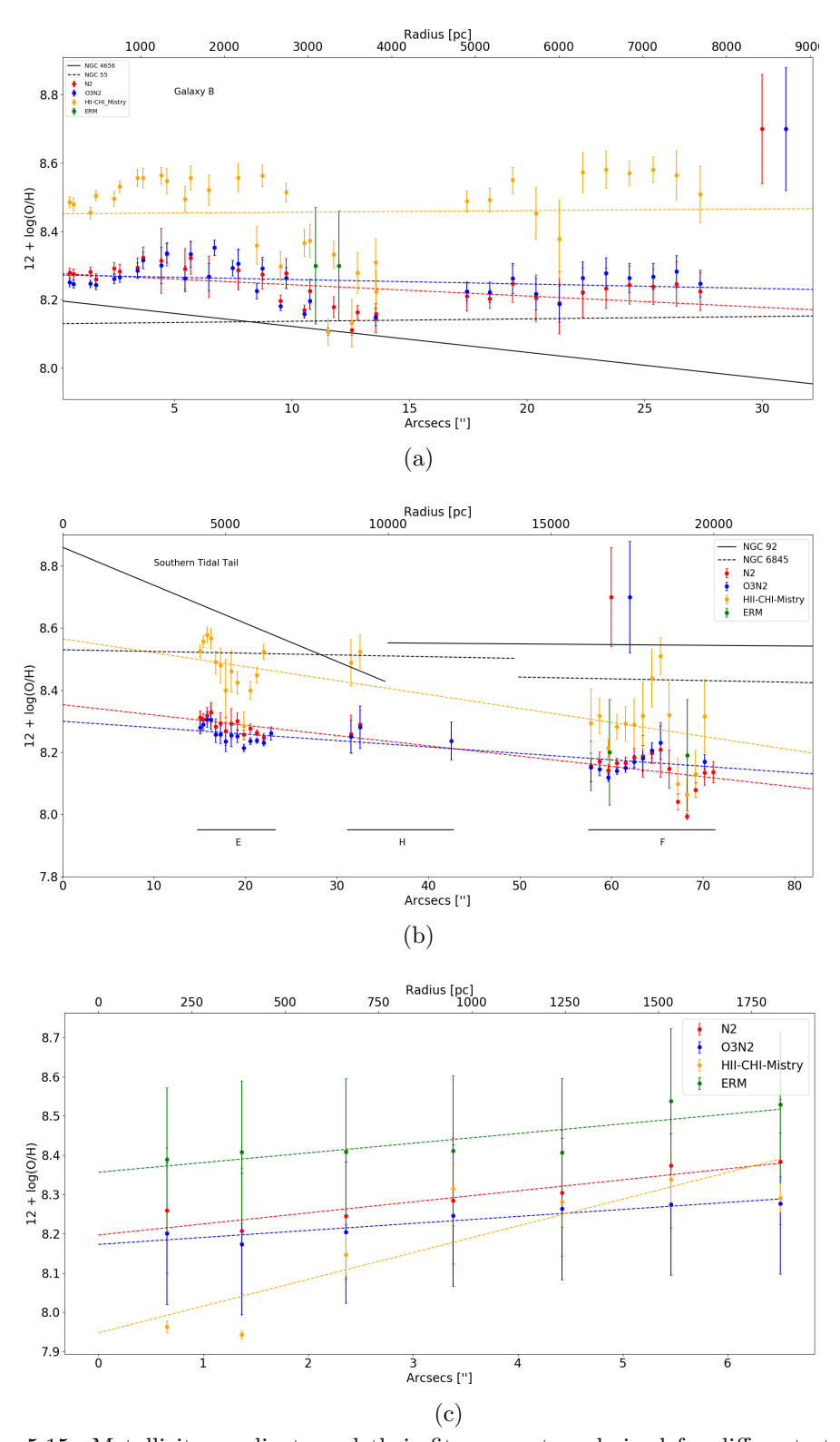


Figure 5.15: Metallicity gradients and their fit parameters derived for different structures in HCG 31; (a) Galaxy B. (B) southern tidal tail and (c) the central zone. For comparation we include the gradients of other similar objects in panels (a) and (b). The linear regression were performed using the package CURVEFIT from SCIPY which allow us to consider the uncertainties to perform the linear regression.

ing feature that could be related to gas flows on the galaxy. Sánchez et al. (2014) found the same behaviour on some galaxies of their sample, and they propose that in many cases this drop is produced by the presence of a star-formation ring at the nuclear region of the galaxy. This scenario is difficult to prove on HCG 31 B because its nearly edge-on, therefore we cannot discard it. However, we can speculate that a gas inflow induced by the interaction with the HCG1 A+C complex is diluting the central metallicities and triggering star-formation at the central zone of this galaxy, producing the central drop on the metallicity gradient.

In Figure 5.15b we show the metallicity gradient of the southern tidal tail, which include members E, H and F. Uncertainties represent the propagation of the flux errors, and on the top right are represented the associated uncertainty of the empirical calibrators (0.16 dex for N2 and 0.18 dex for O3N2). Gradient starts at the midpoint between knots A and C (HCG31 A+C complex) given that some authors suggest that this tail is formed from material detached from galaxy C (Amram et al. 2007). On Figure 5.15b we include the oxygen abundance distributions of other tidal tails located in compact group galaxies, namely NGC 92 (Torres-Flores et al. 2014) and NGC 6845 (Olave-Rojas et al. 2015). We note that NGC 92 and NGC 6845 are spiral galaxies that belong to groups in less advance interaction stage (no strong evidence of merge in these systems). Inspecting Figure 5.15b we find, i) the tidal tail of HCG 31 is less metallic than NGC 92 and NGC 6845 by ~ 0.4 dex and ~ 0.3 dex respectively and ii) the scale lengths are quite different, the tidal tail of NGC 92 starts at a radius of ~ 10 kpc and extends upon ~ 25 kpc; for NGC 6845 the tail starts at ~ 14 kpc and extends upon ~ 70 kpc, while the southern tail of HCG 31 starts at ~ 3 kpc and extends upon ~ 20 kpc. Figure 5.15b shows the same trend among the different method. An offset of ~ 0.3 dex is detected in the case of the HII-CHI-Mistry method.

Flat metallicity gradients can be explained due to gas flows induced during galaxy-galaxy interactions (e.g Rupke et al. 2010b). Given that, one could expect to find a velocity gradient through the tidal tail, but as explained in Section 5.1.1, the position-velocity diagram through the southern tidal tidal reveals a velocity gradient only through objects E and H, where F presents a flat velocity gradient because is kinematically detach from the tail. These findings suggest that gas flows could be the explanation of the flat gradient only for objects E and H. For member F, a metal-poor gas accretion that trigger star formation (Amram et al. 2007) could be the explanation for its slightly lower metallicity.

Method	Zero point [dex]	Slope [dex/kpc]			
Galaxy B					
N2	8.26 ± 0.02	-0.012 ± 0.002			
O3N2	8.27 ± 0.01	-0.004 ± 0.001			
HII-CHI-Mistry	8.43 ± 0.03	0.002 ± 0.001			
ERM	8.14 ± 0.01	0.049 ± 0.001			
	Southern Tail				
N2	8.35 ± 0.02	-0.012 ± 0.001			
O3N2	8.29 ± 0.01	-0.007 ± 0.001			
HII-CHI-Mistry	8.61 ± 0.03	-0.020 ± 0.001			
ERM	8.14 ± 0.01	0.049 ± 0.001			
A+C Complex					
N2	8.19 ± 0.02	0.100 ± 0.010			
O3N2	8.17 ± 0.01	0.063 ± 0.006			
HII-CHI-Mistry	7.87 ± 0.03	0.234 ± 0.032			
ERM	8.36 ± 0.03	0.088 ± 0.013			

Table 5.4: Results of the linear regression for the different gradients of HCG 31

Using Gemini/GMOS datacubes, Torres-Flores et al. (2015) find a metallicity gradient that connects the knots A and C at the central zone of HCG 31. In order to revisit its result we simulate a slit connecting the knots A and C (white segment on Figure 5.12a). The gradients obtained with the different methods are presented on Figure 5.15c. The ERM method shows a very homogeneous distribution of the oxygen abundance, with an average of $12 + log(O/H) \sim 8.40$, from 0 to \sim 5 arcsec, and a slightly increasing to $12 + log(O/H) \sim 8.55$ at ~ 5.5 arcsec, corresponding to knot A. A linear fit on this gradient give us a slope of $\alpha = 0.088 \pm 0.013$ dex/kpc, which is lower with respect to the gradient found by these authors, 0.15 ± 0.10 dex/kpc. However, if we compare it with our gradient obtained with the N2 method (the same used by the authors) we find a very good agreement $(0.10 \pm 0.1 \text{ dex/kpc})$.

5.5 H α luminosities and star formation rates: Witnessing the stellar birth in a merging system

Using the H α map, corrected by extinction and distance, we derive the SFR map of HCG 31, which is shown in Figure 5.16. This map was obtained by using

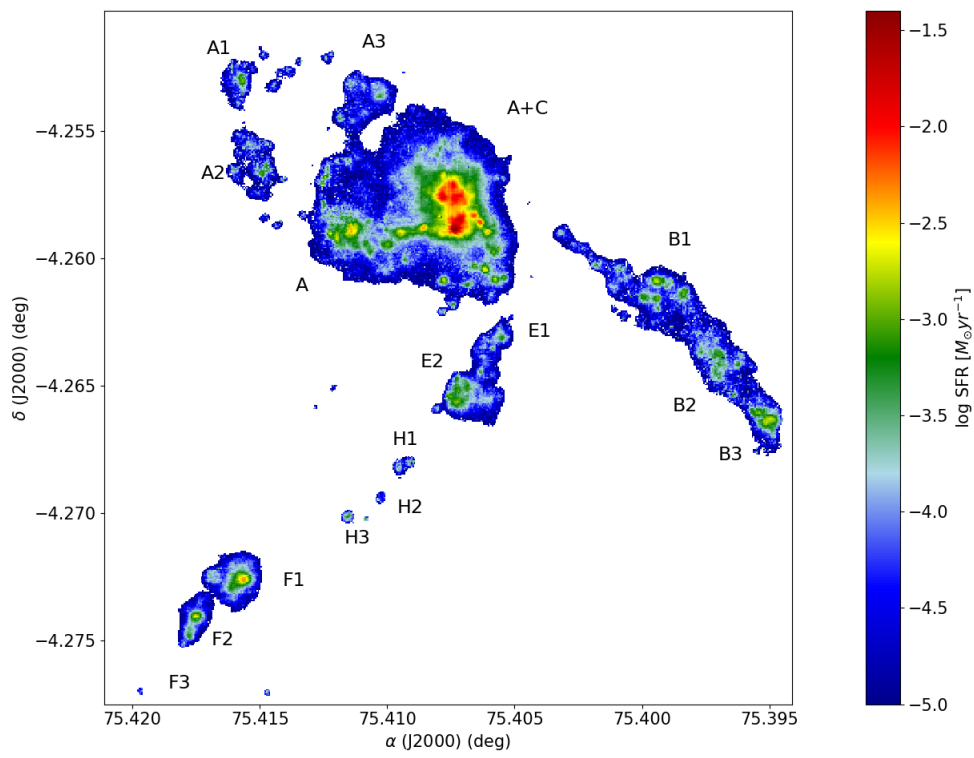


Figure 5.16: Map of star formation rate for HCG 31 derived using the calibration of Kennicutt & Evans (2012)

the calibration proposed by Kennicutt & Evans (2012).

In order to have a complete picture of the SFRs in different knots in HCG 31, we run SExtractor on the H α map to locate the most brigther H α knots in HCG 31. We slightly change the input parameters of SExtractor to obtaining a visually satisfactory result. For the central region it was necessary to use a different convolution filter. The input parameters that we use on SExtractor were; DETECT_MINAREA = 30, DETECT_TRESH = 9, ANALYSIS_TRESH = 6 and we use the default.conv convolution filter for the outer zones, and mexhat_5.0_11x11.conv for the central zone. This approach allowed us to obtain a segmentation map, whose different regions are presented on Figure 5.17. We detect a total of 46 different H α knots through the system, 20 on the A+C complex, 9 on HCG 31 B, 4 on HCG 31 E, 2 in HCG 31 H, 3 on HCG 31 F, 1 on HCG 31 A1, 2 on HCG 31 A2 and 3 on HCG 31 A3. All these H α knots are spatially consistent with the detection of super star cluster and star-formation complexes previously performed by Gallagher et al. (2010) on deep HST images.

In order to obtain a more robust determination of the SFR, we take the inte-

grated spectra of each knot and obtain the total H α flux and the SFR for each knot. The results are presented on table 5.5 including the SFR derived with the calibration of Kennicutt & Evans (2012) and Kennicutt (1998a). It should be noted that we use the integrated spectra to obtain the average H α luminosity for each knot. We do not average the values of H α obtained for each spaxel (from 2D analysis).

The HCG 31 A+C complex is the region with the major number of knots, 20 in total. Knots 31 and 36 are representative of the knots C and A that we define on previous sections. These knots have equal H α luminosities (consistent with Alfaro-Cuello et al. 2015), having $logL(H\alpha) \sim 40.98[ergs \times s^{-1}]$. However, we note that knot 31 is more extended. Adding the H α luminosities of all knots that belongs to the inner A+C complex (i.e knots 31,32,33,34,35,36 and 39) we obtain a total of $logL(H\alpha) = 41.53 \pm 0.07[ergs \times s^{-1}]$, which is translate into a SFR of $2.64 \pm 0.43 M_{\odot}yr^{-1}$ (using the calibration of Kennicutt (1998a)). This value is consistent with previous determinations, e.g López-Sánchez et al. (2004) obtained a SFR of $2.74 M_{\odot}yr^{-1}$ for the inner part of the A+C complex (see table 9 in their work) and Alfaro-Cuello et al. (2015) obtained a SFR of $2.86 \pm 0.14 M_{\odot}yr^{-1}$ for this zone.

In the case of A+C as a whole, if we add the H α luminosities of the 20 knots identified on this region, we obtain a total of $logL(H\alpha) = 41.57 \pm 0.07 [ergs \times s^{-1}]$ which is equivalent to a SFR of $2.99 \pm 0.49 M_{\odot} yr^{-1}$, which is lower than previous determinations for the entire complex. However, if we calculate the SFR considering all the spaxels of the A+C complex, we obtain a SFR of $\sim 10.99 M_{\odot} yr^{-1}$, which is consistent with previous determinations for the system, e.g Alfaro-Cuello et al. (2015) obtain a SFR of 11.06 $M_{\odot} yr^{-1}$ for the A+C complex. The difference between the results obtained by adding the luminosities of the knots and the spaxel-by-spaxel determination could be due to the unresolved SF knots lying on the ISM of the A+C complex, which are considered in the second method and not in the first one.

For the A1, A2 and A3 objects we detect 6 knots, and for the northern tidal tidal we detect 8 knots, considering that knots 6 and 9 are part of this tail. The total H α luminosity for the northern tail is $logL(H\alpha) = 40.07 \pm 0.08 [ergs \times s^{-1}]$. We did not find in the literature other H α luminosity determination for this tail. However, López-Sánchez et al. (2004) presented the H α luminosity for the A1 object and they obtain $logL(H\alpha) = 38.76 [ergs \times s^{-1}]$, which is lower than our

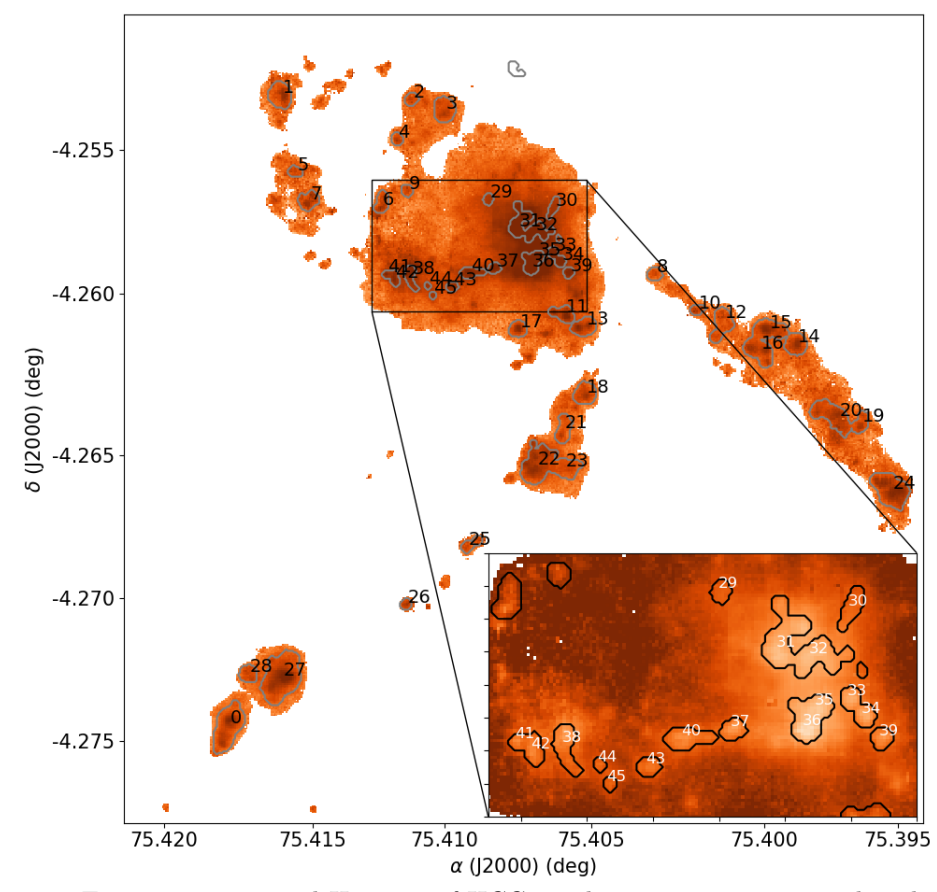


Figure 5.17: Extinction corrected $H\alpha$ map of HCG 31, the contours represent the edges of the segmentations obtained by SExtractor, each knot are labeled with their respective ID

value for the knot 1 of $log L(H\alpha) = 39.54 \pm 0.1 [ergs \times s^{-1}]$. We note that this difference could be due to aperture effects or by the use of a different extinction law. The total SFR obtained for the northern tidal tail is $0.09 \pm 0.02 M_{\odot} yr^{-1}$.

On Galaxy B we detect 9 knots and the sum of the H α luminosities of these knots give us a total of $logL(H\alpha) = 40.67 \pm 0.06 [ergs \times s^{-1}]$, which is higher than the luminosity presented in López-Sánchez et al. (2004) of $logL(H\alpha) = 40.22 [ergs \times s^{-1}]$. However, these authors extrapolate their results obtained from their long-slit spectra, which does not cover completely the galaxy B. Thus, they consider that the galaxy follows a homogeneous distribution of the H α luminosity, which is not the case for this object (see Figure 5.16). The total SFR obtained for this galaxy using the calibration of Kennicutt (1998a) is $0.38 \ M_{\odot}yr^{-1}$

For the southern tidal tail we detect 9 H α knots, 4 in galaxy E, 2 in H and 3 in galaxy F. For object E we obtain a total H α luminosity of $log L(H\alpha) =$

 $40.26\pm0.08[ergs\times s^{-1}]$ which is slightly higher than the value obtained by López-Sánchez et al. (2004) of $logL(H\alpha)=40.05[ergs\times s^{-1}]$. The difference could be due to the same reason as for galaxy B. Mendes de Oliveira et al. (2006) also presented H α luminosities for different knots in HCG 31. For galaxy E they obtained a total luminosity of $logL(H\alpha)=39.34ergs\ s^{-1}$ (adding the E1 and E2 luminosities taken from col(6) in table 2 of their work) which is an order of magnitude lower than our determinations. Their measurements are lower limits because they did not correct their values for light loss from the slits used. For object E we derive a total SFR of $0.147\pm0.025M_{\odot}yr^{-1}$

Object H encompass knots 25 and 26 and also a third knot located between them, but its luminosity does not reach the threshold that we define to run SExtractor. The total H α luminosity obtained for this object is $logL(H\alpha) = 39.03 \pm 0.15[ergs \times s^{-1}]$ which is equivalent to a SFR of $0.008 \pm 0.003 M_{\odot} yr^{-1}$.

Galaxy F is composed by 3 principal objects F1, F2 and F3. From the H α map we only have information with good SNR for F1 (knots 27 and 28) and F2 (knot 0), which have a total H α luminosity of $logL(H\alpha) = 40.45 \pm 0.07 [ergs \times s^{-1}]$ and $logL(H\alpha) = 40.03 \pm 0.08 [ergs \times s^{-1}]$, respectively. The total H α luminosity for galaxy F (rather is a lower limit, because we do not consider F3) is $logL(H\alpha) = 40.59 \pm 0.07 [ergs \times s^{-1}]$ which correspond to a SFR of $0.311 \pm 0.049 M_{\odot} yr^{-1}$.

The total H α luminosity obtained for the southern tidal tail is $log L(H\alpha) = 40.76 \pm 0.06 [ergs \times s^{-1}] \sim 67\%$ of this luminosity comes from galaxy F, $\sim 32\%$ from galaxy E and $\sim 1\%$ from object H. The total SFR obtained for this tail is $0.467 \pm 0.072 M_{\odot} yr^{-1}$.

If we consider all the spaxels of Figure 5.16 and add its values, we obtain a SFR of $13.76M_{\odot}yr^{-1}$ using the calibration of Kennicutt (1998a) and $9.31M_{\odot}yr^{-1}$ using the calibration of Kennicutt & Evans (2012) (these values are calculated by using the total H α luminosity for HCG 31, $logL(H\alpha) = 42.23[ergs \times s^{-1}]$). In both cases our values are very similar to the value obtained by Gallagher et al. (2010) (11.06 $M_{\odot}yr^{-1}$).

ID	$\log(L(H\alpha))[ergs/s]$	$SFR_{K12} [M_{\odot}yr^{-1}]$	$SFR_{K98} [M_{\odot}yr^{-1}]$
0	40.03 ± 0.08	0.058 ± 0.011	0.085 ± 0.016
1	39.54 ± 0.10	0.018 ± 0.004	0.027 ± 0.006
2	38.79 ± 0.12	0.003 ± 0.001	0.005 ± 0.001
3	39.39 ± 0.10	0.013 ± 0.003	0.020 ± 0.005
4	38.73 ± 0.13	0.003 ± 0.001	0.004 ± 0.001
5	38.73 ± 0.14	0.003 ± 0.001	0.004 ± 0.001
6	39.17 ± 0.17	0.008 ± 0.003	0.012 ± 0.005
7	39.31 ± 0.13	0.011 ± 0.003	0.016 ± 0.005
8	38.70 ± 0.15	0.002 ± 0.001	0.004 ± 0.001
9	38.73 ± 0.11	0.003 ± 0.001	0.004 ± 0.001
10	38.75 ± 0.17	0.003 ± 0.001	0.004 ± 0.002
11	39.62 ± 0.10	0.022 ± 0.005	0.033 ± 0.007
12	39.30 ± 0.11	0.011 ± 0.003	0.016 ± 0.004
13	39.54 ± 0.09	0.019 ± 0.004	0.028 ± 0.006
14	39.57 ± 0.08	0.020 ± 0.004	0.029 ± 0.006
15	39.88 ± 0.09	0.041 ± 0.008	0.060 ± 0.012
16	39.75 ± 0.08	0.030 ± 0.005	0.045 ± 0.008
17	39.37 ± 0.10	0.013 ± 0.003	0.019 ± 0.004
18	39.41 ± 0.10	0.014 ± 0.003	0.020 ± 0.005
19	39.24 ± 0.10	0.009 ± 0.002	0.014 ± 0.003
20	39.88 ± 0.08	0.041 ± 0.008	0.060 ± 0.011
21	39.18 ± 0.11	0.008 ± 0.002	0.012 ± 0.003
22	40.08 ± 0.09	0.064 ± 0.013	0.094 ± 0.019
23	39.41 ± 0.08	0.014 ± 0.003	0.020 ± 0.004
24	40.26 ± 0.07	0.098 ± 0.016	0.144 ± 0.024
25	38.80 ± 0.17	0.003 ± 0.001	0.005 ± 0.002
26	38.64 ± 0.26	0.002 ± 0.001	0.004 ± 0.002
27	40.43 ± 0.07	0.145 ± 0.025	0.210 ± 0.040
28	39.12 ± 0.11	0.007 ± 0.002	0.010 ± 0.003
29	39.21 ± 0.07	0.009 ± 0.001	0.013 ± 0.002
30	39.60 ± 0.07	0.022 ± 0.004	0.032 ± 0.005
31	40.98 ± 0.07	0.510 ± 0.080	0.750 ± 0.110
32	40.88 ± 0.07	0.400 ± 0.070	0.600 ± 0.100
33	40.09 ± 0.07	0.066 ± 0.010	0.097 ± 0.015
34	39.96 ± 0.08	0.049 ± 0.009	0.071 ± 0.013
35	40.66 ± 0.08	0.250 ± 0.040	0.360 ± 0.060
36	40.97 ± 0.08	0.510 ± 0.090	0.740 ± 0.140
37	39.70 ± 0.09	0.027 ± 0.006	0.039 ± 0.008
38	39.82 ± 0.08	0.035 ± 0.007	0.052 ± 0.010
39	39.57 ± 0.08	0.020 ± 0.004	0.029 ± 0.006
40	39.90 ± 0.08	0.043 ± 0.007	0.063 ± 0.011
41	39.22 ± 0.09	0.009 ± 0.002	0.013 ± 0.003
42	39.55 ± 0.08	0.019 ± 0.004	0.028 ± 0.005
43	39.32 ± 0.08	0.011 ± 0.002	0.017 ± 0.003
44	38.73 ± 0.08	0.003 ± 0.001	0.004 ± 0.001
45	38.69 ± 0.09	0.003 ± 0.001	0.004 ± 0.001

Table 5.5: Star formation rates and H α luminosities for the knots identified using SExtractor. Col (1) shows the ID, Col (2) the H α luminosity. Col (3) shows the SFRs obtained with the calibration of Kennicutt & Evans (2012) and Col (4) the SFR obtained with the calibration of Kennicutt (1998a).

5.6 Estimating the ages of the different star forming burst

5.6.1 H α Equivalent width and ages

In Figure 5.18 we show the EW(H α) map of HCG 31, derived from FADO. Black contours represent the H α emission. The whole group span a range of $10\mathring{A} < EW(H\alpha) < 2000\mathring{A}$, where the highest values are associated with the galaxy F and the central merger. On the other hand, the lowest values are associated with member B. The EW map is also used to estimate the ages of the star forming knots, interpolating it with the models of STARBURST99 Leitherer et al. (1999). In this case we assume a Salpeter IMF with mass limits 1-100 M_{\odot} , an instantaneous starburst of $10^6 M_{\odot}$ and we consider 2 different metallicities, given that the metallicity of the group range from 8.19 < 12 + log(O/H) < 8.57 (section 5.4.1, see table 5.3). In this case abundances were transformed into Z, by using the solar metallicity derived by Allende Prieto et al. (2001) (Z = 0.0018) and following the equation

$$Z = Z_{\odot} \times 10^{\log(O/H) - 12 + \log(O/H)_{\odot}} \tag{5.1}$$

Then, our age estimates were performed by assuming Z=0.008 and Z=0.004 and those results are shown in (Figure 5.19a) and Z=0.008 (Figure 5.19b). It should be noted that previous works that use STARBURST99 to determine the ages of this system used the same metallicity as input (López-Sánchez et al. 2004; Alfaro-Cuello et al. 2015)

Ages are estimated on the same regions defined by the segmentation map, produced by SExtractor and used in the previous section. Results are presented in col (1), (2) and (3) of table 5.6.

Inspecting the maps, in the A+C complex we find an interesting trend near to knots A and C. In order to contextualize it, we mention a previous finding on this system. Alfaro-Cuello et al. (2015) find a super stellar cluster (SSC) in the central zone of this system. One evidence that support that finding is a small region with a low EW inside a zone of high EW. In addition, the continuum emission peak at the low EW region. Using these results, and the ages associated to the different regions, Alfaro-Cuello et al. (2015) suggest that small region with

ID	$EW(H\alpha)$ [Å]	$Age_{z=0.008}$ [Myr]	$Age_{z=0.004}$ [Myr]	$Age_M[Myr]$	$Age_L [Myr]$
0	986 ± 49	3 ± 1	4 ± 1	783	223
1	293 ± 9	5 ± 1	5 ± 1	723	250
2	353 ± 19	4 ± 1	5 ± 1	132	120
3	315 ± 9	5 ± 1	5 ± 1	399	184
4	295 ± 12	5 ± 1	5 ± 1	688	269
5	144 ± 3	5 ± 1	6 ± 1	609	343
6	243 ± 7	5 ± 1	5 ± 1	758	476
7	146 ± 3	5 ± 1	6 ± 1	763	464
8	264 ± 11	5 ± 1	5 ± 1	660	284
9	240 ± 8	5 ± 1	5 ± 1	801	447
10	607 ± 64	4 ± 1	4 ± 1	895	207
11	256 ± 2	5 ± 1	5 ± 1	776	348
12 13	219 ± 6 235 ± 3	5 ± 1 5 ± 1	5 ± 1 5 ± 1	96 806	86 412
13 14		5 ± 1 5 ± 1	5 ± 1		570
15	207 ± 2 344 ± 11	5 ± 1 5 ± 1	5 ± 1 5 ± 1	869 610	195
16	344 ± 11 217 ± 2	5 ± 1 5 ± 1	5 ± 1 5 ± 1	737	433
17	324 ± 6	5 ± 1	5 ± 1	843	443
18	359 ± 10	4 ± 1	5 ± 1	308	167
19	195 ± 2	5 ± 1	6 ± 1	847	528
20	89 ± 2	6 ± 1	7 ± 1	873	414
$\frac{20}{21}$	394 ± 18	4 ± 1	5 ± 1	754	282
22	431 ± 9	4 ± 1	4 ± 1	90	61
23	121 ± 1	6 ± 1	6 ± 1	108	67
24	448 ± 6	4 ± 1	4 ± 1	554	137
25	508 ± 77	4 ± 1	4 ± 1	8	7
26	675 ± 197	4 ± 1	4 ± 1	664	194
27	1047 ± 31	3 ± 1	4 ± 1	215	65
28	666 ± 59	4 ± 1	4 ± 1	97	85
29	254 ± 2	5 ± 1	5 ± 1	53	41
30	1293 ± 24	3 ± 1	3 ± 1	1024	276
31	721 ± 2	4 ± 1	4 ± 1	47	24
32	816 ± 4	4 ± 1	4 ± 1	36	22
33	1061 ± 5	3 ± 1	4 ± 1	66	29
34	760 ± 7	4 ± 1	4 ± 1	30	15
35	639 ± 4	4 ± 1	4 ± 1	60	36
36	837 ± 6	3 ± 1	4 ± 1	230	77
37	258 ± 2	5 ± 1	5 ± 1	648	247
38	138 ± 1	6 ± 1	6 ± 1	357	108
39	365 ± 2	4 ± 1	5 ± 1	172	94
$\frac{40}{41}$	139 ± 1	$6 \pm 1 \\ 5 \pm 1$	6 ± 1	944 827	341
$\frac{41}{42}$	253 ± 3		5 ± 1		501
	271 ± 3	5 ± 1	5 ± 1	982 937	344 604
43	188 ± 1	5 ± 1	$6 \pm 1 \\ 6 \pm 1$		604
$\frac{44}{45}$	$ \begin{array}{r} 197 \pm 2 \\ 272 \pm 5 \end{array} $	5 ± 1		900 866	685 733
45	212 ± 5	5 ± 1	5 ± 1	800	/ ১১

Table 5.6: Ages and EW obtained with different methods of the knots of HCG 31; Col (1) shows the ID of every knot. Col(2) shows the EW derived by FADO. Col (3) shows the age obtained interpolating with the models of S99, assuming a metallicity of z = 0.008. Col (4) Shows the age obtained with S99 but assuming a metallicity of z = 0.004. Col (5) Shows the mass-weighted age of the population vector fitted by FADO and Col (6) shows the light-weighted age obtained by FADO. We note that uncertainties for columns (5) and (6) are lower than 10 Myrs, as discussed in the text. Cols (3) and (4) represents the age of the last episode of star formation. On the other hand, cols (5) and (6) shows the weighted age of the stellar popularion fitted by FADO.

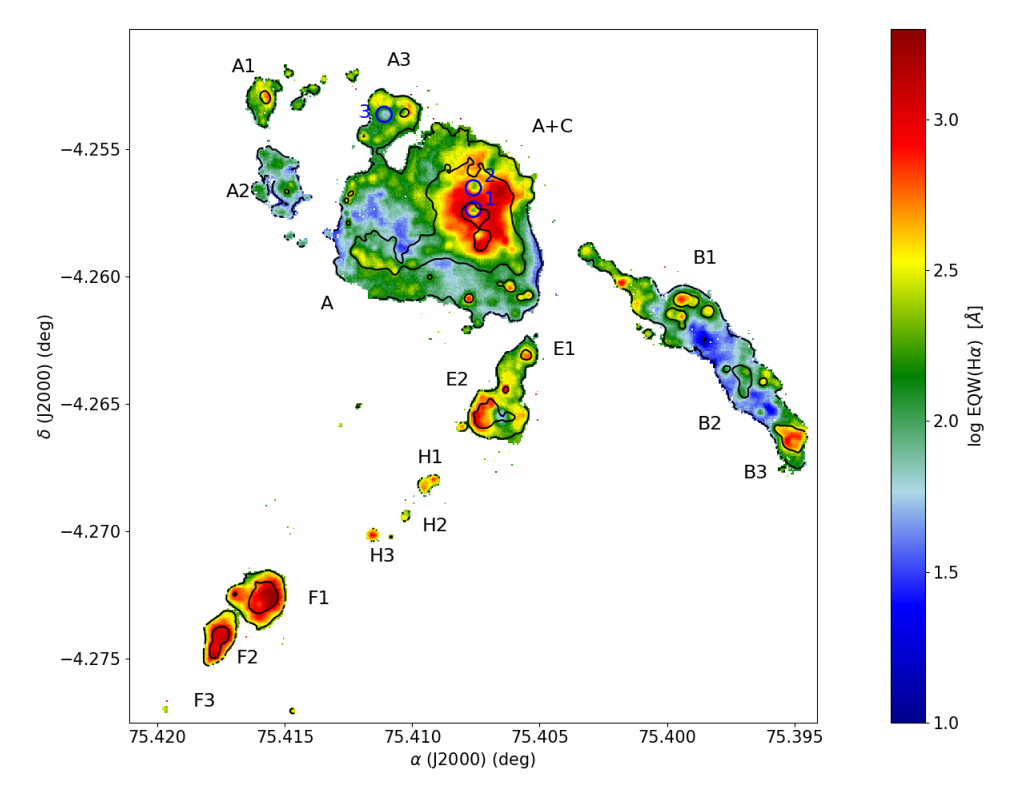


Figure 5.18: Map of H α equivalent width derived by FADO, black contours represent H α in emission

low EW corresponds to an SSC that is triggering star formation in its surroundings. We find the same trend in the same region, confirming their result (at $\alpha = 75.4076^{\circ}$, $\delta = -4.25737^{\circ}$) but also we find a similar trend at the north of this SSC (at $\alpha = 75.4076^{\circ}$, $\delta = -4.2564^{\circ}$), as can we see in Figure 5.18 circles 1 and 2 respectively. Both zones display similar EW, with $ew(H\alpha) \sim 200 \mathring{A}$ (~ 6 Myr) and are surrounded by similar ews of $ew(H\alpha) \sim 800 \mathring{A}$ (~ 4 Myr) the possibility of other SSC will be discussed on section 6.

Knots A and C have similar values of EW, i.e., $\sim 720 \text{Å}$ and $\sim 840 \text{Å}$ respectively (~ 5 Myr and $\sim 4\text{-}5$ Myr depending on the metallicity). These high values are consistent with the scenario of a recent starburst at the central zone of this merger (Iglesias-Paramo & Vilchez 1997, Johnson & Conti 2000).

The main body of galaxy A has lower EW values than region A+C, spanning a range of $30\mathring{A} < ew(H\alpha) < 400\mathring{A}$ (5-10 Myr), while region A+C range between $300\mathring{A} < ew(H\alpha) < 1600\mathring{A}$ (3-5 Myr). The higher values at the central region should be a consequence of the starburst triggered by the merger.

The three principal members of the northern tidal tail (A1, A2, and A3)

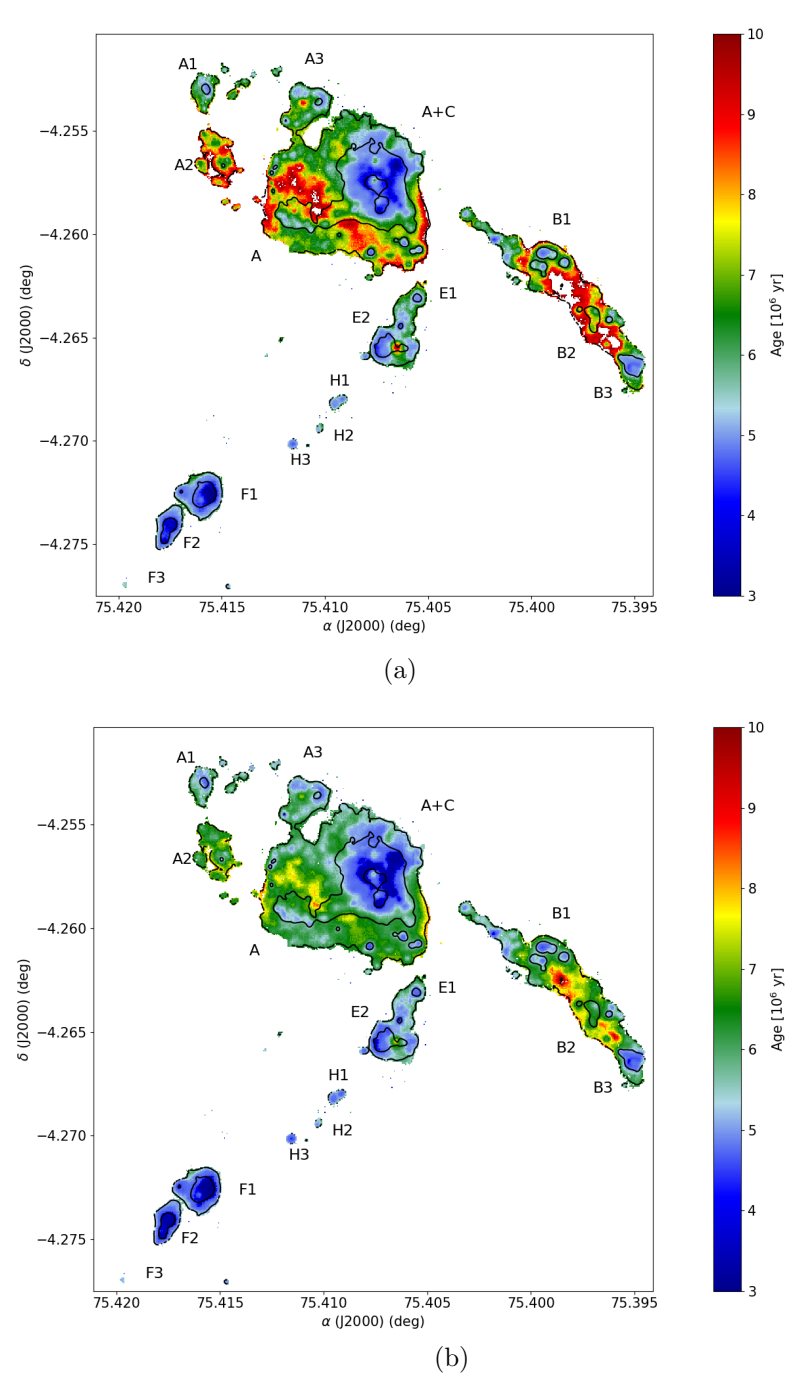


Figure 5.19: Map of ages obtained interpolating with the models of Starburst99 assuming an instantaneous star formation event, a Salpeter IMF was assumed with mass limits 1-100 M_{\odot} and with different metallicites; (a) with Z = 0.004 and (b) with Z = 0.008.

shows very different trends on the EQW(H α) map. A1 spans a wider range of ew with $60\mathring{A} < ew(H\alpha) < 660\mathring{A}$ (5-10 Myr). The peak of EQW(H α) are correlated with the H α knot of this object (~ 5 Myr). A2 shows a homogeneous ew distribution, spanning a range of $30\mathring{A} < ew(H\alpha) < 250\mathring{A}$ (6-10 Myr) with an average of $ew(H\alpha) \sim 90\mathring{A}$ (6-7 Myr depending on the metallicity). A3 is the more interesting object of this tail. It spans a range of $50\mathring{A} < ew(H\alpha) < 400\mathring{A}$ (5-9 Myr) and as for A1 and A2, the peak of ew is correlated with the H α knot of the object. An interesting feature is observed on this object that is not present on the other members of this tail. To the east of the H α knot (at $\alpha = 75.4111^{\circ}$, $\delta = -4.25363^{\circ}$) a small region with lower ews (7-9 Myr depending on the metallicity) is observed and it is surrounded by regions of higher ews (~ 5 Myr on average), as can be seen in Figure 5.18 (circle labeled with a number 3). The presence of an SSC in this object will be discussed on section 6.

Galaxy B shows a wide range of EW, ranging from $10\mathring{A} < EW(H\alpha) < 970\mathring{A}$ (3-10 Myr). The lowest values of ew across HCG 31 are found on this galaxy, specifically between knots B2 and B1 and between knots B2 and B3. The knot B1 encompass three different regions; 14, 15 and 16 (see Figure 5.17), which have ews of $207 \pm 2\mathring{A}$ (~ 6 Myr), $344 \pm 11\mathring{A}$ (~ 5 Myr) and $217 \pm 2\mathring{A}$ ($\sim Myr$), respectively. The knots B2 and B3 have EW ranging from $89 \pm 2\mathring{A}$ (~ 7 Myr) to $448 \pm 6\mathring{A}$ (~ 5 Myr). On the bridge that connects this galaxy and the A+C complex we find 3 main knots (knots 8, 10 and 12 in Figure 5.17). These knots with have of $264 \pm 11\mathring{A}$, $607 \pm 64\mathring{A}$ and $219 \pm 6\mathring{A}$ respectively (~ 5 Myr for the three knots), suggesting a recent star formation in the bridge.

Four knots are detected on galaxy E (18, 21, 22, and 23), having young ages, $40\mathring{A} < ew(H\alpha) < 1070\mathring{A}$ (3-10 Myr). The most interesting feature on this galaxy is that knots 22 and 23 are very close to each other and they show very different EWs. Both knots display a significant difference in EW, which indicate an ongoing burst just in one of them despite its proximity.

Object H displays high values of EW, with $ew(H\alpha) = 508 \pm 77 \text{Å}$ for H1 (knot 25) and $ew(H\alpha) = 675 \pm 197 \text{Å}$ for H3 (knot 26), (~ 4 Myr for both knots). These high values suggest that H is a young object with recent star formation.

Galaxy F is probably the younger member of HCG 31 (Iglesias-Paramo & Vilchez 1997, López-Sánchez et al. 2004) and our ew and age map suggests the same. The EW range of this object is $150\mathring{A} < ew(H\alpha) < 2000\mathring{A}$ (3-6 Myr). Probably a gas accretion across the tail is triggering the starburst in object F. By

using SExtractor we detect 3 knots on this object: 0, 27 and 28, which have EW of: 986 ± 49 Å, 1047 ± 31 Å and 666 ± 59 Å respectively (3-4 Myr for knots 0, 27 and 5 Myr for knot 28), suggesting very similar ages of objects F1 and F2.

In general, comparing our ages estimates with previous works, we find a very good agreement with the determinations of Iglesias-Paramo & Vilchez (1997), Johnson & Conti (2000), López-Sánchez et al. (2004) and Alfaro-Cuello et al. (2015).

5.6.2 Ages estimates through stellar populations: FADO

In order to have an idea of the age of the underlying stellar population we use the ages derived by FADO. Age maps are shown in Figure 5.20a and 5.20b, for mass-weight and luminosity-weighted ages, respectively black and white contours on these maps represent the H α and continuum emission, respectively. In Table 5.6, columns (4) and (5), we list the ages derived from this analysis, for each knot. Due to the faint continuum of the spectra the maps seem to be noisy. Therefore, will use these results in a more qualitative way taking into consideration only the order of magnitudes of the ages. It should be noted that the uncertainties given by FADO were very low (< 10Myr) and probably underestimate the actual value of the uncertainty. Considering these results, and the fact that the continuum detected is very faint, we will mainly focus in the order of magnitude of the ages from a qualitative point of view.

In the A+C complex a clear correlation between the ages of $log\ age[yr] \sim 7.5-8$ and the continuum emission is observed in both maps. The knot C (31 in table 5.6) display a young stellar population with an age < 50 Myr. For knot A (36 in table 5.6) we find a mass-weighted age of 230 Myr, and a luminosity-weighted age of 77 Myr. This difference could be due to the recent starburst that forms new massive, luminous and young stars that are "contaminating" the actual age of the underlying stellar population. However, the mass-weighted age -230 Myr—indicate that knot A presents an older underlying stellar population than knot C.

We found that the youngest knots in the central zone, with a mass-weighted age < 100 Myr (knots 29,31,32,33,34 and 35), traces a projected diagonal line from NE to SW.

For the other knots of the central complex, which are part of the main body of galaxy A (knots 36-45), we find very similar mass-weighted ages between knots

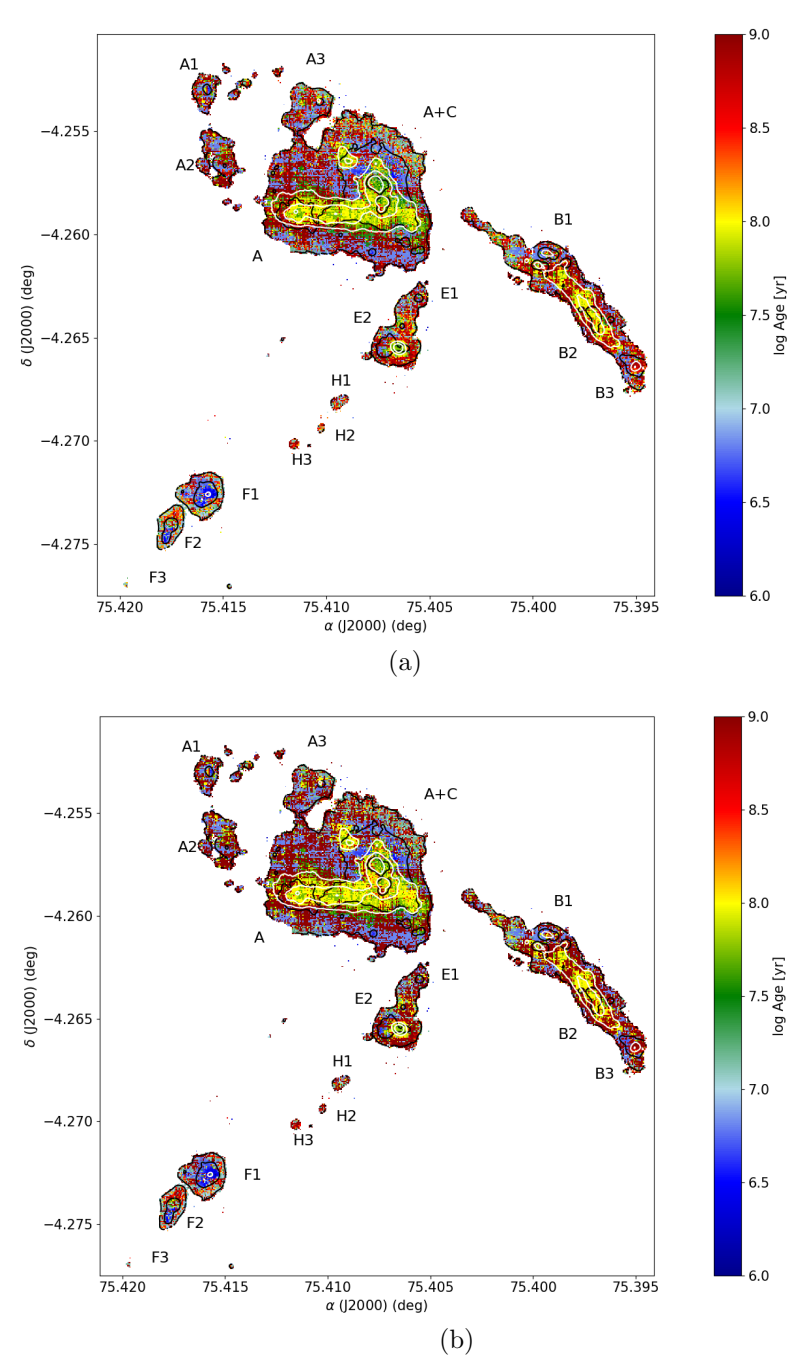


Figure 5.20: Ages derived through the population synthesis performed by FADO, black contours represent $H\alpha$ in emission and white contours represent continuum emission (a) Luminosity-weighted Age and (b) Mass-weighted age.

 $40-45 \ (\sim 900 \ \mathrm{Myr}).$

For galaxy B, we find a spatial correlation between the ages of $log\ age\ [yr]=8$ and the continuum emission, in a similar way than the case of the central zone. The knots of this galaxy (8,10,12,14,15,16,19,20,24) span a range of mass-weighted ages of 554-895 Myr, excepting knot 12 which has 96 Myrs and 86 Myrs, mass-weighted and luminosity-weighted ages, respectively. Probably it is a young star-cluster formed during the interaction events produced in HCG 31.

In the case of member E, the most interesting feature is the age difference between knots 22 and 23. There is an offset between the H α emission peak (knot 22) and the continuum emission peak knot (23). If we inspect the ages of the underlying stellar population of these knots we did not find a large difference; knot 23 is \sim 20 Myr older than knot 22. However, the age map on this region seems to be very noisy, thus our determinations of ages are only lower limits.

The knots on galaxy F (0, 27 and 28) shows different ages. For object F1 (knots 27 and 28) we find mass-weighted ages of 215 Myr and 97 Myr respectively, suggesting young stellar populations as expected for this object, however. For F2 (knot 0) we find a mass-weighted age of 783 Myr which is slightly higher than expected, probably evidence that this object was stripped from galaxy C and still maintains its underlying stellar population.

5.7 Wolf-Rayet bump

Several previous studies have detected WR features in the spectra of HCG 31 (e.g Kunth & Schild 1986, López-Sánchez et al. 2004, López-Sánchez & Esteban 2010). Kunth & Schild (1986) were the first authors to report WR features in HCG 31. They detect He_{II} 4686 Å and N_{III} 4640 Å features, that are related to the emission of WN stars. Guseva et al. (2000) detect the same lines and added N_{III} 4512Å and Si_{III} 4565Å at the central zone of HCG 31. The blending of all these lines in the spectra of a galaxy is the so-called blue bump and it is widely used on literature to estimate the number of WN stars in a galaxy (e.g. Vacca & Conti 1992, López-Sánchez & Esteban 2010). In the case of HCG 31, López-Sánchez et al. (2004) also detect the blue bump on their long-slit spectra. In our case, the spectral coverage of our data does not allow us to detect completely the blue bump. However, we can detect another feature that is related to emission of WC stars, the so-called red bump. This red bump is produced due to the line

 C_{IV} 5808Å and for HCG 31 this feature is very weak and difficult to detect, e.g. Guseva et al. (2000) and López-Sánchez et al. (2004) do not detect this line in their spectra, probably because the WR population of this system is dominated by WN stars (Guseva et al. 2000, López-Sánchez & Esteban 2010). Nevertheless, in our data we can detect this weak feature at the central zone of this system.

In order to map the red bump we perform a linear fit to the continuum near to the feature and then we substract it from the data. Using the continuum-substracted spectra we collapse the datacube in the range 5838-5934 \mathring{A} (red segmented lines in Figure 5.21a), producing a 2D image. The obtained map is presented on Figure 5.21b, where we detect the red bump only in the inner central zone of HCG 31 A+C.

It should be noted that the spatial location of the WC stars is consistent with the ages estimated for this zone in the previous section (5-6 Myr). This fact could suggest that almost all the knots in HCG 31 should present WR features. Probably the spectral features are just too faint to be detected on other regions. Furthermore, the red bump is much fainter than the blue one, thus a region rich in WN stars but poor in WC would be not detected. Therefore, our estimations of the number of WC stars are lower limits.

We integrate all the spectra of the spaxels seen in Figure 5.21b. The obtained spectra is shown in Figure 5.21a, where the most important lines labeled and a gaussian fit is show with a red segmented line. The luminosity obtained for the red bump is $L_{obs}(C_{IV}5808\text{Å}) = 1.09 \times 10^{39} \pm 0.05 \times 10^{38} [ergs^{-1}]$. In order to obtain the number of WC stars we follow the equations presented by López-Sánchez & Esteban (2010),

$$N_{WCE} = \frac{L_{obs}(C_{IV}5808\mathring{A})}{L_{WCE}(C_{IV}5808\mathring{A})}$$
(5.2)

where $L_{WCE}(C_{IV}5808\mathring{A})$ depends on the metallicity and its given by:

$$L_{WCE}(C_{IV}5808\mathring{A}) = (-8.198 + 1.235x) \times 10^{36} ergs\ s^{-1}$$
 (5.3)

with x=12+log(O/H). In the case of HCG 31 we assume the average metallicity obtained for the inner central zone of the system $12+log(O/H)=8.43\pm0.19$. In this case we obtain $L_{WCE}(C_{IV}5808\mathring{A})=2.21\times10^{36}\pm2.35\times10^{35}ergs~s^{-1}$, which translate into $N_{WCE}=492\pm75$.

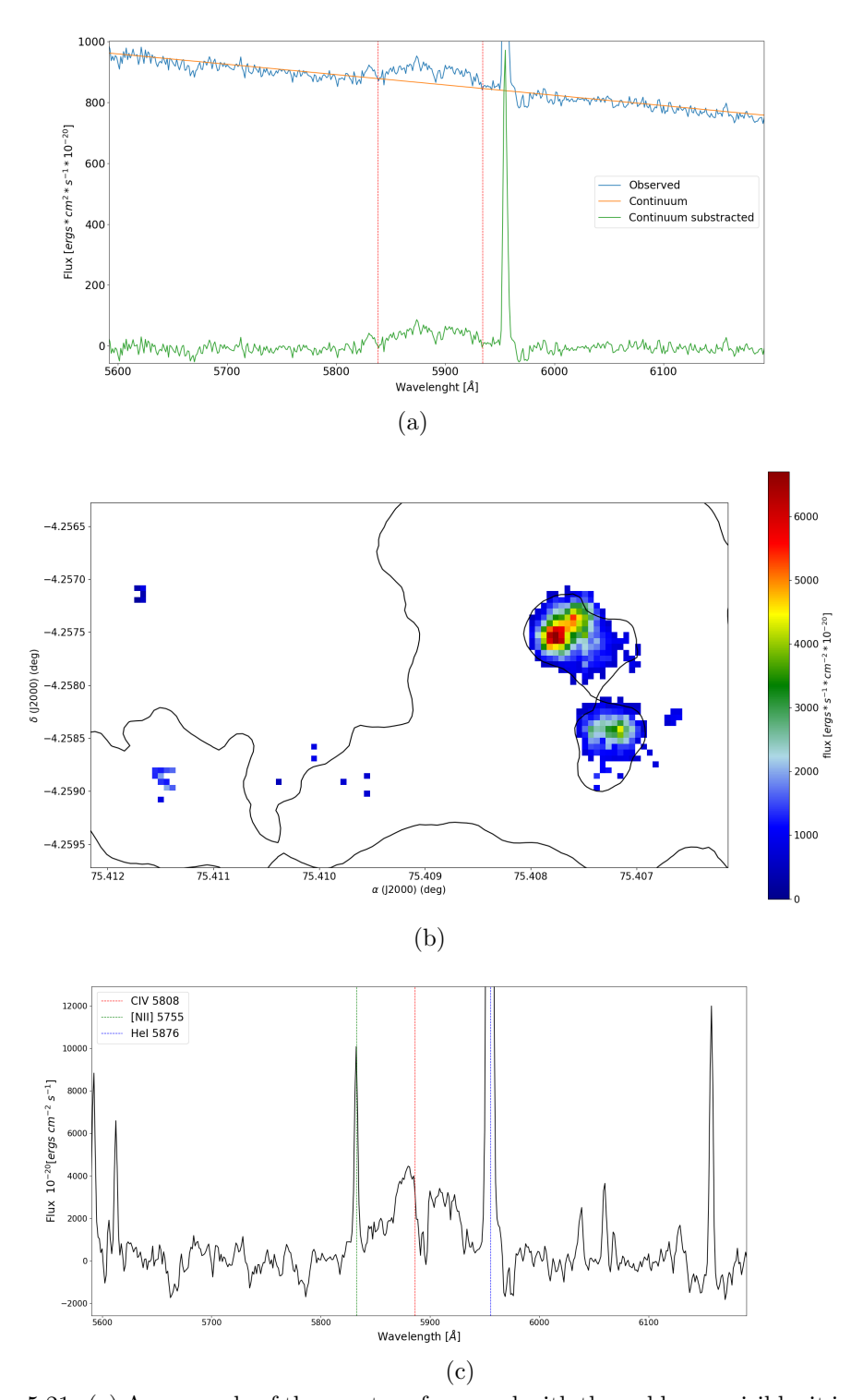


Figure 5.21: (a) An example of the spectra of a spaxel with the red bump visible, it is also shown the continuum fit performed for all the spaxels in order to map the red bump, (b) Intensity map of the red bump obtained for the central region of HCG 31, black contours represent $H\alpha$ in emission and (c) Integrated spectra of all the spaxels in (b) with the gaussian fit performed to estimate the number of WC stars in the central region of HCG 31

The number of WCE stars in HCG 31 was also estimated by different authors. Guseva et al. (2000) obtain N(WCE) = 246 and López-Sánchez & Esteban (2010) obtain N(WCE) = 206. Our number is two times higher than previous studies. However, it is important to note that previous works obtain the number of WCE stars from long-slit spectroscopy instead of integral field spectroscopy, therefore, aperture effects cannot be neglected.

5.8 Ionization Mechanism

We used standard diagnostic diagrams to understand the ionization mechanisms in HCG 31. In Figure 5.22 we show the spatially resolved diagnostic diagrams, where panels (a), (b) and (c) are the $[O_{III}]/H\beta$ vs $[N_{II}]/H\alpha$, $[O_{III}]/H\beta$ vs $[S_{II}]/H\alpha$ and $[O_{III}]/H\beta$ vs $[O_{I}]/H\alpha$, respectively. We find that most of the system is primarily ionized by massive stars due to the recent star formation (pink points in Figure 5.22). Yellow points represent ionization by shocks/LINER, which are negligible, as can be seen in Figure 5.22a. However, in Figures 5.22b and 5.22c yellow points arise from the outskirts of the central merger, where the line ratios could be contaminated by a diffuse ionized gas (DIG). We cannot discard that shocks are the ionization mechanism at these external locations. Red points are associated with AGN as the main ionization mechanism, however this is unlikely, because the spatial distribution of the red points is not consistent with the presence of an AGN. If this was the case, we should find a more central distribution, not a random distribution in the outskirts, which is what we see in Figures 5.22b and 5.22c.

Inspecting the central zone we find that knot A lies in the composite region in the diagnostic ionization diagram that use the $[N_{II}]/H\alpha$ ratio. In order to highlight it, in Figure 5.23 we present a zoom of the central region with their respective ionization diagnostic diagram. This behaviour could be associated with a violent star formation event that is triggering massive stellar winds and shocks. If we inspect the velocity dispersion map (σ_v) on this zone we find that it presents $\sigma_v \sim 60 \ km \ s^{-1}$ which is lower than the velocity expected for shocks $(\sigma_v > 90 \ km \ s^{-1}$, Rich et al. 2015), but higher than the velocity expected for a regular HII region in a dwarf galaxy $(\sigma_v \sim 30 km \ s^{-1}$, Moiseev et al. 2015). However, as mentioned in previous sections, probably the widths that we are measuring are overestimated due to multiple unresolved components, thus the velocity dispersion

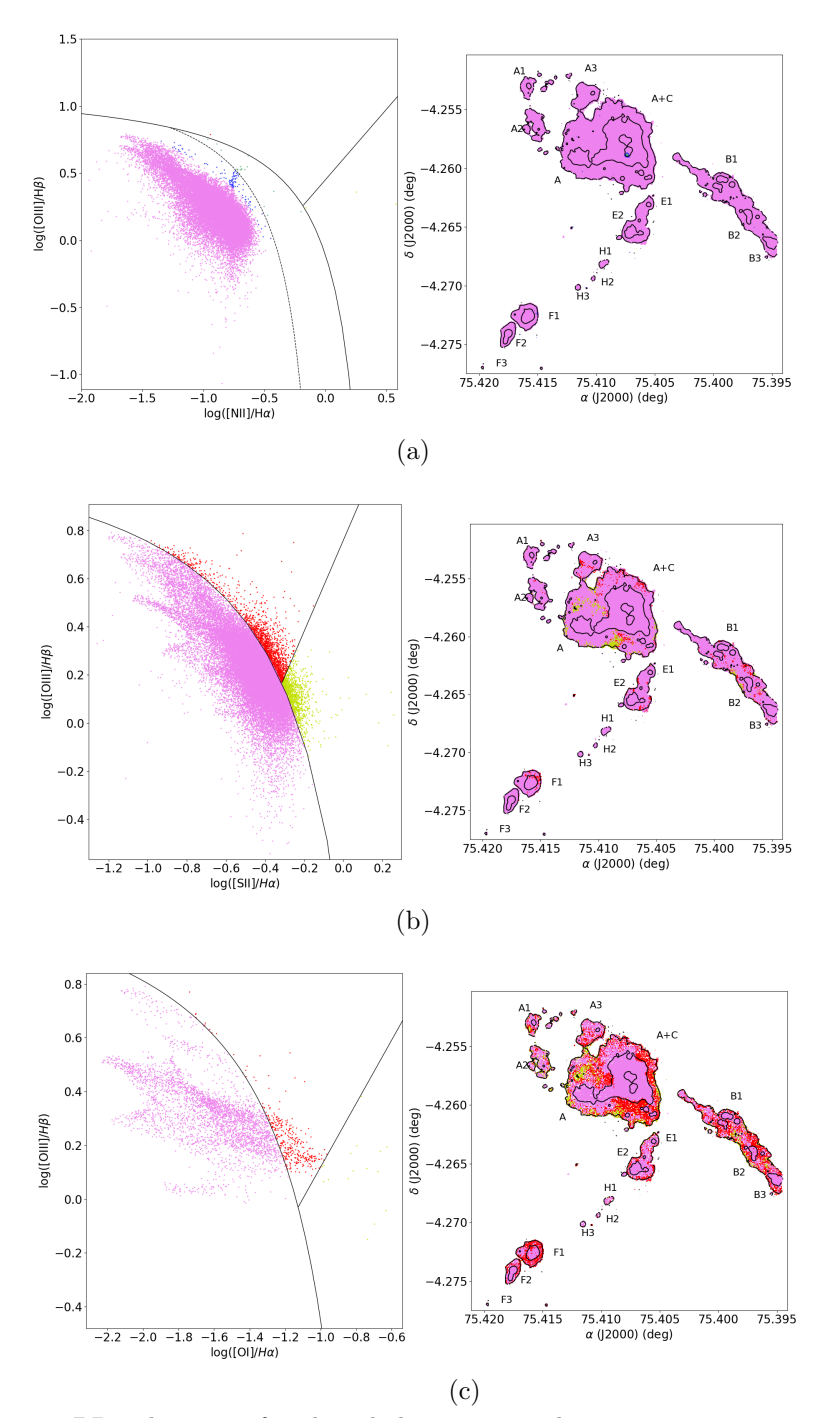


Figure 5.22: BPT diagrams for the whole system. The contours represent $H\alpha$ in emission. Mostly of the points lies in the SF sequence. Almost all points in the AGN/LINER zones lies in the outskirts of the galaxy. Probably due to the low S/N on these regions, or to an eventual contribution of shocks/DIG.

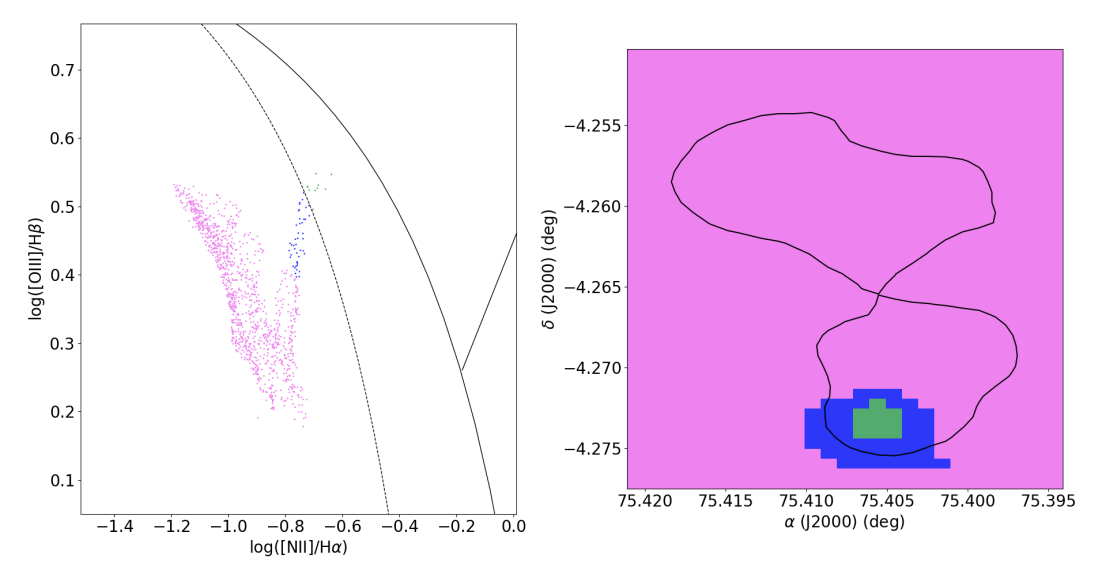


Figure 5.23: BPT diagram of the inner zone of the A+C complex. We see a composite ionization in the HCG31 A knot, this is probably a contribution of shocks on this region, also this region presents a peak in the electron density ($\sim 200~cm^{-3}$)

that we present is an upper limit for this region. The mentioned above allow us to conclude that this knot is ionized by a combination of shocks and star-formation. This scenario is supported by a high $H\alpha$ EW and high $H\alpha$ luminosity (SF evidence) and the line ratios obtained (shocks/composite ionization evidence). The main ionization mechanism for the remaining galaxies is the star formation.

López-Sánchez et al. (2004) show a diagnostic diagram for this system based on their spectroscopic long-slit data. They find a larger contribution of shocks than our results. However, all the points on their diagram lies very close to the theoretical limit proposed by Dopita et al. (2000) (see Figure 5 on their work), thus, within the uncertainties, HCG 31 seems to be ionized by star formation. In agreement with our results, Alfaro-Cuello et al. (2015) shown a WHAN diagnostic diagram (Cid Fernandes et al. 2010) for the central region of the A+C complex, finding that the system is fully photo-ionized by star formation, even knot A. However, inspecting their diagram (Figure 8 on their work) we find that all the points have $log[N_{II}]/H\alpha < -0.5$, which is consistent with our results. These authors could not find a different behaviour on knot A because the diagram they used could not distinguish between star formation and shocks, or composite ionization.

5.9 The Mass-Metallicity relation of HCG 31

It is well established that there is a correlation between the stellar mass of galaxies and their gas-phase metallicities (e.g. Tremonti et al. 2004, Yates et al. 2020). This correlation, known as Mass-Metallicity relation (MZR), has been widely used to study the formation and evolution of galaxies. Weilbacher et al. (2003) shown that the TDGs does not follow the MZR, thus, plotting this relation for the members of HCG 31 and inspecting the positions of the different objects could give us clues about the formation of them. Indeed, several works studied the luminosity-metallicity relation of HCG 31 in order to discriminate among primordial and tidal dwarf galaxies on this group. For instance, Richer et al. (2003) and López-Sánchez et al. (2004) studied the $M_B vs12 + log(O/H)$ relation for this group and Mendes de Oliveira et al. (2006) studied the $M_K vs12 + log(O/H)$ relation. In the case of the $M_B vs12 + log(O/H)$ relation. It suggests that members A, B, C and G are very luminous for their respective metallicity. This could be explained considering that the magnitude on the B-band filter is probably contaminated by the luminosity from the star formation processes in the system (López-Sánchez et al. 2004). On the other hand, the $M_K vs12 + log(O/H)$ relation suggests that members F1, F2, E2, A1, H and R are TDGs or tidal debris (Mendes de Oliveira et al. 2006).

In order to plot the MZR for HCG 31, it is necessary to define a criterion to separate the galaxies to obtain their integrated spectra. To do this, we simulate a R-band image of HCG 31 collapsing the datacube in the range 5284-7414 Å. The obtained image was smoothed with a beam of 1 arcsec and we run SExtractor to obtain the segmentations from which we will obtain the integrated spectra of the objects. The segmentations uses are shown in figure 5.24 We obtain 9 different objects; A1, A2, A3, A, A+C, B, E, F1 and F2. We run FADO on each spectra, allowing us to obtain the stellar mass of each galaxy, whose values are listed in column (5) in Table 5.7. To compare, we include other mass estimations derived by previous studies. On column (6) we show the masses obtained by López-Sánchez & Esteban (2010) for the different members of HCG 31. In column (7) we list stellar masses derived from the K-band magnitudes published by Mendes de Oliveira et al. (2006). In this case we assume a mass-to-light ratio for each member, based on their g'-r' colors (see Bell et al. 2003), and assuming a solar $M_K = 5.08$ [mag] Willmer (2018).

Object	$12 + \log(O/H)$			\log Mass $[M_{\odot}]$		
	N2 + O3N2	HII-CHI-Mistry	ERM	FADO	LS10	M06
A1	8.34 ± 0.22	8.52 ± 0.05	•••	6.94		8.63
A2	8.39 ± 0.21	8.55 ± 0.04	•••	8.05		
A3	8.30 ± 0.21	8.52 ± 0.04	•••	7.18		
A	8.35 ± 0.21	8.55 ± 0.02	•••	8.73		
A+C	8.25 ± 0.21	8.31 ± 0.02	8.43 ± 0.19	8.61	9.05	9.49
В	8.31 ± 0.21	8.45 ± 0.02	8.30 ± 0.18	8.65	8.90	9.28
\mathbf{E}	8.23 ± 0.21	8.42 ± 0.04	•••	7.37	7.67	8.03
F1	8.06 ± 0.21	8.17 ± 0.04	8.20 ± 0.19	6.85		7.86
F2	8.10 ± 0.21	8.12 ± 0.09	8.19 ± 0.19	5.97		7.35
F (F1 + F2)	8.08 ± 0.21	8.15 ± 0.07	8.20 ± 0.19	6.90	7.59	7.98

Table 5.7: Different masses and metallicities determinations for the members of HCG 31;Col (1) ID of the object. Col (2) Mass determination performed by FADO. Column (3) mass determined by López-Sánchez & Esteban (2010). (4) Adopted mass obtained from the K-band luminosities taken from Mendes de Oliveira et al. (2006). Column (5) Oxygen abundance obtained through an average between methods N2 and O3N2. Column (6) Oxygen abundance obtained using HII-CHI-Mistry and Column (7) Oxygen abundance obtained using the ERM method.

Metallicities were based on three different methods: i) the "direct method", ii) HII-CHI-Mistry and iii) an average between N2 and O3N2 empirical calibrators. Results are listed in columns (2), (3) and (4) of Table 5.7, respectively.

As a control sample we use the MZR derived by Lee et al. (2006), which estimate masses and metallicities for 27 nearby dwarf galaxies. This relation is shown by black points in the three panels of Figure 5.25. It should be noted that the metallicities considered on this control samples were obtained through the direct method (Lee et al. 2003).

In Figures 5.25a, 5.25b, 5.25c, we present the MZRs of HCG 31 for the "direct method", average between N2 and O3N2 and HII-CHI-Mistry respectively. In the three relations we see that galaxies A, B and the A+C complex follows the main MZR, which is expected for this kind of galaxies (Mendes de Oliveira et al. 2006). Other objects seems to be out of the main trend shown in Figure 5.25b and 5.25c, which is expected considering the scenario on which all these objects were formed in the tidal tails, after the first gravitational encounter in HCG 31 (Amram et al. 2004, Amram et al. 2007).

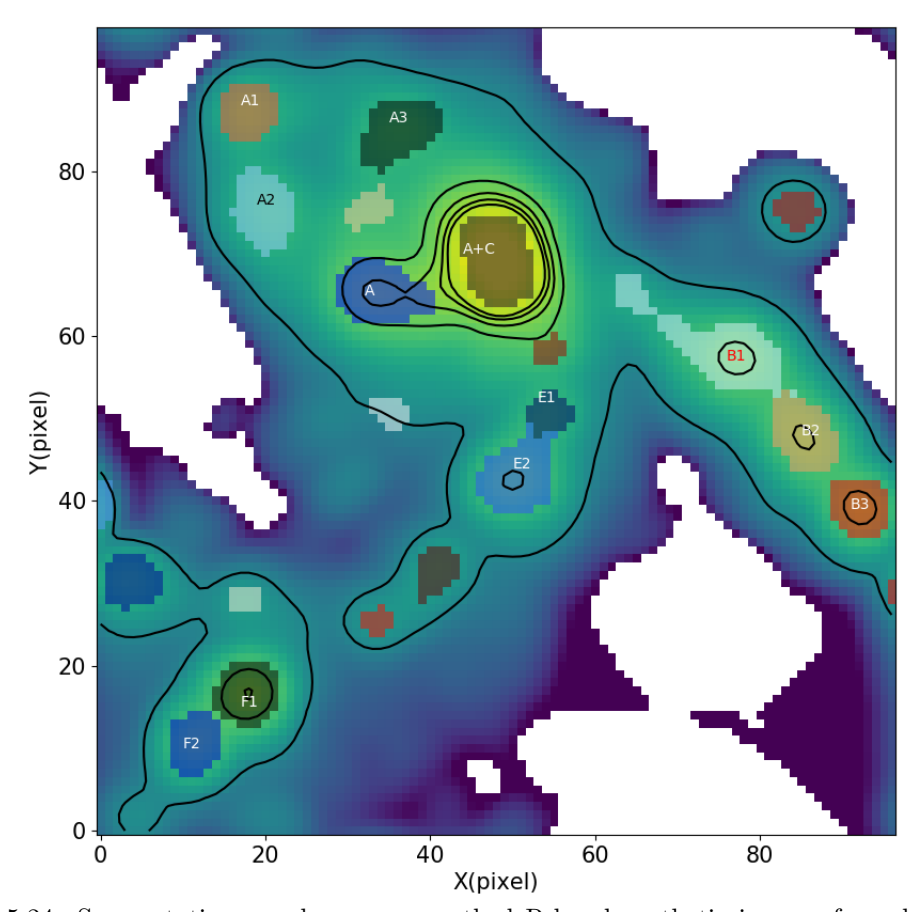


Figure 5.24: Segmentations used over a smoothed R-band synthetic image. for galaxy B we integrate the spectra of segmentations B1, B2 and B3. For Galaxy E we integrate segmentations E1 and E2. The color scale is to show the differences between each segmentation. The black contours represent the smoothed $H\alpha$ emission.

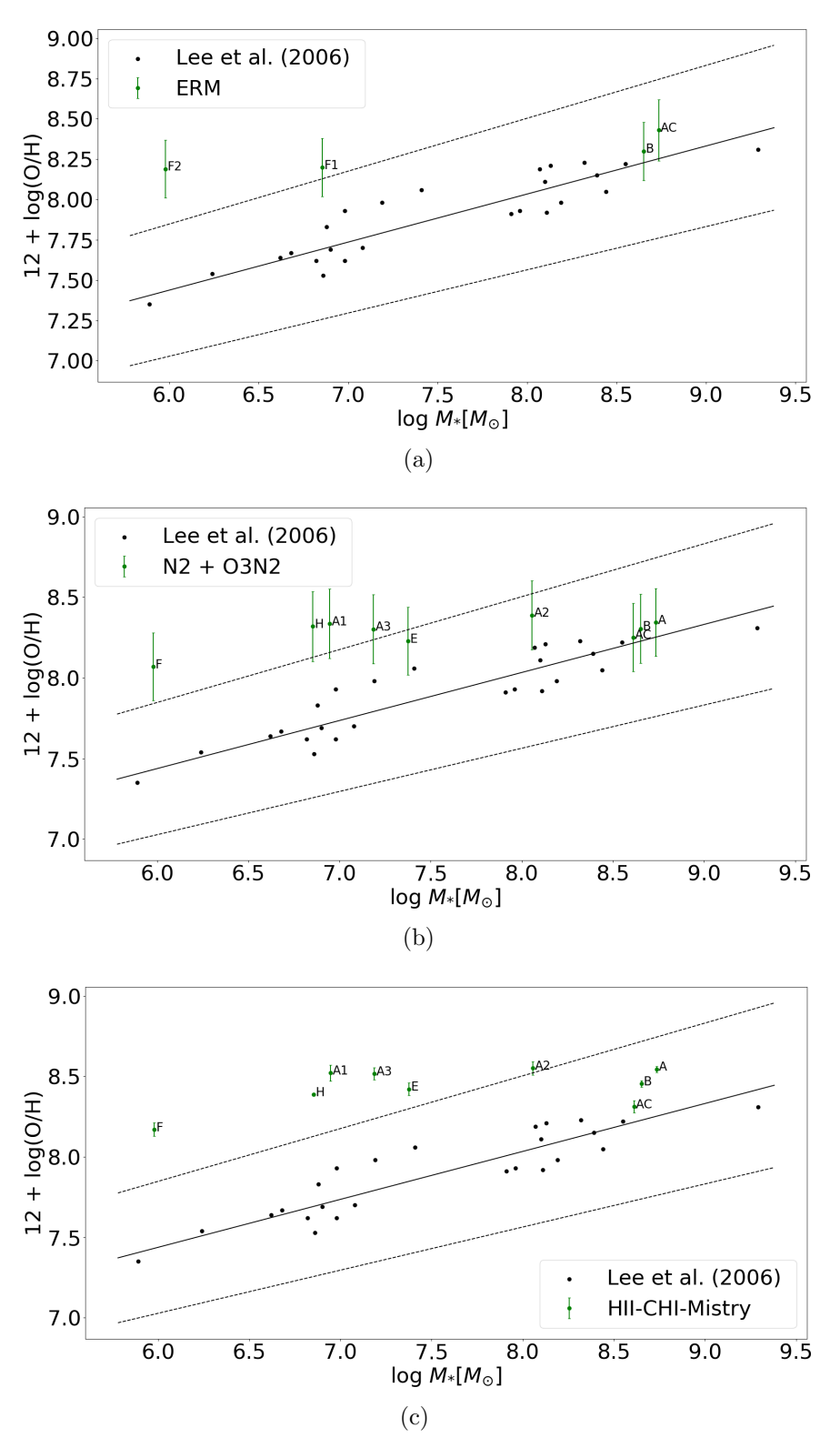


Figure 5.25: MZR relation derived for HCG 31 (green points in three panels). To compare, we present the MZR of nearby dwarf galaxies derived by Lee et al. (2006) as black points in the three panels. The masses considered were calculated by FADO. In (a) is shown the MZR obtained using the ERM Method. In (b) and average between N2 and O3N2 and (c) with HII-CHI-Mistry.

Chapter 6

Discussion

6.1 Are we discovering more super star clusters in HCG 31?

Using GMOS-IFU data, Alfaro-Cuello et al. (2015) report the presence of a central SSC located at ~ 270 pc from the most luminous knot in HCG 31 C. These authors proposed a scenario on which the star formation (associated with the most luminous knot) is triggered at the center of HCG 31 A+C, due to a SSC. This was based on the velocity dispersion, ages, and the continuum emission map. In our data we detect the same behavior at the location of this SSC, confirming their conclusion. However, our larger spatial coverage allow us to extend their results and look for others SSCs in other locations of the group that could be triggering star formation at their neighborhood. In order to confirm our findings, we will use the results obtained by Gallagher et al. (2010) which use deep HST imaging to detect SSCs and star-forming complexes in HCG 31.

We note that a offset between the H α emission and the continuum emission (Figure 6.1) is the first evidence that we must find. By performing this comparison, we find five main offsets, four located at A+C and the other in E2 (see figure 6.1). Offset 4 is the same that was reported by Alfaro-Cuello et al. (2015). Offsets 1 and 2 correspond to the star-forming complexes 2 and 4, previously detected by Gallagher et al. (2010) (see figure 4 and table 2 of their work). Offset 5 correspond to the complex 2, located in galaxy E (see Gallagher et al. 2010) and offset 3 does not appear as a star-forming complex, instead, it corresponds to an SSC. Hereafter we will refer to the offsets as candidates.

We find that candidate 1 has $9\pm 1Myr$, considering Z = 0.004. There are 3 star forming regions near to this candidate (knots 2, 3 and 4 in Figure 5.17), located at ~ 2.2 arcsec (~ 600 pc), ~ 2.6 arcsec (~ 730 pc) and ~ 4.2 arcsec (~ 1.18 kpc), respectively. Considering the age of the bursts, the expansion velocity of an hypothetical shell needed to trigger star formation in the farthest knot is $\sim 232km\ s^{-1}$, which is very high for an expanding shell. Moreover, according to the models of Walborn & Parker (1992), an expanding shell should reach distances of the order of hundreds of parsec in a low density medium, thus, is unlikely that stellar winds coming from candidate 1 can trigger star formation, at least in the knot 4.

In order to reach the closest knot, the expanding velocity should be $\sim 120 \ km \ s^{-1}$, which is quite high, and a typical velocity for shocks (Rich et al. 2015), but, inspecting the BPT diagram for A3 we did not find evidence of shocks. Therefore, the scenario on which candidate 1 could be triggering star formation in its surroundings seems unlikely. This is because we should expect larger velocity dispersion in its surroundings than the observed values ($\sigma_v < 30 \ km \ s^{-1}$). Therefore, this candidate corresponds to an SSC having a recent burst of star formation ($\sim 9 \ Myr$).

Candidate 2 lies in the A+C complex, at a distance of ~ 5.8 arcsec (~ 1.6 kpc) to the NE of the main H α knot in HCG 31C, and shows an age of ~ 6 Myr assuming a metallicity of Z = 0.004. There is no other luminous H α knot in the vicinity of this candidate, and the scenario of candidate 2 triggering star formation in knot C is unlikely, because the distance between them is quite high for an expanding shell.

Candidate 3 is an interesting object. It lies in the A+C complex at ~ 3.5 arcsec (~ 1 kpc) to the north of knot C and it shows an age of ~ 6 Myr (assuming Z = 0.004). It is unlikely that this object is triggering star formation in knot C, due to the same argument for candidate 2. However, this candidate is surrounded by strong H α emission, having ages of ~ 5 Myr. This object is in the central starburst of the system and probably is triggering star formation to their proximity. Moreover, the velocity dispersion of this candidate seems to be high ($\sigma_v \sim 60 \ km \ s^{-1}$), which is expected in such scenario. A detailed kinematic analysis on this source can provide insights on its actual status.

Candidate 4 corresponds to the SSC reported by Alfaro-Cuello et al. (2015). It is very close to knot C (~ 1 arcsec ~ 280 pc) and shows an age of ~ 6 Myr (Z =

0.004). Considering the age of knot C (~ 4 Myr), the expansion velocity needed by an expanding shell should be $\sim 60 km~s^{-1}$ which is consistent with the velocity dispersion detected for this zone. Also, this candidate shows the behaviour of an expanding shell in the σ vs intensity plot (Mu oz-Tu ón et al. 1996).

Candidate 5 lies in the galaxy E and it corresponds to an SF complex, according to Gallagher et al. (2010). Indeed, this is consistent with our detection of an H α knot in the same location as this candidate (knot 23 in Figure 5.17). This candidate is also close to another H α knot (knot 23), which is at \sim 2 arcsec (\sim 550 pc) from it. We derive an age of \sim 9 Myr and \sim 5 Myr for the candidate and the nearest burst, respectively, which give us an expansion velocity of \sim 100 km s⁻¹. This value is lower than the velocity dispersion detected for this candidate ($\sigma_v < 50 \ km \ s^{-1}$). However, we cannot discard the scenario of an old shell in at this location. A detailed kinematic analysis should give us more clues about the kinematic nature of this object.

In summary, we search for SSCs that are triggering star formation in its neighborhood. We define several conditions in order to determine if these SSCs are triggering SF. We find five main offsets between the H α and continuum emission and one of these offsets correspond to the SSC reported by Alfaro-Cuello et al. (2015). We analyze each one of the four offsets and we find that the expansion velocity needed by an hypothetical shell to trigger star formation at their surroundings should be higher than the velocity dispersion detected by our σ_v map. We need more detailed kinematics to analyse if these candidates corresponds to old shells in expansion.

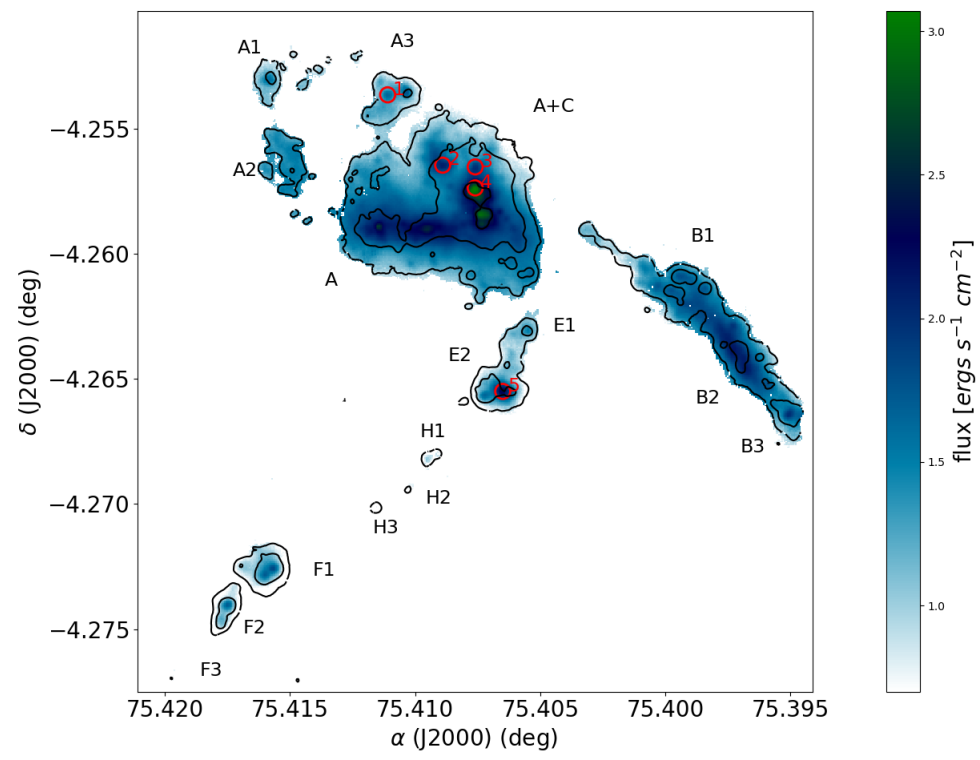


Figure 6.1: Continuum emission map of HCG 31. The black contours represent the H α emission, the red circles show the locations of the principal offsets between continuum and emission peaks.

6.2 A peculiar knot in HCG 31 A

An interesting region located in the central A+C complex is the brightest H α knot. This knot is usually referred as the nucleus of the galaxy HCG 31 A (e.g Torres-Flores et al. 2015) and it shows several interesting properties: i) it is the only region in the entire A+C complex that seems to be ionized not only by star-formation, ii) it shows the higher electron density and H α emission within the entire group (Alfaro-Cuello et al. 2015) and iii) it shows the higher metallicity of the system.

Normally, in HII regions having high H α luminosities one may expect to find low metallicities, because the starburst probably are fuelled by the infall of metalpoor gas (Sánchez-Almeida et al. 2014). However, we detect a quite high oxygen abundance for this region of $12 + log(O/H) = 8.56 \pm 0.19$, on average. According to Oey & Kennicutt (1993), systematic variations in the nebular density can lead to differences in the metallicities up to 0.5 dex. This effect cannot be discarded for this knot, because it shows the higher electron density in the entire system

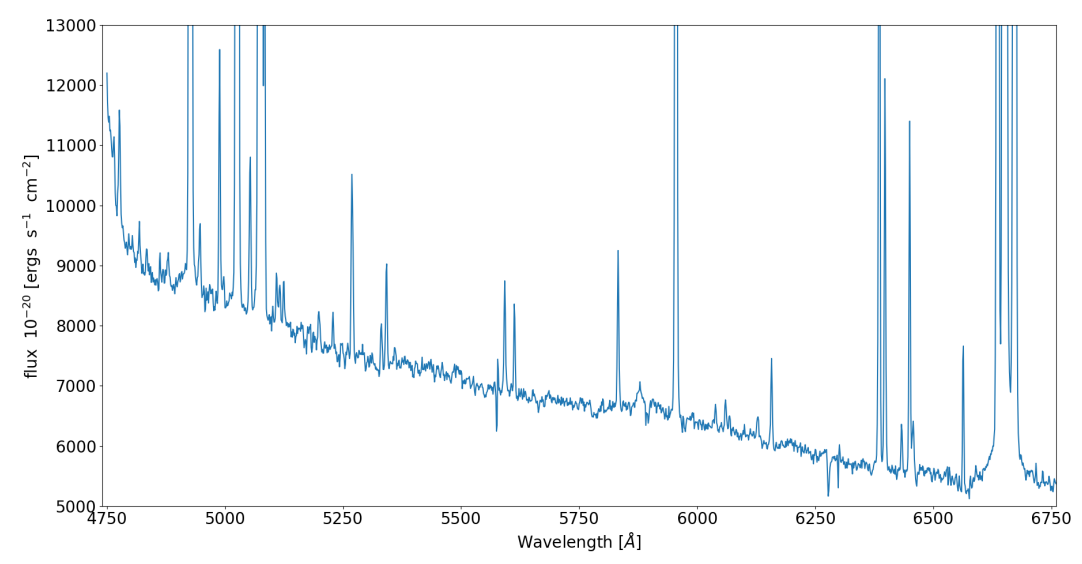


Figure 6.2: Zoom into the integrated spectra of a 1"x1" box centered at the knot A, it is seen that the spectrum shows WR features, a weak red bump and an intense blue bump.

with $n_e \sim 300 \text{ cm}^{-3}$.

This knot is also the region with the highest nitrogen and helium abundance of the system. On this context, it is well known that WR stars can contribute to enrich the ISM with N and He (Pérez-Montero et al. 2013, Kehrig et al. 2013). In order to confirm the existence of such stars we integrate the spectra over a box of 1" ×" centered at knot A. The resulting spectra is presented in Figure 6.2. The red bump seems to be quite weak. An intense blue bump can be inferred from the image which is related with the existence of a larger contribution of WN stars. Probably these WN stars are those that locally enriched the medium in N and He. Furthermore, Krabbe et al. (2014) propose that the stellar winds and mass loss of WR stars are the cause of one of the denser and metal-rich HII regions of their sample, a very similar scenario than the case of this knot.

The velocity dispersion on this knot is in the order of ~ 55 km s⁻¹, which seems to be quite high for star formation but still low to be explained by shocks. In this context, this velocity could be expected considering the location of this knot in the BPT diagram, which lies in the composite zone. However, as for the whole A+C complex, our estimations of the velocity dispersion are biased because the widening of multiple components that cannot be resolved with our spectral resolution, therefore, we cannot rule out the presence of shocks.

6.3 About the TDG nature of member F

One of the most frequent questions about this system in the literature concerns about the nature of object F. In optical images it appears like a bright tidal object located in the southern tail of the system. The photometry of this object was quite uncertain because the contamination of a nearby projected star. In addition, Hunsberger et al. (1996) does not consider the F galaxy as an TDG candidate although they considered other five objects like candidates (E1, E2, A1, A2 and A3). Probably they do not obtain a good photometry of member F and discard it from the analysis. Using H α imaging, Iglesias-Páramo & Vílchez (2001) propose that objects F1, F2 and F3 are the most likely TDGs candidates in HCG 31, based on their H α luminosities (> 10^{39} ergs s⁻¹) and their large projected distances to the parent galaxy.

TDG candidates needs to fulfill two main conditions (based on Weilbacher et al. 2003): i) it is quite metallic for its mass (out of the MZR) and ii) it is kinematically decoupled from the tail showing their independent kinematics. To accomplish the first condition, many works studied the luminosity-metallicity relation for HCG 31 in filters B and K (Richer et al. 2003, López-Sánchez et al. 2004, Mendes de Oliveira et al. 2006). In all these works, objects F1 and F2 show high metallicities for their luminosities. Furthermore, in section 5.9 we note that F1 and F2 seem to be out of the main MZR of dwarf galaxies. Hence it is well established that object F has a tidal rather than a primordial origin.

The H α kinematics of member F is quite peculiar, because its shows no rotation in any axis (Amram et al. 2007). Our radial velocity map presented in section 5.1 confirm that result. The HI kinematics of F (Verdes-Montenegro et al. 2005) shows that object F is kinematically decoupled from the tail, with a rotation axis that is perpendicular to the axis of the tail, suggesting that this object is already decoupled from the tail. Amram et al. (2007) propose that this object is accreting material from the tail. Nevertheless, that scenario is difficult to prove and simulations are needed to confirm it. On this thesis we detect high SFRs and high EW(H α) (young ages) in member F, which is completely consistent with this scenario.

In summary, the true nature about object F is not fully understood yet. We confirm its tidal origin using the MZR relation and it is very likely that the object is already decoupled from the tail based on its HI kinematics.

6.4 Abundance gradients

The metallicity distribution in spiral galaxies has been studied by several authors (e.g., van Zee et al. 1998 Bresolin et al. 2012, Sánchez et al. 2014), who find that most of these galaxies show a clear abundance gradient, with the center of the galaxy being more metallic than the outskirts. On the other hand, several observational studies have proven that interacting galaxies show flatter abundance gradients than isolated galaxies (Kewley et al. 2010, Torres-Flores et al. 2014, Olave-Rojas et al. 2015). Numerical simulations shows that this flattening in the gradients are mainly due to gas inflows towards the nuclear zones, which are mainly triggered by gravitational encounters and mergers (Torrey et al. 2012). In addition, observational studies have shown that dwarf galaxies present small, or no abundance gradients (Roy et al. 1996, Hunter & Hoffman 1999, Croxall et al. 2009, Izotov et al. 2006). Pilyugin et al. (2015) find that dwarf irregular galaxies can present an abundance gradient depending on their surface brightness profile, breaking the "spiral vs dwarf dichotomy" (which says that spiral galaxies display clear abundance gradient whereas dwarf irregular galaxies do not). More recently, James et al. (2020) use MUSE observations of the dwarf galaxy JKB 18 to find that it have an inhomogeneous chemical distribution, bringing more evidence to the fact that not all dwarf irregular galaxies are chemically homogeneous.

In this thesis we present detailed metallicity maps of the system HCG 31, derived with the Empirical relation method and with several strong-line empirical calibrators. The excellent spatial resolution provided by MUSE allow us to derive the metallicity gradient for galaxy B, the southern tidal tail and for the central zone of the system. In the case of galaxy B, we detect an almost flat metallicity distribution with a slope of $\alpha = -0.012 \pm 0.002$ dex kpc⁻¹ (N2 calibrator) which tell us about the chemical homogeneity of this system, with no significant variations in its metallicity. This finding is expected for a merging galaxy (Rupke et al. 2010b). An interesting feature in the gradient of this galaxy is the central drop in metallicity at ~ 5 arcsec. This kind of drops seem to be similar to those detected by Sánchez et al. (2014) in several galaxies of their sample. However, these authors find no correlation between these drops and interaction features in the galaxies. Here we propose three different scenarios to explain this central drop in metallicity:

Amram et al. (2007) found that the receding and approaching sides of the

rotation curve of this galaxy does not match. The most prominent disagreement in the rotation curve lies at the inner 5 arcsec. Amram et al. (2007) indicate that this inner disagreement may be the sign of a bar. Probably this bar is inducing radial motions of gas which are flattening the central metallicities. However, it should be noted that there is no correlation between the presence of a bar and the central drop in metallicity (Sánchez et al. 2014).

Other possibility is that the galaxy is currently accreting metal-poor gas, which is inducing the starburst producing the central drop in metallicity. This scenario is more unlikely because a galaxy that is accreting material shows a drop in metallicity of the order of \sim - 0.5 dex (Sánchez-Almeida et al. 2014), and the central drop that we detect is < -0.2 dex regardless of the method used.

Finally, another possibility could indicate that the galaxy hosts a central starforming ring which is an evidence of radial gas flows induced by resonance processes. This is the scenario that Sánchez et al. (2014) used to explain the central drop in the galaxies of their sample. However, they did not find evidence of signs of interaction or bars on these galaxies. In our case, galaxy B presents both signs, thus, we can speculate that a mixture between the presence of a bar and gas accretion are the responsible of the presence of the central metallicity drop in this galaxy.

An alternative explanation, could be that the drop is artificial and just a random effect of the strong line methods used. Indeed, if we consider the 0.16 dex uncertainties of the strong-line methods the drop "dissapear". We used three different methods to plot the gradient (N2, O3N2 and HII-CHI-Mistry) and with the three methods we observe the same behaviour, which supports the fact that the drop observed is real. A determination of the metallicity gradient of galaxy B with the ERM method is required to double check the presence of this central drop.

For the southern tidal tail we also detect a flat metallicity distribution with a slope of $\beta = -0.012 \pm 0.001$ dex kpc⁻¹ (N2 calibrator) and $\beta = -0.007 \pm 0.001$ (O3N2 calibrator) dex kpc⁻¹. Member F seems to be slightly less metallic than members E and H, which could be a consequence of the current metal-poor gas accretion. Several works have studied the metallicity gradients of tidal tails (e.g Chien et al. 2007 Torres-Flores et al. 2014, Olave-Rojas et al. 2015) and their results suggests that the tidal tails shows flat metallicity gradients. A similar behaviour is found for larger radii (R > R₂₅) in normal disk galaxies (Sánchez

et al. (2014)). However, we did not find in the literature a metallicity gradient determination in a system similar to HCG 31 (compact group of dwarf galaxies), thus, we can compare our gradient only with gradients of tails in more massive systems. The origin of this flat behaviour is generally attributed to streaming motions inside the tail that redistribute the gas. If this is the case, one may expect to find a velocity gradient along the tail, which is exactly what we find for this tail. An increasing velocity is observed from object E to H. But in object F we not detect the same gradient, indeed, we observe a flat velocity gradient for this galaxy, which indicates counter rotation with respect to the tail (Verdes-Montenegro et al. 2005, Amram et al. 2007).

Finally, in order to confirm the result obtained by Torres-Flores et al. (2015), we determined the metallicity variation between the two more intense H α knots in the A+C complex. We did not detect a significant metallicity gradient between them, and our determinations using the ERM method shows a uncertainty quite high (~ 0.18 dex) which is insufficient to verify the smooth metallicity variation between the knots reported by Torres-Flores et al. (2015).

6.5 The star-formation history of HCG 31

The history of this system haven been studied by several authors (Rubin et al. 1990, Iglesias-Paramo & Vilchez 1997, Johnson et al. 1999, López-Sánchez et al. 2004, Gallagher et al. 2010). We consider that our new spectroscopic information of the system can bring more evidence to unveil the star-formation history of this group.

In order to have a good determination of the stellar populations in HCG1 we run FADO over the integrated spectra of each galaxy. In Figure 6.3 is represented the luminosity fraction at the normalization wavelength (5100 \mathring{A}) for each of the SSPs fitted, which is a schematic illustration of the star-formation history of each galaxy. We show the SFHs only for the galaxies with the best signal-to-noise in the continuum (A+C, A, and B). Also, we include the SFH of the galaxy F1. We caution the reader that the continuum emission for this galaxy is very weak.

The SFH of the A+C complex reveals that the peak of star formation occurred $\sim 10^7 - 8$ yr ago. If we associate this SF peak with the first encounter between the galaxies, we find that this age is consistent with the 400 Myr of the first encounter reported by Johnson et al. (1999). In addition, the system is experiencing another

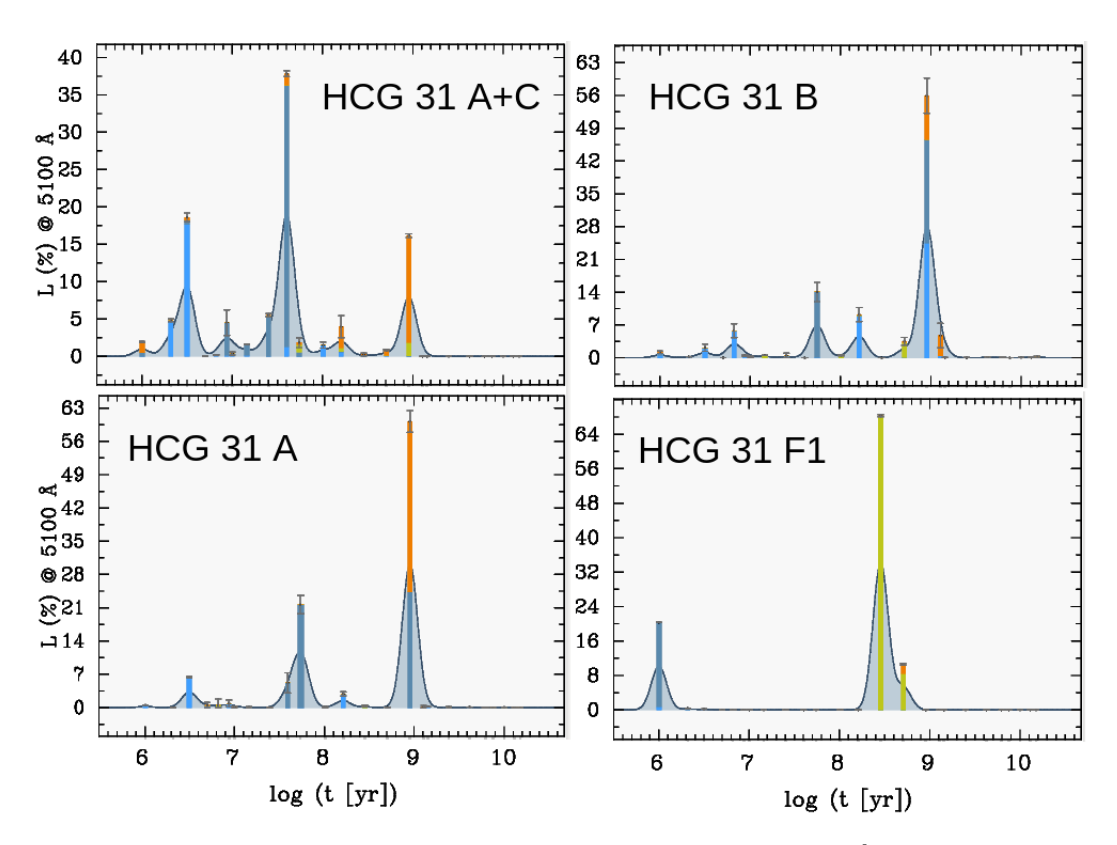


Figure 6.3: Luminosity fraction at the normalization wavelength (5100 Å) as a function of the age for the galaxies HCG 31 A+C, HCG31 A, HCG 31 B and HCG 31 F1. The colors light-blue, blue, light-green and orange stand for metallicities of 0.02 Z_{\odot} , 0.2 $_{\odot}$, 0.4 $_{\odot}$ and 1 Z_{\odot} respectively. The shaded area shows an Akima-smoothed (Akima 1970) version of the SSP contributions, giving as a result an illustration of the star formation history of the different galaxies.

starburst event at $\sim 10^{6-7}$ Myr ago, which is completely consistent with the ages of the star forming bursts (this work, Alfaro-Cuello et al. 2015) and with the ages derived using photometry (Iglesias-Paramo & Vilchez 1997, López-Sánchez et al. 2004).

The SFH of galaxy A is very similar to that of the A+C complex, with an important underlying old stellar population of ~ 1 Gyr, another peak at 10^{7-8} yr and the current star-formation event at 10^{6-7} yr ago. It should be noted that the SFH of galaxy A represents only the SFH of the extended body that is seen in the optical images, and it is not a representation of the SFH of the galaxy HCG 31A as whole, indeed, it is not possible to completely separate both galaxies (A+C) because they are probably overlapping each other (Amram et al. 2007).

For galaxy F1 we find a very interesting behaviour on its SFH, with only two

peaks of star formation, at $\sim 10^{8-9}$ yr and $\sim 10^6$ yr. We did not find evidence of a very old stellar population with ages larger than > 1 Gyr, thus, our results are in very good agreement with the ages of the SSCs found by Gallagher et al. (2010), who found no evidence of an old population. However, as mentioned above, this result should be taken with care, because the continuum emission of galaxy F is very weak, and therefore our determination of the stellar populations are not precise.

In summary, all the galaxies of the group display an underlying stellar population of ~ 1 Gyr and are currently forming stars. The first encounter between HCG 31A and HCG 31C occurs ~ 100 Myr ago. Galaxy F1 has a bimodal distribution of ages, with intermediate and young stellar populations.

6.6 Disentangling the Hickson Compact Group HCG 31

This group has been studied by several authors, in different wavelengths, with different techniques (e.g Iglesias-Paramo & Vilchez 1997, Johnson et al. 1999, Gallagher et al. 2010, Rubin et al. 1990, López-Sánchez et al. 2004, Mendes de Oliveira et al. 2006, Amram et al. 2007, Alfaro-Cuello et al. 2015). On this thesis we present a considerable improvement in terms of spatial resolution and spectral and spatial coverage. The FoV analyzed on this work allow us to study 9 objects of this group (A1, A2, A3, A, A+C, B, E, H and F). Here we are going to review the main properties and physical parameters of each object.

6.6.1 The northern tidal tail: Objects A1, A2 and A3

This tail was detected in HI images of HCG 31 (see Williams et al. 1991, Verdes-Montenegro et al. 2005), and connect the central merger with the galaxy HCG 31 Q (not visible in our FoV). There is no obvious optical counterpart for this tail, and objects A1, A2 and A3 are located in the southern part of it. These three objects are formed from material that was expelled from galaxy A during the interaction with member C (Amram et al. 2007).

Object A1 is located at the NE of this tail and shows a rounded shape in continuum and $H\alpha$ images. Its kinematics show no rotation and a low velocity

dispersion. This object is not kinematically detached from the main rotation pattern of the central merger, suggesting that it continues being part of it. This object is out of the M_B vs metallicity relation (López-Sánchez et al. 2004) and of the M_K vs metallicity relation (Mendes de Oliveira et al. 2006). Considering this fact, in addition with its proximity to the central merger (\sim 6 kpc), this object will be falling back to the main merger, which is the scenario proposed by Amram et al. (2007). This object also hosts the most intense H α knot in the northern tidal tail, which corresponds to an star-formation complex which was also detected by Gallagher et al. (2010), and for which we estimate an age of 5-6 Myr.

At the west of A1 we find several objects with an extension of ~ 2 arcsec each, which correspond to tidal debris of the northern tidal tail, with little star-formation and mass, but with a metallicity similar to that of A1 and the central merger. Kinematically these objects follows the main trend and probably they are going to fall back on the central system as the other members of this tail.

Object A2 is located at the south of A1, closer to the central merger. This object shows a slightly more elongated shape that A1 and it shows its own kinematic pattern, with a low amplitude on its rotation curve of $\sim 25 \; \mathrm{km \ s^{-1}}$ (Amram et al. 2007), which is also observed in our radial velocity map. This motion is from north-to-south which is in counter-rotation with respect to the main rotation pattern of the system, which suggests that this object will fall back into the central merger.

The location of A2 in the MZR is very interesting, because this object is the most massive in the northern tidal tail and seems to be close to the main trend of dwarf galaxies, however, as mention before, its proximity to the central merger and low mass indicate that this object is probably falling back into A+C, thus, is unlikely the scenario of this object being a normal dwarf galaxy. We detect two H α knots in this object which corresponds to HII regions. We do not find a peak of continuum emission near to these knots, or an offset between continuum and H α emission. We cannot confirm with HST imaging if there are a SSC in this object because it is out of the FoV. Regarding ages, this object is slightly older than other objects in this tail, with ages ranging 6-9 Myr.

Object A3 is located at the north of the A+C complex, with a triangular shape and with $H\alpha$ knots at their vertices. This object seems to be "connected" with the central complex (in the continuum image a little bridge at the south of A3 can be seen connecting this object with A+C). At the center of this object

a continuum peak, non-correlated with the H α emission, is observed. According to Gallagher et al. (2010) this peak corresponds to a star-formation complex, but we do not detect a concentration of H α emission at its location. We investigate the possibility of this continuum source could be triggering star formation in the outer knots, but we find that this is unlikely because the velocity expansion of the hypothetical expanding shell should be higher than the velocity dispersion detected. We propose that it corresponds to an SSC with its last starburst \sim 9 Myr ago. Kinetically this object follows the main rotation pattern of HCG 31 A+C and shows low velocity dispersion.

The metallicity of A3, as for A1 and A2, seems to be very similar to the metallicity of the central merger, and its location in the MZR is out of the main trend. This objects is thus a tidal debris that is going to fall back into HCG 31 A+C, together with A1 and A2.

6.6.2 The central merger: The A+C complex

Galaxies HCG 31A and HCG 31C together makes up the central complex HCG 31 A+C (or NGC 1741). This complex has been studied by several authors and there are two different origin scenarios in the literature, i) the complex is a single interacting galaxy (Richer et al. 2003) and ii) the complex consists in a pair of interacting dwarf galaxies (Rubin et al. 1990, López-Sánchez et al. 2004, Amram et al. 2007, Alfaro-Cuello et al. 2015). The evidences for the last scenario are more robust and supported by kinematic and physical criteria.

In the continuum emission images this complex seems to be clumpy, because the different stellar clusters that lies on it that were reported in different studies (Johnson et al. 1999, Gallagher et al. 2010) and a bar-like structure that extends to the east. The latter structure correspond to the main body of the galaxy HCG 31A. The galaxy HCG 31 C lies in the north of the central continuum peak. The exact limit between these two galaxies is difficult to determine because i) projection effects and ii) probably does not even exist because the ongoing merger.

Verdes-Montenegro et al. (2005) found that the HI disks of the two galaxies still is surviving, with different velocity ranges for each one. Such a division could not be done in the case of the H α kinematics (Amram et al. 2007), despite their high spectral resolution, which is an evidence of the advanced stage of merger between those galaxies.

The radial velocity map derived for this group is in quite good agreement with the velocity map presented in Amram et al. (2007). One of the most noticeable features on the map is that the A+C complex shows a rotating pattern that could lead to misunderstandings about the kinematic nature of the complex. Using Fabry-Perot datacubes, Richer et al. (2003) concluded that the A+C complex consists in a single kinematic entity, but their conclusion was biased by their lower spatial resolution. Even though the velocity map shows a rotation pattern, it is not present the classical solid-body rotation fingerprint and it is clearly a perturbed velocity map which is a solid evidence of the merger event.

For this complex we derive the main physical parameters. We find that the electron density is low over the entire system, excepts for a peak located at the nucleus of the galaxy HCG 31A (knot A). This peak in density can be explained by a inflow of gas between the nucleus of galaxy HCG 31C (Torres-Flores et al. 2015). However, we did not find clear evidence of a metallicity gradient between these two knots. On the other hand, the distribution of the electron temperature seems to be quite homogeneous, and our values are in quite good agreement with previous determinations.

The metallicity map of this complex shows a homogeneous distribution. We find a mean oxygen abundance of $12+log(O/H)\sim 8.37$, by using the ERM method. We also derive abundances of He, N, Ar and S and we find that the distribution is also homogeneous for these elements. We find that the main body of HCG 31A and HCG 31A+C follows the standard MZR for dwarf galaxies.

We determine, for the first time for this system, a map of the Wolf-Rayet population, estimating a total number of $N_{WCE} = 492 \pm 75$, which is higher than previous determinations, and none of them have determined it using spatially resolved data. It should be noted that our spectral resolution allow us to map only the WR red bump, which is associated with WC stars which are less numerous than WN stars (Guseva et al. 2000), thus, our map not represent the total WR population of the galaxy.

The map of the ionization mechanism shows that almost the entire complex is mainly ionized by massive stars, excepting a knot located in the nucleus of HCG 31A which shows composite ionization. We detect also some points with LINER/AGN line ratios. All these points are located in the outskirts of the galaxy and probably are dominated by shocks or some diffuse ionized gas (DIG).

We verify the previous determinations of the SFR of this system, finding a total

SFR of $10.99 \text{ M}_{\odot} \text{ yr}^{-1}$ for the central A+C complex, which is in good agreement with previous determinations. Clearly this central complex is in a starburst phase, probably triggered by the merger between the galaxies A and C.

The SFH of the system shows that there are three principal populations: i) an "old" population with an age of ~ 1 Gyr, ii) an "intermediate" with ages of ~ 100 Myr (which is a consequence of the starburst triggered by the first encounter), iii) and a young population which is being formed by the current starburst. We find that our ages are in good agreement with the ages derived by previous works using HST photometry (Johnson et al. 1999, Gallagher et al. 2010).

We detect 3 main continuum-emission peaks that are no-correlated with H α emission and we investigate the possibility that these peaks were triggering star formation in their surroundings. However, we did not find evidence of a second star formation episode triggered by those SSCs, except for one which was previously reported by Alfaro-Cuello et al. (2015). In any case, a more detailed kinematic analysis centered on these sources is needed in order to verify if the peaks presents the behaviour of an expanding shell.

In summary, the A+C complex consists in a pair of dwarf galaxies in an ongoing merger that are passing through a starburst. A scenario similar to NGC 1487 (e.g Buzzo et al. 2021).

6.6.3 A close companion: Galaxy B

The morphological type of this galaxy is SB(s)m pec edge-on (de Vaucouleurs et al. 1991). It lies very close to the main merger and a H α bridge connects them (Iglesias-Paramo & Vilchez 1997). On this thesis, we obtain spatially resolved maps of different physical properties of this object.

The radial velocity map obtained for this object is very consistent with a rotating galaxy, having a velocity amplitude of $\sim 200~km~s^{-1}$. The velocity dispersion map display low values of $\sigma_v < 30km~s^{-1}$. All the kinematic properties obtained are in quite good agreement with those obtained by Amram et al. (2007).

The physical properties measured for this galaxy are consistent with previous works, with low electron densities $n_e < 100~cm^{-3}$ and electron temperatures of the order of $T_e \sim 12000 K$.

We detect for this galaxy, an almost flat metallicty distribution with an average value of $12 + log(O/H) \sim 8.3$, which is very similar to the value found for the

other members of the group. We compare its metallicity gradient with that of other similar galaxies and we find that the behaviors are almost the same. A peculiarity found for the metallicity profile of this galaxy is the metallicity drop detected in the inner parts of the galaxy, however, as mentioned in section 6.4, this central drop could be explained by three different scenarios; i) metal-poor gas accretion of the galaxy at the central zone, ii) A star formation ring which is diluting the central metallicities and iii) the eventual presence of a bar which triggers metal mixing in the inner regions of this galaxy.

We determine a spatially resolved map of the ionization mechanism for this galaxy and we detect that it is mostly dominated by the ionization of massive young stars. A few spaxels are located in a different region of the ionization diagnostic diagram, but these points are located at the outskirts of the galaxy and can be explained by the presence of a DIG, or by the low SNR detected for those points.

Finally, we estimate the SFH for this system using the results of the spectral population synthesis derived by FADO, and we detect that this galaxy hosts an underlying old stellar population.

6.6.4 The southern tidal tail: Objects E, H and F

This tail extends from the core of the galaxy HCG 31C until the galaxy HCG 31F. It shows an HI counterpart (Williams et al. 1991, Verdes-Montenegro et al. 2005) which is aligned with the optical tail. There are 2 main hypothesis about the origin of this tail: i) it is a tail generated by a fly-by interaction with the galaxy HCG 31G (e.g López-Sánchez et al. 2004) and ii) it is generated only by the tidal forces involved in the interaction between HCG 31A and HCG 31C (e.g Amram et al. 2007). On this thesis we did not get information about the galaxy HCG 31G, which for obvious reasons is a key object to fully understand the nature and origin of this tail.

Based in the velocity map and in the metallicity distribution obtained for this tail, we infer that definitively this object was generated from the material of galaxy HCG 31A. The most likely scenario is that it has been generated from the merger of the galaxies HCG 31A and HCG 31 C. Moreover, Amram et al. (2007) propose this scenario and our velocity map is fully consistent with the one presented by them.

We also derive different properties and physical parameters for this tail: i) the main ionization mechanism is star formation in almost all the spaxels, with no significant contribution of shocks, ii) The electron densities are low, with an average $n_e < 100 \ cm^{-3}$, iii) the electron temperatures are close to those of typical HII regions, having $t_e \sim 10^4 K$. These properties are consistent with young HII regions distributed through the extension of the southern tidal tail.

The SFR derived from the $H\alpha$ emission of the different members of this tail presents a peak in the members F1 and F2, which could be an insight of the ongoing accretion process that those galaxies are experiencing.

The star formation history diagram derived for galaxy F1 could be an evidence for the tidal origin of this object. This galaxy presents only two peaks in star formation through its history. The first peak is associated with the old stellar population that were part of the system HCG 31C. The second one is associated with the current episode of star formation.

As a summary, we propose that the interaction between galaxies A and C led to the formation of this tidal tail. And the accretion of gas from the HI envelope triggers the formation of members F1 and F2 which are currently passing through an episode of star formation.

Chapter 7

Summary and Conclusions

On this thesis we perform a deep analysis of the Hickson compact group 31 using IFS data observed with MUSE. We used different maps for analyzing the kinematics, ionization mechanisms, physical properties, chemical abundances, SFRs, ages, among others. Our most remarkable results are:

- The kinematic is consistent with previous works. The group show clear evidence of an ongoing merger process.
- The main ionization mechanism through the whole group is the star formation, with a small contribution of shocks only at the nucleus of galaxy A.
- The physical properties of the different regions on HCG 31 are consistent with previous works and are typical for young star-forming regions
- The oxygen abundance is mainly low and it shows a flat distribution across the different galaxies. This suggests gas mixing through the whole group probably triggered by the merger.
- We do not have the sufficient precision to confirm, or discard the presence of a central gradient of metallicity.
- The star formation rate and ages are consistent with previous works. There are two simultaneous bursts of star formation: In the central zone and Galaxy F.
- There is a prominent Wolf-Rayet population in the central zone of the group. We cannot estimate the population of WN stars.

- The continuum emission seems to be very low. Thus, we cannot perform a precise analysis of the stellar population of each galaxy belonging to the system.
- The Mass-Metallicity relation confirm the tidal origin of objects E, H and F.
- We can only reconstruct the star formation history of the youngest population. The ages obtained are consistent with previous works.

Chapter 8

Future Work

On this thesis we develop a deep study of the Hickson Compact Group 31 using MUSE data. We obtain detailed maps of the kinematic, extinction, physical parameters, chemical abundances, ionization parameters, ages, SFRs, among others interesting features of this spectacular system.

However, there are different ways to enrich this work and obtain more information about HCG 31. Here we list some of them:

- A spatially resolved map of the metallicity but using exclusively the direct method instead of empirical calibrators (e.g using IFU data with spectral coverage covering the [OIII]auroral line). It would be very useful to obtain precise determinations of the gas-phase chemical abundances. This would be very helpful in order to obtain precise determinations of the oxygen abundance and should allow us to compare the values obtained with other galaxies or compact groups in a more robust way.
- A spatially resolved correlation of the physical parameters with the highresolution kinematic data available for this object (Amram et al. 2007) would be very relevant in order to: i) detect expanding shells, ii) compare the chemical abundances gradients with a detailed kinematic analysis of the central zone, galaxy B and in the tidal tail.
- A deep analysis of the stellar emission of the system (e.g using deeper observations) could provide us very important information concerning to the underlying stellar population of this system (e.g kinematics, metallicities and ages)

8 Future Work 114

• A larger study including in the analysis the galaxies Q, R and G, allowing us to obtain a more complete vision of the system and investigate the role of these galaxies in the interaction.

Bibliography

- Alfaro-Cuello, M., Torres-Flores, S., Carrasco, E. R., et al. 2015, Mon. Not. R. Astron. Soc., 453, 1355
- Allende Prieto, C., Lambert, D. L., & Asplund, M. 2001, Astrophys. J. Let., 556, L63
- Allington-Smith, J., Murray, G., Content, R., et al. 2002, Pub. Astron. Soc. Pacific, 114, 892
- Allington-Smith, J. R., Content, R., & Haynes, R. 1998, in Society of Photo-Optical Instrumentation Engineers (SPIE) Conference Series, Vol. 3355, Optical Astronomical Instrumentation, ed. S. D'Odorico, 196–205
- Alloin, D., Collin-Souffrin, S., Joly, M., & Vigroux, L. 1979, Astron. Astrph., 78, 200
- Amram, P., Mendes de Oliveira, C., Plana, H., Balkowski, C., & Hernandez, O. 2007, Astron. Astrph., 471, 753
- Amram, P., Mendes de Oliveira, C., Plana, H., et al. 2004, Astrophys. J. Let., 612, L5
- Bacon, R., Bauer, S.-M., Bower, R., et al. 2004, in Society of Photo-Optical Instrumentation Engineers (SPIE) Conference Series, Vol. 5492, Ground-based Instrumentation for Astronomy, ed. A. F. M. Moorwood & M. Iye, 1145–1149
- Bacon, R., Copin, Y., Monnet, G., et al. 2001, Mon. Not. R. Astron. Soc., 326, 23
- Baldwin, J. A., Phillips, M. M., & Terlevich, R. 1981, Pub. Astron. Soc. Pacific, 93, 5

Bell, E. F., McIntosh, D. H., Katz, N., & Weinberg, M. D. 2003, Astrophys. J. Suppl., 149, 289

- Bellocchi, E., Ascasibar, Y., Galbany, L., et al. 2019, Astron. Astrph., 625, A83
- Bresolin, F., Kennicutt, R. C., & Ryan-Weber, E. 2012, Astrophys. J., 750, 122
- Bresolin, F., Schaerer, D., González Delgado, R. M., & Stasińska, G. 2005, Astron. Astrph., 441, 981
- Bruzual, G. & Charlot, S. 2003, Mon. Not. R. Astron. Soc., 344, 1000
- Bundy, K., Bershady, M. A., Law, D. R., et al. 2015, Astrophys. J., 798, 7
- Buzzo, M. L., Ziegler, B., Amram, P., et al. 2021, Mon. Not. R. Astron. Soc., 503, 106
- Calzetti, D., Armus, L., Bohlin, R. C., et al. 2000, Astrophys. J., 533, 682
- Calzetti, D., Kinney, A. L., & Storchi-Bergmann, T. 1994, Astrophys. J., 429, 582
- Cappellari, M. 2017, Mon. Not. R. Astron. Soc., 466, 798
- Cappellari, M. & Emsellem, E. 2004, Pub. Astron. Soc. Pacific, 116, 138
- Cardelli, J. A., Clayton, G. C., & Mathis, J. S. 1989, Astrophys. J., 345, 245
- Chien, L.-H., Barnes, J. E., Kewley, L. J., & Chambers, K. C. 2007, Astrophys. J. Let., 660, L105
- Cid Fernandes, R., Mateus, A., Sodré, L., Stasińska, G., & Gomes, J. M. 2005, Mon. Not. R. Astron. Soc., 358, 363
- Cid Fernandes, R., Stasińska, G., Schlickmann, M. S., et al. 2010, Mon. Not. R. Astron. Soc., 403, 1036
- Croxall, K. V., van Zee, L., Lee, H., et al. 2009, Astrophys. J., 705, 723
- de Mello, D. F., Urrutia-Viscarra, F., Mendes de Oliveira, C., et al. 2012, Mon. Not. R. Astron. Soc., 426, 2441
- de Vaucouleurs, G., de Vaucouleurs, A., Corwin, Herold G., J., et al. 1991, Third Reference Catalogue of Bright Galaxies

Denicoló, G., Terlevich, R., & Terlevich, E. 2002, Mon. Not. R. Astron. Soc., 330, 69

- Domínguez, A., Siana, B., Henry, A. L., et al. 2013, Astrophys. J., 763, 145
- Dopita, M. A., Kewley, L. J., Heisler, C. A., & Sutherland, R. S. 2000, Astrophys. J., 542, 224
- Dors, O. L., Pérez-Montero, E., Hägele, G. F., Cardaci, M. V., & Krabbe, A. C. 2016, Mon. Not. R. Astron. Soc., 456, 4407
- Duc, P. A. & Mirabel, I. F. 1998, Astron. Astrph., 333, 813
- Ellison, S. L., Patton, D. R., Mendel, J. T., & Scudder, J. M. 2011, Mon. Not. R. Astron. Soc., 418, 2043
- Epinat, B., Amram, P., Balkowski, C., & Marcelin, M. 2010, Mon. Not. R. Astron. Soc., 401, 2113
- Fitzpatrick, E. L. 1999, Pub. Astron. Soc. Pacific, 111, 63
- Gallagher, S. C., Durrell, P. R., Elmegreen, D. M., et al. 2010, Astron. J., 139, 545
- Gomes, J. M. & Papaderos, P. 2017, Astron. Astrph., 603, A63
- Guseva, N. G., Izotov, Y. I., & Thuan, T. X. 2000, Astrophys. J., 531, 776
- Hägele, G. F., Pérez-Montero, E., Díaz, Á. I., Terlevich, E., & Terlevich, R. 2006, Mon. Not. R. Astron. Soc., 372, 293
- Hickson, P. 1982, Astrophys. J., 255, 382
- Hudson, C. E., Ramsbottom, C. A., & Scott, M. P. 2012, Astrophys. J., 750, 65
- Hunsberger, S. D., Charlton, J. C., & Zaritsky, D. 1996, Astrophys. J., 462, 50
- Hunter, D. A. & Hoffman, L. 1999, Astron. J., 117, 2789
- Iglesias-Paramo, J. & Vilchez, J. M. 1997, Astrophys. J., 479, 190
- Iglesias-Páramo, J. & Vílchez, J. M. 2001, Astrophys. J., 550, 204

Izotov, Y. I., Stasińska, G., Meynet, G., Guseva, N. G., & Thuan, T. X. 2006, Astron. Astrph., 448, 955

- James, B. L., Kumari, N., Emerick, A., et al. 2020, Mon. Not. R. Astron. Soc., 495, 2564
- Johnson, K. E. & Conti, P. S. 2000, Astron. J., 119, 2146
- Johnson, K. E., Vacca, W. D., Leitherer, C., Conti, P. S., & Lipscy, S. J. 1999, Astron. J., 117, 1708
- Kauffmann, G., Heckman, T. M., Tremonti, C., et al. 2003, Mon. Not. R. Astron. Soc., 346, 1055
- Kaviraj, S. 2014, Mon. Not. R. Astron. Soc., 440, 2944
- Kaviraj, S., Cohen, S., Windhorst, R. A., et al. 2013, Mon. Not. R. Astron. Soc., 429, L40
- Kehrig, C., Pérez-Montero, E., Vílchez, J. M., et al. 2013, Mon. Not. R. Astron. Soc., 432, 2731
- Kennicutt, Robert C., J. 1998a, Annual Review of Astronomy & Astrophysics, 36, 189
- Kennicutt, Robert C., J. 1998b, Astrophys. J., 498, 541
- Kennicutt, R. C. & Evans, N. J. 2012, Annual Review of Astronomy & Astrophysics, 50, 531
- Kewley, L. J., Dopita, M. A., Sutherland, R. S., Heisler, C. A., & Trevena, J. 2001, Astrophys. J., 556, 121
- Kewley, L. J., Rupke, D., Zahid, H. J., Geller, M. J., & Barton, E. J. 2010, Astrophys. J. Let., 721, L48
- Kniazev, A. Y., Grebel, E. K., Hao, L., et al. 2003, Astrophys. J. Let., 593, L73
- Kniazev, A. Y., Pustilnik, S. A., Grebel, E. K., Lee, H., & Pramskij, A. G. 2004, Astrophys. J. Suppl., 153, 429

Krabbe, A. C., Rosa, D. A., Dors, O. L., et al. 2014, Mon. Not. R. Astron. Soc., 437, 1155

- Kunth, D. & Schild, H. 1986, Astron. Astrph., 169, 71
- Lee, H., Grebel, E. K., & Hodge, P. W. 2003, Astron. Astrph., 401, 141
- Lee, H., Skillman, E. D., Cannon, J. M., et al. 2006, Astrophys. J., 647, 970
- Leitherer, C. 1990, Astrophys. J. Suppl., 73, 1
- Leitherer, C. & Heckman, T. M. 1995, Astrophys. J. Suppl., 96, 9
- Leitherer, C., Schaerer, D., Goldader, J. D., et al. 1999, Astrophys. J. Suppl., 123, 3
- Lenz, D. D. & Ayres, T. R. 1992, Pub. Astron. Soc. Pacific, 104, 1104
- López-Sánchez, Á. R. & Esteban, C. 2010, Astron. Astrph., 516, A104
- López-Sánchez, Á. R., Esteban, C., & Rodríguez, M. 2004, Astrophys. J. Suppl., 153, 243
- Magrini, L., Gonçalves, D. R., & Vajgel, B. 2017, Mon. Not. R. Astron. Soc., 464, 739
- Maiolino, R. & Mannucci, F. 2019, , 27, 3
- Marino, R. A., Rosales-Ortega, F. F., Sánchez, S. F., et al. 2013, Astron. Astrph., 559, A114
- Melnick, J., Tenorio-Tagle, G., & Terlevich, R. 1999, Mon. Not. R. Astron. Soc., 302, 677
- Mendes de Oliveira, C. L., Temporin, S., Cypriano, E. S., et al. 2006, Astron. J., 132, 570
- Moiseev, A. V., Tikhonov, A. V., & Klypin, A. 2015, Mon. Not. R. Astron. Soc., 449, 3568
- Muñoz-Elgueta, N., Torres-Flores, S., Amram, P., et al. 2018, Mon. Not. R. Astron. Soc., 480, 3257

Mu oz-Tu ón, C., Tenorio-Tagle, G., Castaneda, H. O., & Terlevich, R. 1996, Astron. J., 112, 1636

- Nagao, T., Maiolino, R., & Marconi, A. 2006, Astron. Astrph., 459, 85
- Oey, M. S. & Kennicutt, R. C., J. 1993, Astrophys. J., 411, 137
- Olave-Rojas, D., Torres-Flores, S., Carrasco, E. R., et al. 2015, Mon. Not. R. Astron. Soc., 453, 2808
- Olive, K. A. & Skillman, E. D. 2004, Astrophys. J., 617, 29
- Osterbrock, D. E. 1989, Astrophysics of gaseous nebulae and active galactic nuclei
- Pagel, B. E. J., Edmunds, M. G., Blackwell, D. E., Chun, M. S., & Smith, G. 1979, Mon. Not. R. Astron. Soc., 189, 95
- Pagel, B. E. J., Simonson, E. A., Terlevich, R. J., & Edmunds, M. G. 1992, Mon. Not. R. Astron. Soc., 255, 325
- Patton, D. R., Ellison, S. L., Simard, L., McConnachie, A. W., & Mendel, J. T. 2011, Mon. Not. R. Astron. Soc., 412, 591
- Pérez-Montero, E. 2014, Mon. Not. R. Astron. Soc., 441, 2663
- Pérez-Montero, E. 2017, Pub. Astron. Soc. Pacific, 129, 043001
- Pérez-Montero, E. & Contini, T. 2009, Mon. Not. R. Astron. Soc., 398, 949
- Pérez-Montero, E. & Díaz, A. I. 2003, Mon. Not. R. Astron. Soc., 346, 105
- Pérez-Montero, E. & Díaz, A. I. 2005, Mon. Not. R. Astron. Soc., 361, 1063
- Pérez-Montero, E., Hägele, G. F., Contini, T., & Díaz, A. I. 2007, Mon. Not. R. Astron. Soc., 381, 125
- Pérez-Montero, E., Kehrig, C., Brinchmann, J., et al. 2013, Advances in Astronomy, 2013, 837392
- Pettini, M. & Pagel, B. E. J. 2004, Mon. Not. R. Astron. Soc., 348, L59
- Pilyugin, L. S., Grebel, E. K., & Zinchenko, I. A. 2015, Mon. Not. R. Astron. Soc., 450, 3254

Plana, H., Amram, P., Mendes de Oliveira, C., Balkowski, C., & Boulesteix, J. 2003, Astron. J., 125, 1736

- Rich, J. A., Kewley, L. J., & Dopita, M. A. 2015, Astrophys. J. Suppl., 221, 28
- Rich, J. A., Torrey, P., Kewley, L. J., Dopita, M. A., & Rupke, D. S. N. 2012, Astrophys. J., 753, 5
- Richer, M. G., Georgiev, L., Rosado, M., et al. 2003, Astron. Astrph., 397, 99
- Riess, A. G., Macri, L. M., Hoffmann, S. L., et al. 2016, Astrophys. J., 826, 56
- Roth, M. M., Becker, T., Böhm, P., & Kelz, A. 2002, in Scientific Drivers for ESO Future VLT/VLTI Instrumentation, ed. J. Bergeron & G. Monnet, 136
- Roy, J.-R., Belley, J., Dutil, Y., & Martin, P. 1996, Astrophys. J., 460, 284
- Rubin, V. C., Hunter, D. A., & Ford, W. Kent, J. 1990, Astrophys. J., 365, 86
- Rupke, D. S. N., Kewley, L. J., & Chien, L. H. 2010a, Astrophys. J., 723, 1255
- Rupke, D. S. N., Kewley, L. J., & Chien, L. H. 2010b, Astrophys. J., 723, 1255
- Sánchez, S. F., Kennicutt, R. C., Gil de Paz, A., et al. 2012, Astron. Astrph., 538, A8
- Sánchez, S. F., Rosales-Ortega, F. F., Iglesias-Páramo, J., et al. 2014, Astron. Astrph., 563, A49
- Sánchez-Almeida, J., Morales-Luis, A. B., Muñoz-Tuñón, C., et al. 2014, Astrophys. J., 783, 45
- Schaerer, D. & Vacca, W. D. 1998, Astrophys. J., 497, 618
- Schmidt, M. 1959, Astrophys. J., 129, 243
- Seaton, M. J. 1979, Mon. Not. R. Astron. Soc., 187, 73
- Stasińska, G. 1978, Astron. Astroph. Supplement (Journal), 32, 429
- Stasińska, G. 1990, Astron. Astroph. Supplement (Journal), 83, 501
- Stasińska, G. 2006, Astron. Astrph., 454, L127

Storchi-Bergmann, T., Calzetti, D., & Kinney, A. L. 1994, Astrophys. J., 429, 572

- Surace, J. A. 1998, PhD thesis, Institute for Astronomy University of Hawaii 2680 Woodlawn Dr. Honolulu, HI 96822
- Tayal, S. S. & Zatsarinny, O. 2010, Astrophys. J. Suppl., 188, 32
- Toomre, A. & Toomre, J. 1972, Astrophys. J., 178, 623
- Torres-Flores, S., Mendes de Oliveira, C., Amram, P., et al. 2015, Astrophys. J. Let., 798, L24
- Torres-Flores, S., Mendes de Oliveira, C., Amram, P., et al. 2010, Astron. Astrph., 521, A59
- Torres-Flores, S., Scarano, S., Mendes de Oliveira, C., et al. 2014, Mon. Not. R. Astron. Soc., 438, 1894
- Torrey, P., Cox, T. J., Kewley, L., & Hernquist, L. 2012, Astrophys. J., 746, 108
- Tremonti, C. A., Heckman, T. M., Kauffmann, G., et al. 2004, Astrophys. J., 613, 898
- Vacca, W. D. & Conti, P. S. 1992, Astrophys. J., 401, 543
- van Zee, L., Salzer, J. J., Haynes, M. P., O'Donoghue, A. A., & Balonek, T. J. 1998, Astron. J., 116, 2805
- Verdes-Montenegro, L., Del Olmo, A., Yun, M. S., & Perea, J. 2005, Astron. Astrph., 430, 443
- Walborn, N. R. & Parker, J. W. 1992, Astrophys. J. Let., 399, L87
- Weilbacher, P. M., Duc, P. A., & Fritze-v. Alvensleben, U. 2003, Astron. Astrph., 397, 545
- Williams, B. A., McMahon, P. M., & van Gorkom, J. H. 1991, Astron. J., 101, 1957
- Willmer, C. N. A. 2018, Astrophys. J. Suppl., 236, 47
- Wong, O. I., Ryan-Weber, E. V., Garcia-Appadoo, D. A., et al. 2006, Mon. Not. R. Astron. Soc., 371, 1855

Xu, C. K., Domingue, D., Cheng, Y.-W., et al. 2010, Astrophys. J., 713, 330

Yates, R. M., Schady, P., Chen, T. W., Schweyer, T., & Wiseman, P. 2020, Astron. Astrph., 634, A107

Zaragoza-Cardiel, J., Smith, B. J., Rosado, M., et al. 2018, Astrophys. J. Suppl., 234, 35